Thesis for the degree
Doctor of Philosophy

חבור לשם קבלת התואר
דוקטור לפילוסופיה

By:
Efrat Shefer

מאת:
אפרת שפר

Supervisor:
Prof. A. Breskin

מנחה:
פרופ. ע. ברסקין

חקר חומרי פוטוקתודה חדשים ויציבים לשימוש בגלאי פוטונים גזיים בתחום האולטרא-סגול הקרוב עד הנראה

Study of novel stable photocathode materials for gaseous photon detectors in the near-UV to visible spectral range

September 2000

אלול תש"ס

Submitted to the Feinberg graduate school
Weizmann Institute of Science
Rehovot, Israel

מוגש למדרשת פיינברג
מכון וייצמן למדע
רחובות, ישראל

This Ph.D. research was performed under the supervision of Prof. A. Breskin at the Particle Physics Department of the Weizmann Institute of Science, Rehovot, Israel.

Acknowledgments

I would like to express my deep gratitude to all those who advised, supported and helped me to carry out this work.

In particular I thank my advisor, Prof. Amos Breskin, who created a research environment in the physics detector laboratory that encouraged a search for new ideas and methods. His vast knowledge, advise and encouragement were essential for the successful completion of this work.

Special thanks to Dr. Rachel Chechik who was always willing to discuss and comment. Her advise contributed greatly to this work.

I would also like the extend special thanks:

- To Dr. Alexei Buzulutskov who contributed significantly to various parts of this work and who helped me, especially in my first steps.
- To Dr K.B. Singh for his patient work on photocathodes aging and his help in constructing the experimental setups.
- To Moshe Klin and Yehuda Asher for their helpful technical support.
- To Dr. Hagai Cohen for his help and support in the XPS experiments.
- To Dr. Michael Rappaport and to Dr. Mark Prager for their help in constructing the experimental setup.
- To Amir Pansky, Thierry Boutboul, Guy Garty and Dirk Mureman, my fellow students, who made the laboratory a pleasant environment.

Last but not least I thank my husband Gil for his support encouragement and patience during the Ph.D. work period.

Table of contents

1. Introduction **8**

1.1 Presentation of the subject……..……. 8

1.2 Scientific background……..…… 9

1.2.1 Photon detectors for the far-UV to visible…..…… 9

1.2.2 Physics of photoemission from solid photocathodes……...…..… 13

1.2.3 Photocathodes for UV to visible spectral range…..…..…… 15

2. Study of near-UV to visible photocathodes **18**

2.1 Experimental techniques……..……..…… 18

2.1.1 Experimental setups and procedures……..…… 18

2.1.2 Alkali-antimonide preparation……...…… 21

2.1.3 Coating film preparation…… 22

2.1.4 UV-visible and x-ray photoelectron energy spectroscopy……..… 23

2.2 Electron transport model and simulation……..…… 29

2.2.1 The model……..…… 29

2.2.2 he Monte-Carlo calculations……..…… 32

2.3 Results……..…… 35

2.3.1 Bare alkali-antimonide photocathodes……...…… 35

2.3.2 Coated photocathodes…… 37

2.3.2.1 Chemical composition……..…… 37

2.3.2.2 QE spectra……..…… 42

2.3.2.3 QE attenuation length…….……..…… 44

2.3.2.4 Photoelectron energy spectroscopy……..…… 52

2.3.2.5 Stability in gaseous environment……...…… 61

2.3.2.6 Surface charging……...…… 68

2.3.2.7 Photon aging……..…… 69

2.3.2.8 Gas multiplication…… 70

2.3.3 Photocathodes with removable coating……..…… 71

3. Photocathodes in the UV range. **73**

3.1 Diamonds films……..…… 73

3.1.1 Experimental setup …… 73

3.1.2 QE spectra…… …… 73

3.1.3 Surface termination of CVD diamond films…….. 75

3.2 CsBr photocathodes…….. 75

3.2.1Experimental setup……... 75

3.2.2Chemical composition…….. 75

3.2.3QE spectra…… 76

3.2.4Photoelectron energy spectroscopy…….. 77

3.2.5Stability in gaseous environment……. 78

3.2.6Aging by photons and ions……... 78

4. Gas avalanche electron multipliers **81**

4.1 Micro-pattern multipliers……..…… 81

4.2 The Gas Electron Multiplier (GEM).…… 82

5. Discussion **86**

5.1 Visible photocathodes in gaseous detectors……..…… 86

5.2Electron transport properties……...…… 88
5.3 UV photocathodes……...……...…… 90
5.4 Application and future investigations…… 91
6. Summary **94**
Literature……...…… 96

List of figures

1.1 A scheme of a gaseous photon detector…… 5
1.2 Band bending at the vacuum interface…….. 8
1.3 Absolute QE spectra of numerous commercial UV-to visible photocathodes….. 9
2.1 The experimental setup for the evaporation and characterization of protective layers on alkali-antimonide photocathodes……... 11
2.2 A photograph of the photocathode mounted within the oven element……. 12
2.3 The new experimental setup for the production and characterization of protective coatings on alkali-antimonide photocathodes, and for detector sealing…….……... 13
2.4 A picture of the sample transfer chamber……. 16
2.5 The setup for the measurement of photoelectron energy distribution……... 17
2.6 Photoelectron energy distribution dependence on the bias voltage…….. 19
2.7 Photoelectron energy distribution from CsI photocathodes…….. 19
Ion sputtering effect on the photoelectron energy distribution…….. 20
2.9 XPS wide scan of K-Cs-Sb photocathode coated with 50Å CsBr film…… 20
2.10 A scheme of the photocathode-coating film interface…….. 22
2.11 The QE attenuation length as a function of the photon energy, calculated for different values of the free parameter E_{loss}……...……. 26
2.12 The difference between simulated and measured QE attenuation length, Δ, as a function of the free parameter E_{loss}..... 27
2.13 Distribution of the absolute quantum efficiency values of reflective photocathodes prepared in our setup……. 28
2.14 Absolute QE spectra of a commercial and atypical K-Cs-Sb photocathode prepared at our setup…… 29
2.15 Exposure of K-Cs-Sb photocathode to methane……..…….. 29
2.16 Depth profiles of the elemental atomic concentrations of K-Cs-Sb photocathodes coated with CsBr films……..…… 32
2.17 XPS K line shift due to oxidation……... 33
2.18 Depth profiles of the elemental atomic concentrations of K-Cs-Sb photocathodes coated with CsI films……. 34
2.19 Absolute QE spectra of K-Cs-Sb photocathodes: bare coated with CsI films of different thickness……..…… 35
2.20 Absolute QE spectra of bare K-Cs-Sb and Cs_3Sb photocathodes and coated with CsBr, NaI and CsI films…… 36
2.21 Relative QE of K-Cs-Sb Cs_3Sb photocathodes coated with CsBr, NaI, CsI, CsF and NaF films as a function of the film thickness……. 37
2.22 Relative QE of Cs_3Sb photocathodes coated with HTC, CaSt and SiO films as a function of the film thickness…… 38
2.23 Relative QE of CsBr-coated K-Cs-Sb and Cs_3Sb photocathodes measured at different photon wavelength as a function of the film thickness…….. 39
2.24 Measured QE Attenuation length in CsBr, CsI, NaI, CsF and NaF films deposited on K-Cs-Sb and Cs_3Sb photocathodes as a function of the incident photon energy. …….. 40

2.25 Measured QE attenuation length in CaSt, HTC and SiO deposited on Cs_3Sb photocathodes as a function of the incident photon energy…….. 41
2.26 Calculated QE attenuation length dependence on the electron affinity value….. 42
2.27 Attenuation length in CsBr-coated K-Cs-Sb photocathodes: measured and calculated using different initial distributions. ……. 43
2.28 Measured and calculated QE attenuation length in CsBr, CsI and NaI films deposited on K-Cs-Sb and Cs_3Sb photocathodes as a function of the incident photon energy. …….. 44
2.29 Normalized photoelectron energy distribution from K-Cs-Sb photocathode coated with CsBr and CsI films, at different thickness, induced by 2.85-4.9eV photons. …… 46
2.30 Calculated photoelectron energy distribution on the electron affinity value…… 49
2.31 Monte-Carlo calculations and measurements of normalized photoelectron energy distribution from K-Cs-Sb photocathode coated with CsBr and CsI films. ……. 50
2.32 Calculated and experimental peak position and FWHM values of photoelectron energy distribution from CsBr-coated K-Cs-Sb photocathode film versus photon energy. …….. 51
2.33 Calculated and experimental peak position and FWHM value of photoelectron energy distribution from 250Å thick CsI-coated K-Cs-Sb photocathodes versus photon energy..…….. 52
2.34 Calculated and experimental peak position and FWHM value of photoelectron energy distribution from 500Å thick CsI-coated K-Cs-Sb photocathodes versus photon energy. …….. 53
2.35 Exposure to O_2 of K-Cs-Sb and Cs_3Sb photocathodes: bare and coated with CsI, NaI and CsBr films. …….. 55
2.36 QE spectra of CsI-coated K-Cs-Sb photocathodes, exposed to 150 Torr of oxygen for different periods…….. 56
2.37 Exposure to O_2 of K-Cs-Sb and Cs_3Sb photocathodes: bare and coated with CsF, NaF, HTC, CaSt and SiO films……. 57
2.38 Exposure to O_2 of K-Cs-Sb photocathodes: bare and coated with CsI films of different thickness..……... 58
2.39 Exposure to water vapor of K-Cs-Sb photocathodes coated with CsI and CsBr films..……. 59
2.40 Exposure to ambient air of K-Cs-Sb photocathodes coated with CsBr films….. 60
2.41 Charging up of a CsBr-coated K-Cs-Sb photocathode……. 61
2.42 Aging by photons of a CsBr-coated K-Cs-Sb photocathode…… 62
2.43 Gas multiplication versus electrode voltage for a parallel plate multiplier coupled to a CsBr-coated K-Cs-Sb……... 63
2.44 Evolution of the QE of a Cs-Sb photocathode coated with removable HTC film 65
3.1 Absolute QE spectra of a CVD diamond: as grown and treated by H_2 plasma and of a DLC film. ..…… 67
3.2 Absolute QE spectra of DLC films with different concentration of sp^3 bonds, of a CVD diamond and a graphite sample……. 67
3.3 Absolute QE spectra of semitransparent and reflective CsBr photocathodes as deposited and after heat treatment……. 69

3.4 Photoelectron energy distribution from fresh and air-exposed reflective CsBr photocathode, induced by 4.9eV photons……..……... 70
3.5 The effect of x-ray on the photoelectron energy distribution from a CsBr photocathode, induced by 4.9eV photons……. 71
3.6 Aging by photons of CsBr photocathodes…… 72
3.7 Aging by avalanche ions of CsBr photocathodes……. 73
4.1 A scheme of the micro-dot avalanche chamber and the electrode layout…….. 75
4.2 Single photoelectrons current pulses recorded from the anodes of a micro-dot electrode…… 76
4.3 The Gas Electron Multiplier…… 76
4.4 Multiplication curve of the GEM at 40-400Torr…… 77
4.5 The 3-GEM photon detector…….. 78
4.6 The gain of the 3-GEM photon detector…… 78
5.1 A scheme of a 2D digital mammography-imaging detector…….. 85
5.2 A photograph of a 2 dimensional gas avalanche photomultiplier digital mammography-imaging detector…….……. 85

Notations

E_G – band gap energy
E_A - electron affinity
ϕ - work function
AES – Auger electron spectroscopy.
APD – avalanche photodiode
CBM – conduction band minimum
CCD – charge coupled device
CVD – chemical vapor deposition
DLC – diamond like carbon
FWHM – full width half maximum
GEM – gas electron multiplier
HPD – hybrid photodiode
MCP – micro channel plate
MRS - metal-resistor-semiconductor
MTC – Monte-Carlo
MWPC – multi wire proportional chamber
NEA – negative electron affinity
PES – photoelectron spectroscopy
PMT – photomultiplier tube
QE – quantum efficiency
RICH – ring imaging Cherenkov
SEM – scanning electron microscope
VBM – valence band maximum
VLPC – visible light photon counter
UV – ultra-violet
XPS – x-ray photoelectron spectroscopy

1. Introduction

1.1 Presentation of the subject

This work involves the search for novel photocathode materials sensitive over the UV-to-visible spectral range and compatible with an operation within advanced gas avalanche imaging photomutipliers. Such photon detectors, based on the conversion of photons in a thin solid photocathode, followed by the emission and multiplication of the photoelectrons in gas, have numerous advantages compared to other state of the art techniques [1]. They are parallax-free, fast and have very good time and localization resolutions. Unlike vacuum-based devices they have small sensitivity to magnetic fields and can be made very large. Detectors having sensitive area of the order of a square meter, equipped with CsI photocathodes, sensitive in the UV spectral range, are successfully employed in Cherenkov detectors in numerous particle- and nuclear physics experiments [2-4].

A search for materials with high photoemission yield, viable under gaseous electron multiplication is of prime importance for further development of efficient and stable gas avalanche photomultipliers. There is a strong motivation for achieving sensitivity of theses new photon imaging devices in the near-UV to visible range where numerous applications exist. It is a very difficult task, because unlike the far-UV spectral range, where photocathode materials are chemically stable, typically employed photocathodes in the visible spectral range are alkali-antimonides, which are highly reactive. Even minute levels of oxygen, water and CO_2, commonly present in counting gases, result in total loss of the photocathodes sensitivity [5].

In this work we primarily investigated the possibility of modifying the surface of alkali-antimonide photocathodes by coating them with thin dielectric protective films. The protective coating film allows for the transport of photoelectrons through it to the gas, while preventing contact between the gas impurities and the photocathode. Its thickness, typically a few hundred Å, is a compromise between the need for high photo-yield and for chemical stability. Coating Cs-Sb photocathodes by CsI films was proposed by Peskov et al. [6,7]; their attempts resulted, at best, in very low quantum efficiency (number of emitted electrons per incident photon) of 0.15% at wavelength 350nm.

The study of photoemission from coated photocathodes requires the investigation of low-energy photoelectron transport in the photocathode and in the coating layers, as well as in the interface between the two materials. It is of a more general interest, providing the important information regarding the electronic states of the coating material.

We therefore defined the following prime goals for this work:

1. Development of thin-film-protected solid photocathodes, sensitive in the near-UV to visible spectral range and viable under gaseous electron multiplication.
2. Characterization of the coated photocathodes, including absolute quantum efficiency spectra, photoelectron energy distributions and chemical composition.
3. Acquiring of a better understanding of low-energy (<4eV) electron transport through thin dielectric protective films and through the photocathode coating film interface.
4. Coupling of a photocathode to a gaseous electron multiplication element to form a visible-photon gas avalanche detector and investigating its performance.

In order to achieve these goals, methods were found for the preparation and coating of alkali-antimonide photocathodes in the laboratory. We studied in detail the photoemission properties of coated photocathodes by measuring quantum efficiency spectra for different

coating films and photoelectron energy distributions were investigated in detail using photoelectron spectroscopy. We developed a model of low-energy electron transport through the photocathode coating film interface and the coating film. Monte Carlo calculations, based on the model, were performed providing the photoelectron energy distributions and the quantum efficiency attenuation due to the coating film. There is good agreement between the calculated and measured results.

The stability of the novel composite photocathodes has been systematically investigated, under exposure to counting gases and impurities and under gas multiplication conditions. The effect of high photon flux on the photocathodes was also studied.

In addition to the prime goals and scope of this work the following related subjects were studied:

1. In the UV spectral range we investigated diamond films produced by chemical vapor deposition (CVD). These films are radiation-hard and chemically inert. Some attention was given to “solar-blind” CsBr photocathodes.
2. We have investigated the properties of some novel gas avalanche multipliers, and operation conditions which suit their application within gas avalanche photomultipliers.

This research work has paved the way towards imaging of visible light with gas avalanche detectors, which have numerous advantages. The novel coated photocathodes have other applications besides the field of photon detectors; they are already being investigated as possible stable laser-triggered electron sources in accelerators [8]. From the results of our photoemission and electron transport studies we gained understanding of the low-energy electron transport mechanism in the coating film and new information regarding the photocathode coating film interface.

In the following we will provide a brief scientific background on photon detectors, theory of photoemission from solids and currently used photocathodes. Chapter 2 presents the study of coated alkali-antimonide photocathodes, including experimental methods, low-energy electron transport model and our experimental and calculated results. The main results of our studies in the UV spectral range are summarized in chapter 3 and the discussion concerning gaseous electron multipliers can be found in chapter 4.

1.2 Scientific background

1.2.1 Photon detectors for the far-UV to visible

Photon detectors are among the most complex devices used in physics experiments, because they must achieve high efficiency for photon conversion into a photoelectron and for the detection of single photoelectrons. Photon detection in solid state devices is different than that in vacuum and gaseous devices, since the photons are absorbed and detected in the same solid medium, usually without any charge multiplication. In vacuum and gaseous devices the photons are converted into photoelectrons that are multiplied in vacuum or in gas before detection, allowing for their operation in photon counting mode. The photon absorption usually takes place in a solid film, from which the photoelectrons are emitted into the multiplication element.

solid state devices.

Solid state detectors utilizing microelectronic technology are based on the conversion of photons into electron-hole pairs in a semiconductor material. In the UV-to-visible spectral range, a photon would typically create 1-2 electron–hole pairs. These devices, which usually

do not have any internal gain, are sensitive only to high photon levels. There are a few exceptions of devices with internal gain used to detect single photons, as discussed below. Their advantages include high QE, fast response and immunity to magnetic fields. Their flaws are the limited size, typically a few mm^2, high internal noise, low resistance to radiation and their cost. They are also an order of magnitude slower than photomultiplier tubes (see the following section), with typical minimal time scale of 1ns.

The charge-coupled devices (CCD) are widely used for imaging purposes. They are made of an array of potential wells, which operate as pixels, each 10-15μm in square. The charges, created when the CCD is illuminated, are collected in the potential wells. For the readout, the voltage applied to potential wells is adjusted, and the charge moves from one well to its adjacent, until it is collected by the electronics. The CCD is a 2D-imaging device, with an excellent spatial resolution. However, it is available in small sizes, less than $1cm^2$. Due to the serial readout, it is a slow device with a minimum resolving time of 10msec for one image. Its dynamic range is limited by the capacitance of the potential wells. It is mass-produced and therefore relatively inexpensive.

Avalanche photodiodes (APD) consist of a fully depleted p-n junction. A photon creates an electron-hole pair in the depletion zone and the electron and hole drift oppositely in the electric field. If the electric field is high enough, these carriers can acquire enough kinetic energy to create e-h pairs in turn, starting an avalanche process. Their internal gain is typically a few hundreds [9], and may reach 10^4 [10]. The standard APD is a few mm in diameter but APD with active area of up to $13cm^2$ were reported [10]. Spatial resolution is achieved by constructing APD arrays. The QE is typically 60-80% over the broad spectral range of 400-900nm.

The more recent metal-resistor-semiconductor (MRS) device [11-13] is a non-planar APD in which the p-n junction is arranged in “needles” thereby creating high electric fields, allowing for high internal gain of 10^5. The resistive layer provides a feedback controlling the avalanche. This layer is locally charging up at the area of the multiplication, giving rise to an electric field that decelerates and terminates the avalanche. The device has a relatively low QE reaching 30% and 1-2% at red and green light, respectively [11], although there are reports of higher QE: 60% at 350nm [12]. Single photons may be detected due to the high gain and small needle pitch size (5μm). Single photon may also be detected at low efficiency (few %), at -30^0C in another MRS structure [14]: the limited Geiger mode microcell. These detectors are not commercially available.

The visible light photon counter (VLPC) [15-17] is based on impurity band-gap structures designed to convert single photons into a few 10^4 electrons with QE of the order of 80%. It offers excellent single photon counting capability at high rates of the order of 100MHz for 1mm diameter pixel [18]. However, the device is operated at cryogenic temperature of 6-10K, as the impurity band gap is 50meV, and is limited to a few mm in diameter.

Numerous works, investigating the use of materials other than Si are in progress. Among them are chemical vapor deposition (CVD) diamond films [19-21], amorphous Si [22], GaN [23,24] and even polymers [25]. They are not sensitive to single photons.

Vacuum devices

The most common devices used for visible light detection are vacuum photomultipliers tubes (PMT). Photoelectrons emitted from a photocathode into vacuum, hit a dynode structure for fast multiplication of signals. Their great advantages are their fast response, low noise,

high gain and commercial availability. Due to their dynode-based multiplication, they are sensitive to magnetic fields and standard PMTs cannot be operated in high magnetic environment. In the last decade new types of PMTs became available. Among them are multi-anode position sensitive PMT and PMT capable of operation under high magnetic fields [26]. The latter consists of 15 to 19 stages of fine mesh dynodes set close to each other. This proximity configuration yields a relatively high electric field and results in possible operation in an axial magnetic field as strong as 1.5T [26]. The largest available PMT is 20" in diameter but has no position sensitivity, while the position sensitive and the fine mesh photomultipliers are limited to 3" diameter. The efficiency of the PMT is determined by the photocathode's QE, and it may reach 30-40% at maximum, using bialklai-antimonide photocathodes.

A relatively new device is the hybrid photodiode (HPD) [27]. It is made out of a photocathode mounted in front of a planar semiconductor diode. The photocathode and the diode are separated by a vacuum gap and are held at a potential difference of a few kilovolts. An incoming photon is converted at the photocathode into a photoelectron, then accelerated towards the silicon diode by an electrostatic de-magnifying field or by proximity focussing electron optics. Due to the acceleration a single photoelectron acquires enough energy to produce a significant signal is the Si diode. Position sensitive response is realized by patterning the diode electrodes.

The HPDs display very good single photon counting capability [28] and their performance is not impaired by axial magnetic fields as high as 1.5T [29,30]. At CERN large HPDs with a diameter of 2" are being developed [31], but their active area coverage is only 70%. Commercially available HPDs, consisting of avalanche photodiodes, having gains of $6\text{-}8\times10^4$ allow for operation at high counting rates using fast, low gain electronics [32]. However their size is less than 1cm in diameter. The QE of the HPD is the same as that of PMT, as the same photocathodes are used. The readout electronics of some position-sensitive devices is located within the vacuum envelope, limiting the number of useable channels. Another problem is the distortion of the image due to the electrostatic de-magnifying field.

A review of the latest trends in vacuum-based photon detectors and a comparison between them and solid-state devices can be found in [33].

Gaseous photon detectors

Compared to the vacuum and solid state photon detectors, discussed in the previous sections, gaseous detectors have an advantage when large detection area and good spatial localization are needed, down to the level of single photons. No other technique is cost competitive for square meters of coverage. They can operate under the presence of high magnetic fields [4], which is of considerable importance in most particle physics and some medical imaging applications.

Gaseous photon detectors are based on the multiplication in a gas of primary charges deposited by incoming photons. Photons can be converted into electrons either in a photosensitive gas where charges are also multiplied or in a solid photocathode coupled to the gas electron multiplier. The state of the art in gas photomultipliers is reviewed in [34]. The most popular photosensitive vapors are TMAE (tetrakis (dimethylamine) ethylene) and TEA (triethylamine), both widely employed in photon detectors for RICH detector systems [35]. TMAE, with photoemission threshold at ~5.4eV, has the highest known quantum efficiency (QE), defined as the number of electrons emitted per incident photon [36]. However, it is a fragile and chemically reactive molecule resulting in fast aging of the detector. Detectors

based on gaseous photoconverters suffer from parallax errors due to different absorption depths of the photons under angular incidence. The resolving time of the detector is affected by the drift-time of released charges across the detector depth (hundreds of ns).

A more recent class of photon detectors combines solid radiation converters with gaseous electron multipliers [37]. Figure 1.1 shows a scheme of such a photon detector. Due to a surface electron emission, followed by an immediate charge multiplication, such detectors have practically no parallax error or time jitter. The converter thickness and material are chosen according to the photon energy. The most efficient solid photoconverter for the far UV is CsI with a photoemission threshold at ~6eV [2]. More recent photocathodes in the fare UV, CsBr and CVD diamonds will be discussed below. The principles and state of the art of these gas avalanche phtomultipliers are reviewed in ref. [1].

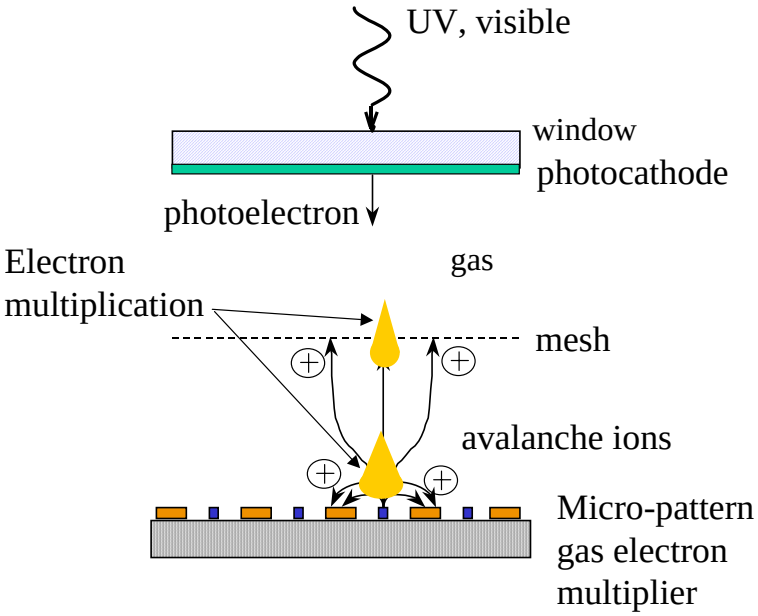

Fig. 1.1: *A scheme of a photon detector incorporating a photocathode, a mesh and a micro-patterned electron multiplication element. Single photoelectrons are amplified at the mesh and further multiplied at the anode strips, which provide localization. Most avalanche-induced ions are collected by the cathode strips and by the mesh.*

Solid photocathodes for the near-UV to visible range will be discussed in detail in section 1.2.3. The most commonly materials used are mono-alkali and bi-alkali photocathodes. However, due to the high chemical reactivity of these materials, they must be kept in a high vacuum environment. Exposure of such a photocathode to gases of standard and even high purity ($\leq$ 1ppm of O_2) will result in a fast decrease in the photocathode QE. Therefore, despite some early works in this field [38,39], no gaseous photodetectors for the near-UV to visible range exists.

Solid photocathodes combined with gaseous electron multipliers have a few other problems [34]. Positive ion feedback onto the photocathode may cause sputtering that limits its lifetime [37,38]. This could be reduced to a certain extent, using special amplification geometry [1,40,41] or, for very small counting rates, electronic gating [38]. Most of the photosensitive materials are good insulators; the back-drifting ions can be deposited on the

photocathode resulting in an increase in the electric field across the photosensitive insulating layer and causing a spontaneous emission of electrons from that layer (Malter effect [42]). On the other hand, surface charging of the photocathode, can result in a modification of the electric field at the surface and hence a reduction in the electron extraction efficiency and in the gas gain. Another problem of photosensitive materials is the undesirable emission of photoelectrons due to photons released in the gas multiplication process (photon feedback effect). This can limit the detector's gain and distort the image.

The photoelectron extraction efficiency strongly depends on the counting gas and on the electric field at the photocathode vicinity due to the electron back-scattering process. High electric fields enhance inelastic processes (excitation, ionization) on the account of elastic scattering, thus allowing for maximal electron extraction efficiencies close to that in vacuum [43].

The gaseous electron multiplier, coupled to a photocathode should have a large gain and good electron extraction from the photocathode, allowing for the efficient detection of single photoelectrons. Its mode of operation should minimize the fraction of avalanche-induced ions back-drifting to the photocathode as well as the photon feedback. The multiplier should allow for an operation at high counting rates, often required in applications in particle physics and medical imaging. The micro-pattern electron multipliers [44], developed over the last decade and the more recently proposed Gas Electron Multiplier (GEM) [45] are attractive for photocathode-based photon detectors. They will be discussed in chapter 4.

1.2.2 Physics of photoemission from solid photocathodes.

A three-step process according to the Three-Step Model developed by Spicer [46,47] describes photoemission. The first step is the absorption of a photon leading to the production of a high-energy electron in the solid; the second is the motion of this electron to the vacuum or gas interface; and the third is the escape of the electron over the surface barrier into the vacuum. The first two steps are bulk phenomena and the third is a surface phenomenon.

Absorption of photons. The absorption of photons is affected by the light reflectivity of the material and by the absorption coefficient. Metals have high reflectivity in the visible and near UV region, resulting in a decrease in the QE of metallic photoemitters by one to several orders of magnitude. In non-metallic materials (insulators and semiconductors) the reflectivity is usually low, and the absorption coefficient for photon energies greater than the gap energy E_G, is very high, in the 10^5 to 10^6 cm^{-1} region. Low gap energy is desirable for high absorption coefficient for visible light, but it should not be too low to allow for thermionic excitation of the electrons that would result in thermal noise. High gap materials are suitable in the UV spectral range.

Motion of the electron to the vacuum interface. The photoelectron created by the photon is a "hot" electron, with an energy above that of the thermal equilibrium. The probability that this hot electron will reach the vacuum interface depends on the energy loss processes along its path. The two main energy loss mechanisms are electron-electron and electron-phonon scattering.

In metals, due to the large amount of free electrons, the main energy loss mechanism is electron-electron scattering in which a large fraction of the photoelectron energy is lost at each collision. As a result, the photoelectron reaches thermal equilibrium within a short distance and can typically escape from the metal into vacuum only if it was excited a few atomic layers from the surface.

In non-metals (insulators and semiconductors) the photoelectrons, are excited from the valence band to the conduction band. The minimal energy required for this excitation is the band gap energy, E_G, that is defined as the energy difference between the conduction band minimum and the valence band maximum. The dominant energy loss mechanism for electrons with energy smaller than E_G is the electron-phonon scattering. In this process the energy loss per collision is much smaller than in the electron-electron scattering. Furthermore, these energy losses can be partially compensated by energy gains of the same order. This results in a greater volume from which electrons can escape into vacuum. Experimental results show that for example in alkali halides, particularly in CsI, photoelectrons created at a distance of several hundred angstroms from the surface can have sufficient energy for emission [48]. If the absorption coefficient is large, $\sim 10^6 cm^{-1}$, the efficiency of the two first steps for a reflective photocathode can approach 50% due to geometrical considerations.

Surface potential barrier. The potential barrier at the surface of metals is their work function ϕ, defined as the energy difference between the vacuum and the Fermi level of the metal. It is at least ~2eV and for most metals above ~3eV. An electron can escape into the vacuum only if its energy is greater than the work function, resulting in a photoemission threshold of about ~400nm. For non-metals, the photoelectron reaching the vacuum interface has to overcome the electron affinity E_A, defined as the difference between the vacuum level and the minimum of the conduction band energy. The minimum photon energy required in order to produce photoemission is E_G+E_A, which has to be less than ~3eV for sensitivity to visible light and in the 4-10eV range for sensitivity to the UV.

The necessary requirements for high QE in non-metals are a high optical absorption coefficient and photon energy greater than E_G+E_A. A photoemission threshold at longer wavelengths requires low value of E_G+E_A. Other factors that affect the QE of non-metals are:

1. *E_G to E_A* ratio. Non metals with $E_G>E_A$ tend to have higher QE than those with $E_G<E_A$. In the latter case, a photon with energy greater than E_G+E_A will excite an electron from the valence to the conduction bands. This electron will have sufficient energy to either escape into the vacuum or excite a second electron from the valence band to the conduction band. If two electrons are excited to the conduction band, there is a large probability that neither will have sufficient energy to escape into the vacuum. In many materials the second electron-hole pair production is more probable than the emission into vacuum. It should be noted that this "thumb rule" is qualitative, and it is the detailed band structure of the relevant material that determines the relative probability of pair production and electron emission.
2. *Band bending*. Impurities and defects are unavoidable, and were not considered so far. The presence of defect levels is particularly important in the case of doped materials such as p-type semiconductor with n-type surface states [49]. This combination results in a shift of the Fermi level, bending the energy bands downward. The band diagram of such a material is shown in fig. 1.2. An electron excited from the valence band at a distance greater than *a* from the surface is accelerated by the internal field with the result that it has to overcome only the "effective" electron affinity E_{Aeff}. It is also possible to describe this phenomenon as a creation of an electric dipole at the surface of the photo-emitter, resulting in an electric field that accelerate the electrons into the vacuum.
3. *Multi-electron effect*. If the energy of a photon is greater than $2(E_G+E_A)$, the possibility exists, and increases with increasing photon energy, that the resulting photoelectron produces one or more secondary electrons. Thus the QE can exceed unity.

Since for most materials E_G+E_A is greater than ~2eV, secondary electrons can be expected in the far UV and higher energies only.
A more detailed discussion of the processes affecting the QE can be found in [50].

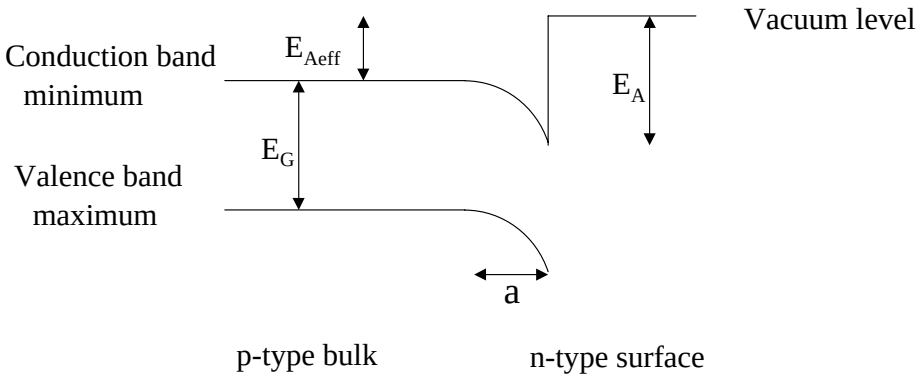

Fig. 1.2: *Effect of band bending on the threshold of photoemission: the electron affinity, E_A, is replaced by an effective electron affinity E_{Aeff} for electrons excited at a depth greater than a from the surface.*

1.2.3 Photocathodes for the UV to visible spectral range.

Most of the efficient solid photocathodes sensitive in the near-UV to visible range, below 3.5eV, belong to one of the following groups:

- Mono-alkali antimonides: Cs_3Sb, K_3Sb, Rb_3Sb, Na_3Sb, Li_3Sb
- Multi-alkali antimonides: Na-K-Sb, Cs-Na-K-Sb, K-Cs-Sb etc.
- Silver based photocathodes: Ag-O-Cs, Bi-Ag-O-Cs.
- Negative electron affinity (NEA): GaAs(Cs), GaAsP(Cs), Si(Cs).

Of the first group, Cs_3Sb with E_G of ~1.6eV [46] and E_A of ~0.45eV [46,51] is the most widely used and has the highest QE. A typical curve of the QE of a semitransparent photocathode is shown in fig. 1.3 [33]. The decrease in the QE at the higher photon energies is due to the light absorption in the photocathode substrates. The fabrication procedure of Cs_3Sb is described in section 2.1.2. An interesting phenomenon observed for Cs_3Sb is its reaction to exposure to oxygen. Exposure to very small traces of oxygen reduces the surface barrier, which results in an increase in QE in all wavelengths, and a higher photoemission threshold wavelength [52]. At this stage the oxygen reacts only with the surface of the photocathode. When exposed to higher oxygen levels, the bulk of the photocathode chemically reacts with it, reducing its QE, and leading to its total destruction.

The exact stoichiometry of the Cs-Sb photocathodes was investigated thoroughly [53-55]. Although Cs_3Sb is the most likely stoichiometric formula and was measured by several authors, none of the methods including microbalance [53], flame photometry [54] or crystallography [55] has the accuracy to detect small deviations from the 3:1 ratio. Dorn et. al. [56] found 7 possible compounds of Cs-Sb: Cs_3Sb, Cs_5Sb_2, Cs_2Sb, Cs_5Sb_4, CsSb, $CsSb_2$ and Cs_3Sb_7.

All other materials in the first group have similar characteristics and fabrication procedure; a full discussion of these materials and of Cs_3Sb can be found in [57].

The photocathodes in the multi-alkali antimonide group have in general higher QE than those in the first group, by a factor of about 2. However, their fabrication is more complicated

and there are great variances in QE and in the photoemission threshold from sample to sample. K-Cs-Sb photocathodes, used as the principal photocathode in this work, were initially reported by Sommer in 1963 [58]. Their main advantages are higher QE in the blue region, stability at higher temperatures and low thermionic noise. The fabrication procedure of K-Cs-Sb, applied in our work, is described in section 2.1.2. The uncertainty in the stoichimetry of the K-Cs-Sb photocathode is even larger than in the case of Cs-Sb, because the complicated preparation procedure. McCarroll [59] used crystallography to measure a ratio of K_2CsSb.

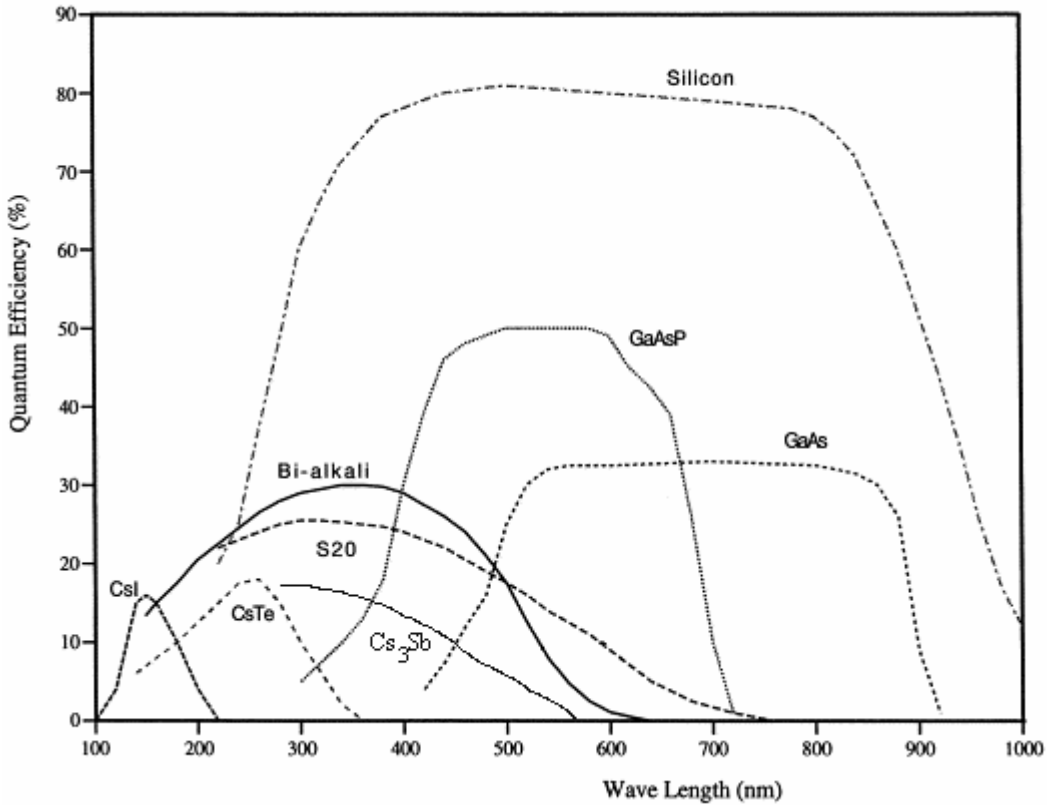

Fig. 1.3: *Absolute QE spectra of numerous commercial UV-to visible photocathodes. S20 and bi-alkali photocathodes are Na_2KSb and K-Cs-Sb respectively. GaAs and GaAsP are solid state photocathodes. The efficiency of silicon devices is shown for comparison. The decrease in the QE at short wavelength is due to window light transmission. The figure was taken (slightly modified) from ref [33].*

The silver-based photocathodes are most useful in the near infrared region. Even though the Ag-O-Cs photocathode was discovered before the antimony based materials, its exact chemical composition and microscopic structure are not well known. The fabrication process is also only partially understood, and is mostly empirical. More details regarding these photocathodes can be found in Sommer's book [57].

The NEA photocathodes [50,60], such as GaAs(Cs) and GaAsP(Cs), are based on materials in which the vacuum level lies below the conduction band minimum in the bulk. This is achieved by p-doping of a semiconductor, usually by adding a mono-layer of Cs. A few mono-layers of Cs and O_2 on the surface give rise, in addition to the p-doping, to an electrical dipole accelerating the electrons into the vacuum. The combination of these two processes produces an enhanced band bending (see section 1.2.2). The great advantage of

such materials is that even thermalized electrons reaching the surface can escape into the vacuum. Therefore, photoelectrons created at a distance of several μm from the surface have sufficient energy for emission, resulting in a very high QE, up to 50%, in the 400-700nm range. On the other hand, the long diffusion distance of the electrons to the photocathode surface, results in a relative slow response time of a few ns, compared to less than a ps in other non-metals. Other disadvantages of these materials are the difficult fabrication process, limiting the size of the photocathodes and increasing their cost and their instability when not sealed under vacuum.

The materials described so far, with high QE in the visible spectral range have, as a rule, uniform high sensitivity to photons of higher energy, i.e., to UV radiation. Other photocathodes sensitive in the UV spectral range, which do not respond to the radiation emitted by the sun, are the “solar blind” photocathodes. The “solar blind” photocathodes can be defined as insensitive to photon with energy below 3.5eV for use in the earth atmosphere or below ~6eV for use in space.

High QE in the 3.5-6eV range was obtained with only two materials: Cs_2Te and Rb_2Te [61]. Cs_2Te with photoemission threshold at 3.5eV has more than 10% QE above 4.5eV. Its preparation process is similar to that of Cs_3Sb: a Te film at elevated temperature is activated by Cs vapor. An excess of Cs results in a reduction of the photoemission threshold down to 1.5eV and an increase in the QE to ~30%. Rb_2Te was not investigated as thoroughly as Cs_2Te. It has similar properties, with a photoemission threshold in the 3.5-4ev range.

Alkali-halides, with the exception of the most fluorides, reach QE values of the order of a few tens of percents. The most efficient are CsI and CsBr with photoemission threshold at 6.1eV and 7.3eV and QE values of 40% and 30% at 150nm, respectively [2,62,63]. Their preparation is very simple, as they can be thermally vacuum-evaporated. Most alkali-halides are stable in standard-purity gas environment. An investigation of the stability of alkali-halides on exposure to air showed that CsI is more stable than the other materials [64]. As discussed previously, CsI is used as a photocathode in gaseous and vacuum photomultipliers.

2. Study of near-UV to visible photocathodes

2.1 Experimental techniques

2.1.1 Experimental setups and procedures.

Two experimental setups were used for the study of alkali-antimonide, Cs_3Sb and K-Cs-Sb, photocathodes in our laboratory. The first, described in detail in ref. [65], is shown in fig. 2.1. It consists of a high-vacuum chamber, in which alkali- and bialkali-antimonide photocathodes are prepared, and their absolute quantum efficiency is measured in situ. In the same setup one can also evaporate thin protective films on the photocathode surface, and measure the stability of the bare or coated photocathodes under exposure to gas.

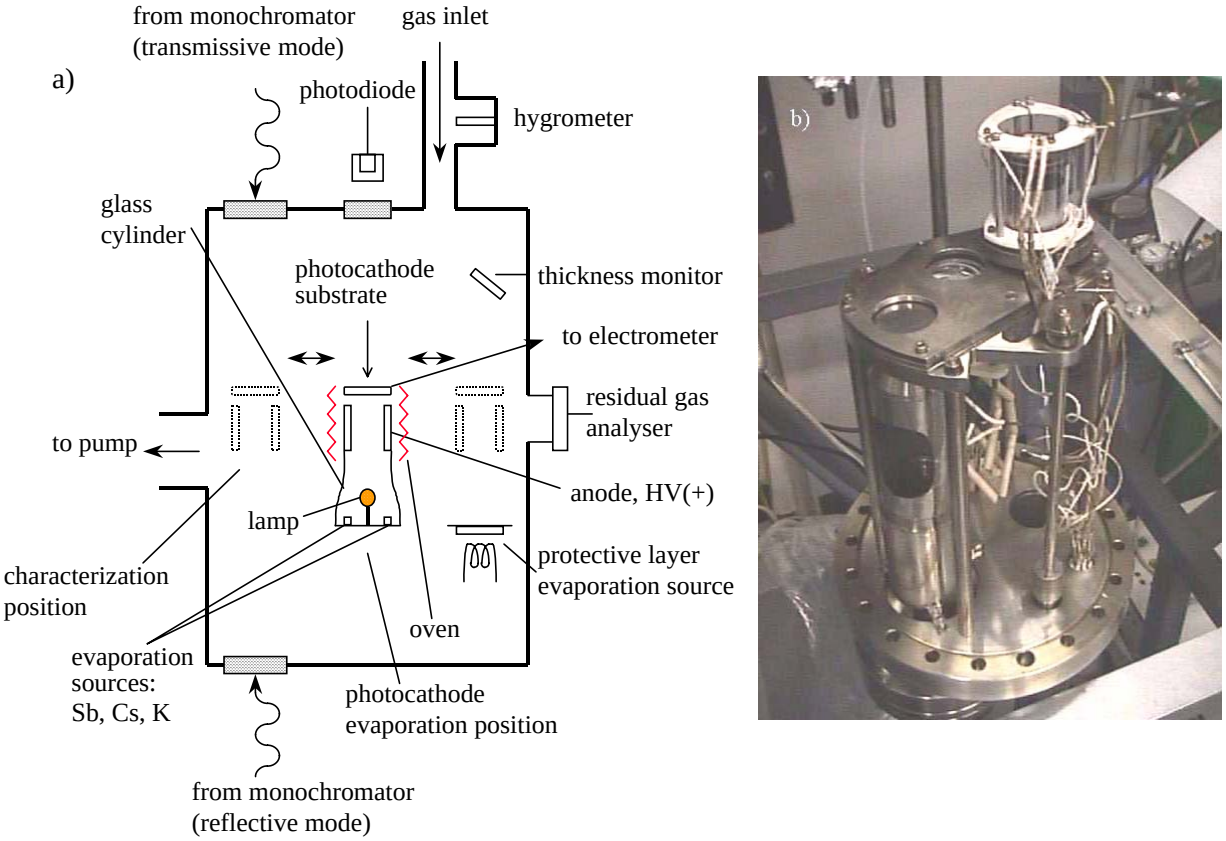

Fig. 2.1: *A scheme (a) and a photograph (b) of the experimental setup for the evaporation and characterization of alkali-antimonide photocathodes and of their protective layers.*

The chamber is bakable and its vacuum can reach values of $5*10^{-9}$Torr, by means of a turbo molecular pump. The photocathode substrate can be displaced between three positions within the vacuum chamber: for photocathode evaporation, for the measurement of quantum efficiency and for thin protective film evaporation. Details of the photocathode production element are shown in figure 2.2. The photocathode substrate is mounted above a stainless steel cylindrical anode, surrounded by a glass cylinder. The latter provides some protection of the photocathode surface form impurities originating from the vacuum chamber volume. The entire complex is located within an activation oven, made of tungsten wire spirals, the temperature of which can vary up to 270^0C. The photocathode evaporation site comprises three evaporation positions, one for antimony and two for alkali metals, and a collimated halogen lamp. The latter is employed for measurement of light transmission through the

photocathode by means of a photodiode, in order to control the antimony thickness, and for monitoring the photocurrent during the photocathode activation.

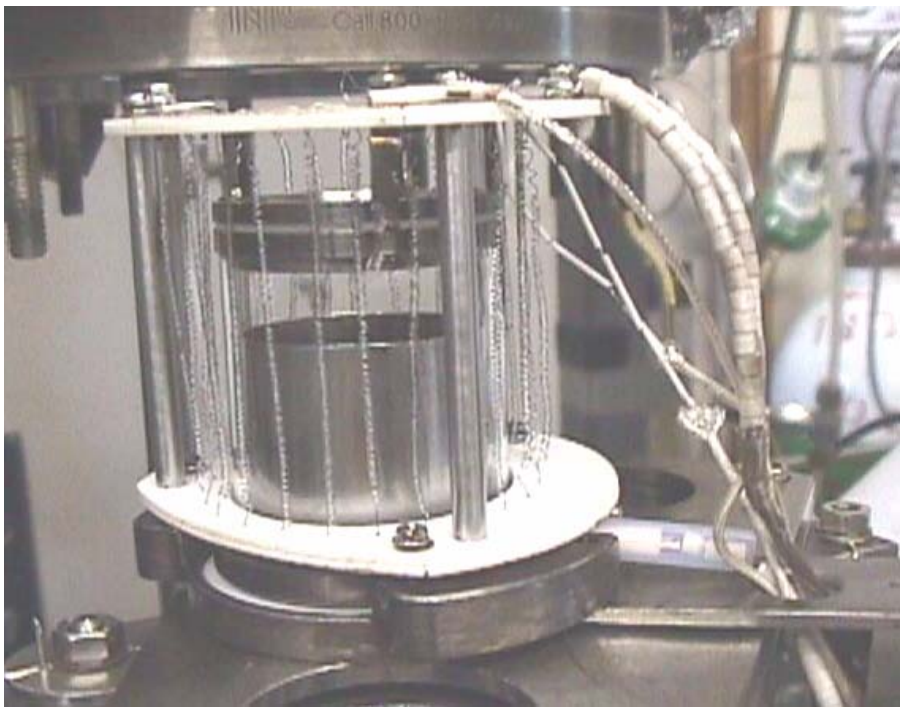

Fig. 2.2: *A photograph of the photocathode mounted within the oven element. The photocathode quartz substrate is held between two metal rings on top of a glass cylinder. The cylindrical anode is situated inside the glass cylinder below the photocathode. An activation oven made of a tungsten wire coil surrounds the glass cylinder and the photocathode. The height of the complex is approximately 5cm.*

Absolute quantum efficiency spectra can be obtained in a transmissive or reflective mode, at the spectral range of 250-550nm. The photocathode is illuminated by an Hg(Ar) lamp, coupled to a monochromator. A positive voltage is applied to the cylindrical anode placed a few mm away from the photocathode and the photocurrent is measured on the photocathode. The light flux is calibrated with a photodiode (Hamamatsu S1723-02) whose quantum efficiency is known with an accuracy of ±10%. The protective film deposition (section 2.1.3) is made by resistive evaporation. A quartz crystal thickness monitor controls the protective film thickness. A small, inner cylinder encloses the evaporation volume of the protective films, preventing the contamination of the evaporation chamber. Various gases can be introduced into the chamber by a manifold made of clean materials. The setup is also equipped with a hygrometer (Panametrics PanDry hygrometer) and a residual gas analyzer (SRS RGA200) allowing for the chemical analysis of the vacuum quality and of the gases inserted into the chamber.

This setup was the first to allow for a systematic investigation of the QE and chemical stability of bare and coated alkali-antimonide photocathodes, **in-situ**. The setup has two drawbacks: it does not allow for coupling of the photocathodes to a gaseous electron multiplier and at maximum, one photocathode per week can be produced and tested in it. Therefore, a second, more complex setup, shown in fig. 2.3, was designed and constructed. This setup consists of three vacuum chambers, evacuated by turbo-molecular pumps and baked prior operation. The first is an introduction chamber where the substrates are baked

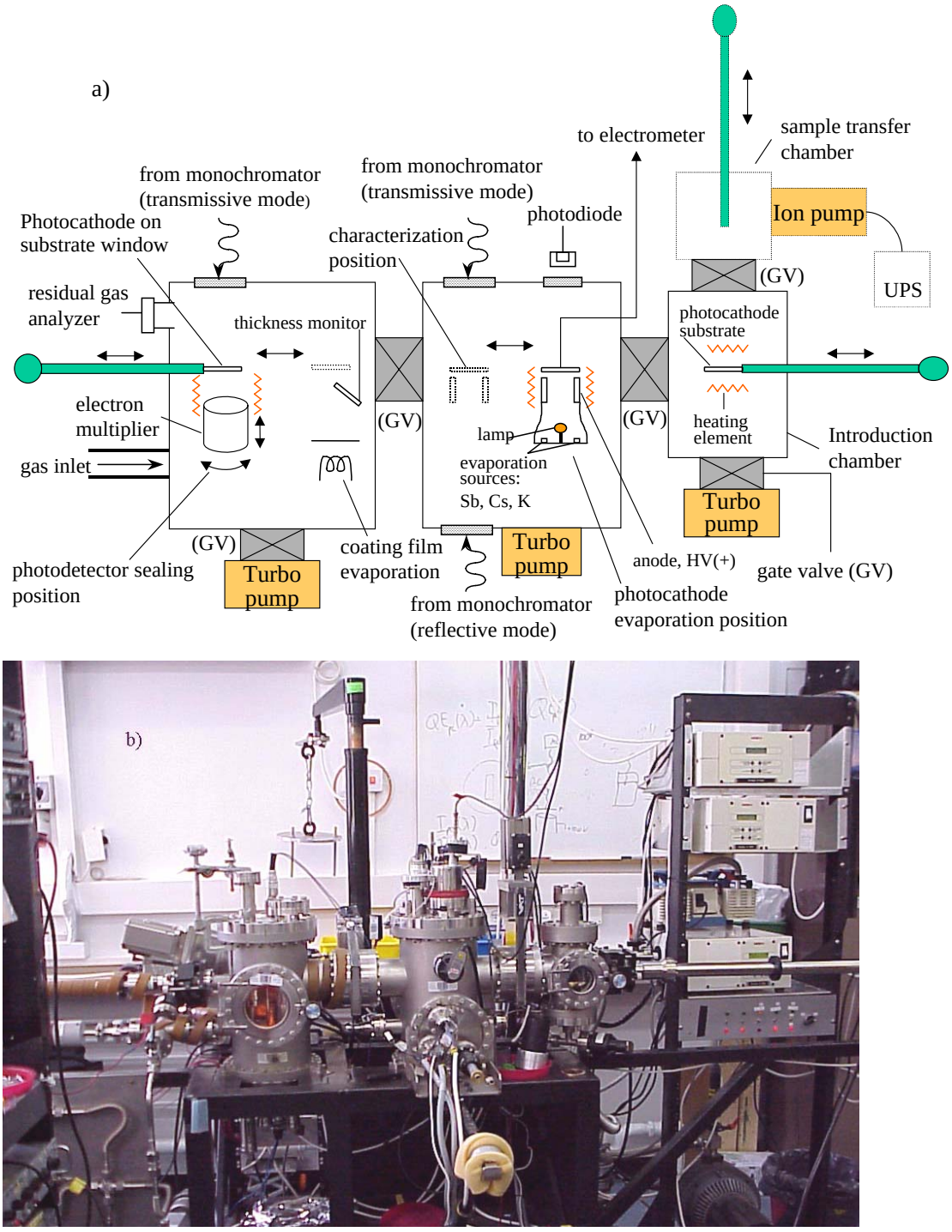

Fig. 2.3: *A scheme (a) and a photograph (b) of the new experimental setup for the production and characterization of protective coatings on alkali-antimonide photocathodes, and for detector indium sealing. The setup consists of three vacuum chambers: an introduction chamber for substrate baking, a central chamber for alkali-antimonide photocathodes production and characterization and a third chamber for evaporation of protective coatings, characterization and detector sealing. A sample transfer chamber can be attached to the introduction chamber.*

under high-vacuum (10^{-8}Torr). In the central, ultra-high vacuum chamber ($5*10^{-10}$Torr), the alkali-antimonide photocathodes are prepared and the QE spectrum is measured in situ. The photocathode production element is larger than in the first setup and the activation oven consists of four 500W halogen lamps, surrounded by a stainless steel reflector. The chamber contains evaporation materials for the preparation of up to 9 photocathodes.

In the third chamber, the photocathodes can be coated with protective films and exposed to a gaseous environment by the same method as in the first setup. One can also couple a photocathode to a gas electron multiplier and form a photon detector by indium sealing the photocathode coupled to an electron multiplier in a package

The experimental procedure of the measurement of the QE dependence on the coating film thickness included the preparation of an alkali-antimonide photocathode (see section 2.1.2), measurement of the QE spectrum in a reflective mode, evaporation of a coating film (see section 2.1.3) and re-measurement of the QE spectrum. The last two steps were repeated several times.

Exposure of the photocathode to gas was performed by filling the chamber with gas at a known pressure for five minutes, followed by pumping of the chamber and measuring the QE spectrum in vacuum. This was repeated several times for increasing pressures, measuring the QE evolution in the gas. All the steps were carried out in-situ.

2.1.2 Alkali-antimonide preparation

Photocathode production depends on many parameters, some of them are not clearly defined, resulting in large fluctuations in their quality. We defined a detailed production procedure resulting in reasonable variations in the photoemissive properties. As a rule, we found that the deposition at initial vacuum below 10^{-7}Torr resulted in stable photocathodes with reasonably high quantum efficiency values.

The evaporation sources used were alkali metal dispensers (SAES Getters Cs/NF/5.5/17FT10+10, K/NF/3.1/17FT10+10) and 99.999% pure elemental antimony (Alfa, antimony shots) previously melted, under vacuum of 10^{-6}Torr, in a Ta boat. During the vacuum chamber-baking period, small currents (a few Amperes) are applied to the alkali metal dispensers and antimony boat in order to outgas possible contaminnts.

Cs_3Sb and K-Cs-Sb photocathodes were produced on 4mm thick, 36mm or 63.5mm in diameter optically polished suprasil quartz substrates. The substrates are cleaned with NaOH and distilled water, followed by 10 minutes rinse in absolute acetone and 10 minutes in absolute ethyl alcohol in an ultra sonic bath; they are dried using clean nitrogen. Electrical contacts are provided by evaporation of a 1000Å thick aluminum film on the circumference of the substrate.

The first part in the production procedure of both photocathode types, Cs_3Sb and K-Cs-Sb, is the evaporation of antimony on a substrate held at room temperature or at 150^0C-160^0C. The antimony thickness is monitored by measuring the attenuation of white light transmission through the substrate during the evaporation. The evaporation usually lasts for 15-30 sec and is terminated after a light flux decrease to 70% of its initial value.

Cs_3Sb photocathodes are prepared by heating the antimony-deposited substrate to 160^0C-170^0C and evaporating cesium. The photocurrent of the photocathode is monitored throughout the activation process, and the Cs evaporation is stopped when it reaches a maximal value. We then cool the photocathode, measuring the photocurrent. A stable photocathode undergoes an increase in the photocurrent while being cooled to room temperature.

In the case of K-Cs-Sb photocathodes, the substrate is heated to 195^0-200^0C and potassium is evaporated. The evaporation is stopped when a K-Sb photocathode is formed, indicated by a maximum in the photocathode photocurrent. In order to remove some of the potassium and allow for cesium reaction, the substrate is then heated to 240^0C for 10sec, cooled down to 195^0-200^0C, and a decrease of the photocurrent to about one half of the maximal value is registered. To complete the photocathode activation, the substrate is cooled down to 175^0-180^0C and cesium and antimony are alternately evaporated until the photocurrent reaches a peak value. The photocurrent is also monitored during the photocathode cooling. In case of a decrease, a very small amount of antimony is evaporated in order to stabilize the photocathode.

2.1.3 Coating film evaporation

All the coating films investigated (CsI, CsBr, NaI. CsF, NaF, SiO, n-$C_{36}H_{74}$ and $(O_2C_{18}H_{35})_2Ca$) were produced by a vacuum resistive evaporation technique. The reasons for having chosen these materials will be given in section 2.3.2.The thickness of the film and its deposition rate were monitored with a quartz crystal oscillator (Sycon instruments STM100) with an accuracy of ±5%. The film thickness was calculated relative to the bulk density of the deposited material, hence, it was not corrected for the possible reduced packing density that in principle could take place [66,67]. The geometrical correction factor was carefully calibrated by weighting the quartz crystal prior to and after evaporation of a film and comparing the thickness derived from this measurement with the quartz crystal oscillator reading. This was repeated several times for different film thickness.

The materials were evaporated from Ta boats that were closed with a perforated cover. For SiO the cover was hand-made with one central hole. The evaporation material was typically a powder of high purity. Some of the materials were evaporated on a heated substrate by heating the oven surrounding the photocathode. The deposition rate was typically 0.1-0.5Å/sec. The heating of the substrate and the slow deposition rate were applied in order to achieve high QE of the coated photocathode [68]. The substrate was maintained at room temperature when evaporating n-$C_{36}H_{74}$, due to its low melting temperature. Other materials, for which no improvement in QE due to heating was observed either in previous [68] or in this work, were also evaporated on a substrate at room temperature. For NaI films, a post-evaporation heat-treatment for a few hours, was a key element for attaining the highest photoelectron transmission. In order to obtain organized $(O_2C_{18}H_{35})_2Ca$ films, which should have very good electron transport properties [69], with a vacuum-evaporation technique, we followed the procedure reported in [70]. This consisted of slow evaporation rate (0.1Å/sec) on a substrate held at an elevated temperature of 70^0C. Table 2.1 summarizes the coating film deposition parameters:

Deposited material	Purity (%) Alfa Aesar	Substrate temperature (^{0}C)

CsI	Ultra pure	24, 60
CsBr	99.9	24, 80
NaI	99.5	60, 80
CsF	99.9	24
NaF	99	75
SiO	99.9	70
n-$C_{36}H_{74}$	99	24
$(O_2C_{18}H_{35})_2Ca$	98	70

Table 2.1: The list of coating materials, their respective puritylevels and the deposition conditions of the coating films.

2.1.4 UV-visible and x-ray photoelectron energy spectroscopy

An important part of the research was carried out in the x-ray photoelectron spectroscopy (XPS) facility at the Weizmann Institute of Science. In order to transfer the samples without contaminating them, a high vacuum ($5*10^{-9}$Torr) transfer chamber equipped with a battery-operated ion pump was designed and constructed (see figure 2.4). The prepared samples were extracted via the introduction chamber and brought to the XPS analysis system in a vacuum better than 10^{-8}Torr. In the XPS facility, both x-ray and UV-visible photoelectron spectroscopy (PES) were performed.

Fig. 2.4: *A picture of the sample transfer chamber. Thc chamber consists of a manipulator, a gate valve and a battery-operated ion pump.*

A scheme of the UV-visible PES measurement setup is shown in figure 2.5. A Hg(Ar) lamp coupled to a monochromator illuminates the photocathode through a quartz window so

that the center of the light spot coincides with the center of the electron optics. A set of filters was used at the monochromator exit in order to reduce the stray light and to assure illumination by mono-energetic photons. The photoelectrons were accelerated by a bias voltage applied to the photocathode.

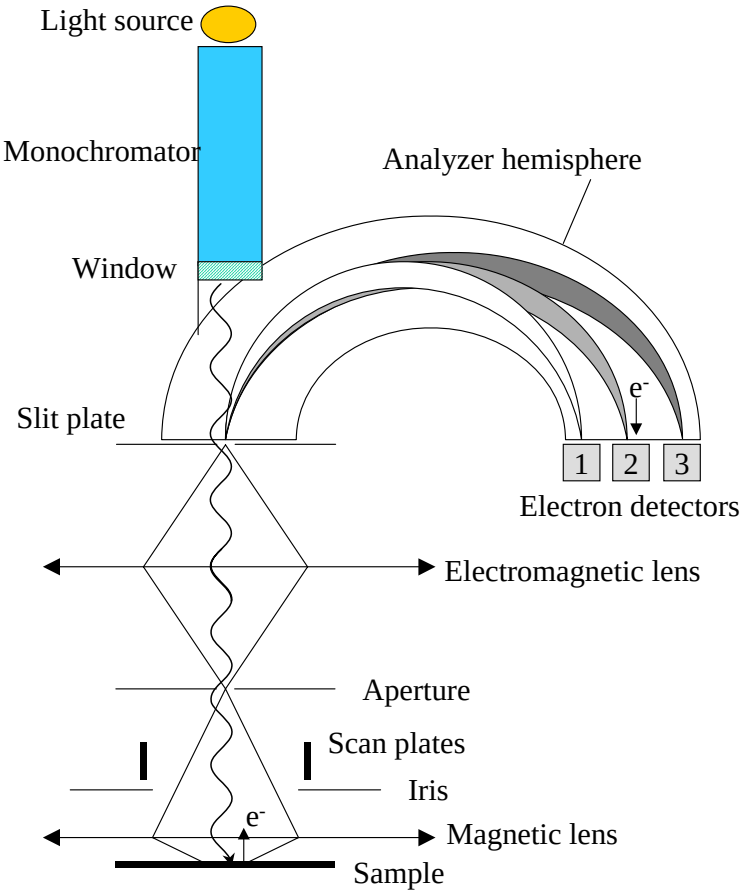

Fig. 2.5: *A scheme of the setup for the measurement of photoelectron energy distribution. Mono-energetic photons, emitted by a lamp coupled to a monochromator, pass through a quartz window, illuminating the sample, and exciting photoelectrons. The photoelectrons are emitted into the vacuum and are brought by means of electron optics (magnetic lens, iris and aperture) to the analyzer hemisphere. Three detectors at the far end of the hemisphere measure the intensity of the emitted electrons. The electron energy scan is performed by changing the potential applied to the scan plates.*

As we were the first users to measure UV-visible PES in that facility, the UV-visible PES measurement conditions were optimized and determined to be:

- Magnetic mode
- Detector 2 (central) only. (1 and 3 switched off)
- Pass energy 5eV
- Aperture 18.50
- Iris 12-14 turns
- Bias voltage: -15V - -20V
- Energy scan step size 0.025eV

In the magnetic mode, electrons are collected from a small area, with a relatively large solid angle. In an electrostatic mode, not applied here, they are collected from a larger area

and a smaller solid angle. For example: using a fully opened aperture (18.5), the collection area diameter is approximately 1mm in the magnetic mode, and 1cm for the electrostatic mode. Although no significant difference was observed in the shape of the photoelectron energy spectrum in the two modes, the signal intensity measured in electrostatic mode was smaller than in the magnetic mode. In general, a great difference in intensity between the spectra recorded on different detectors or using different energy pass or aperture values was observed in the electrostatic mode.

The best results in terms of signal intensity and spectrum width were obtained with detector 2. This is probably due to fewer artifacts by the analyzer hemisphere.

The pass energy determines the energy resolution of the detector: the lower is the pass energy value, the better is the resolution. For pass energies of 5eV and 10eV, the detector energy resolution is approximately 0.08eV and 0.16eV respectively. Naturally, the signal intensity is reduced for lower pass energy value. The observed improvement in the spectrum width between pass energy 10 and 5eV was not large, but it is important because the UV-visible spectra are very narrow.

The aperture, located at the image plane, controls the object size (the area from which electrons are collected). Collecting electrons from a small area may be important in the case of spatial non-homogeneity. The smaller the aperture, the smaller is the collection area. The fully opened aperture (18.50) corresponds to a collection area of approximately 1mm in diameter. It was preferred since no difference in the spectrum shape was observed, while the intensity decreases for smaller aperture.

The iris is located at the focal plane designed to determine the maximal angular region of collection. In our measurements, it also affected the size of the light spot. The dependence of the photoelectron energy spectra on the iris was monitored. The spectrum shape remained unchanged for 0-14 turns, but was distorted for smaller iris size. The iris size was chosen to give the smallest light spot, which did not yet distort the spectrum.

The dependence of the photoelectron energy spectrum shape on the bias voltage is summarized in figure 2.6. The bias was varied between –40V and –7V. For the voltage range between –20V and –40V, the measured spectrum was broader than for smaller bias voltages. The width remained constant in the –7V to –15V range. One can see a strong decrease in signal intensity as the bias voltage is lowered, and the beginning of a collection plateau for higher voltages.

We worked at the smallest available energy scan step size because the systematic error is determined by this step size and by the detector's energy resolution. For energy scan step size of 0.025eV and energy resolution of 0.08eV, the systematic error was 0.04eV.

Calibration standards are gold or silver samples, but due to the low photoelectron yield from metals, our attempts to measure PES of these samples resulted in very poor signal-to-noise ratio. However, our measurement of electron energy distribution from CsI, induced by 6.7eV photons, is in very good agreement with the results of DiStefano [71] as can be seen in figure 2.7.

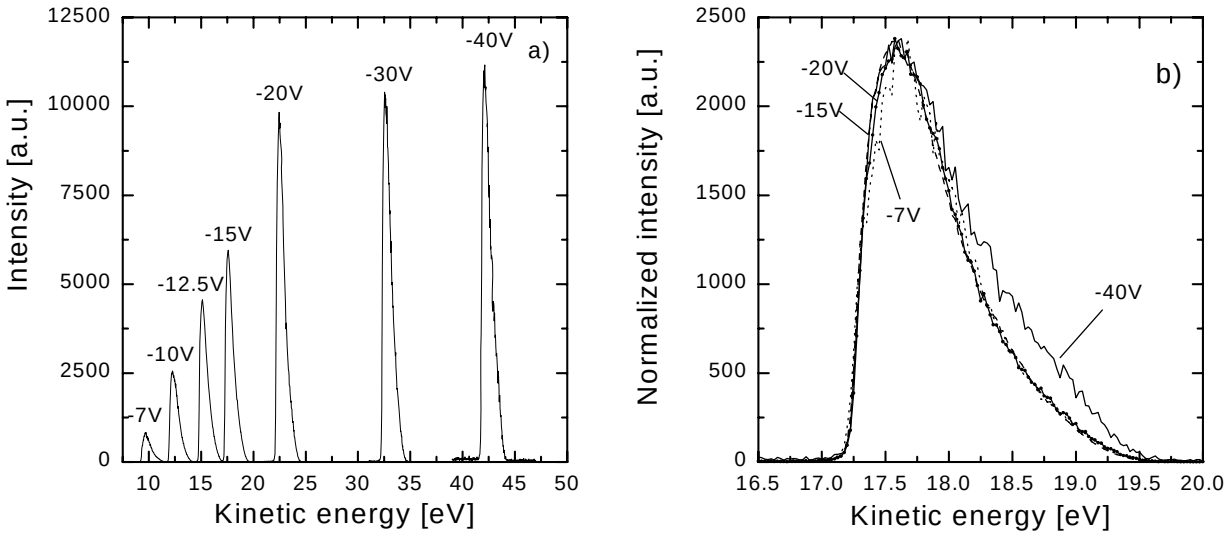

Fig. 2.6: *Photoelectron energy distribution from a K-Cs-Sb photocathode coated with a 50Å thick CsBr film, illuminated with 4.9eV photons and measured using different bias voltages in the magnetic mode. Shown are the spectra a) as measured and b) normalized.*

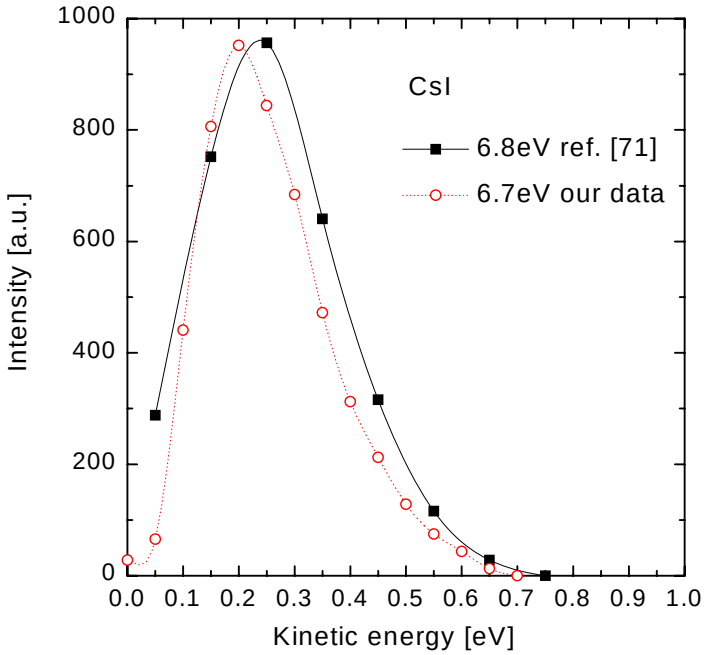

Fig. 2.7: *Photoelectron energy distributions from CsI photocathodes. Shown are our measured spectrum, induced by 6.7eV photons and the spectrum measured by DiStefano et al. [71], induced by 6.8eV photons.*

In order to remove surface contamination, fine ion sputtering was performed on a 500nm thick CsI sample. The photoelectron energy spectra before and after the sputtering are shown in figure 2.8. The sputtering reduced the signal intensity drastically, and caused a shift in the spectrum. The spectrum gradually shifted back to its original position but the intensity remained low. These changes are attributed to the structural damage induced by the ion beam.

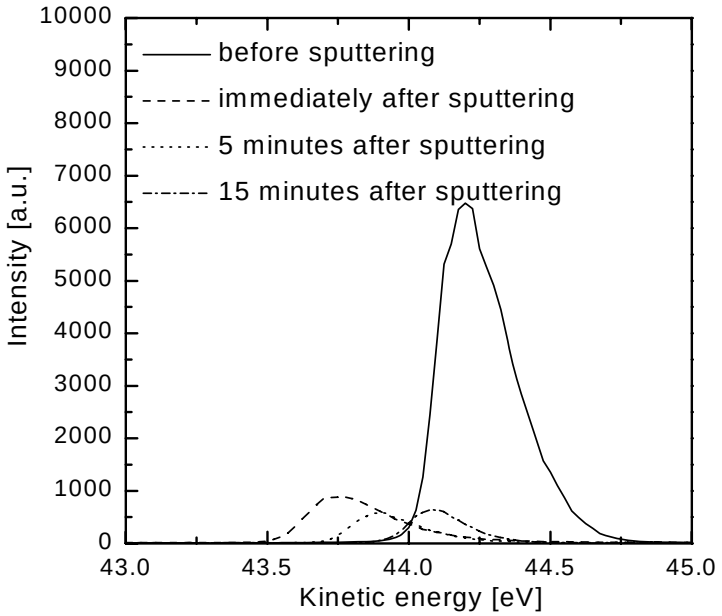

Fig. 2.8: *Photoelectron energy distributions from a 5000Å thick CsI film illuminated with 6.7eV photons, measured before and at different times after Ar^+ ion sputtering.*

XPS is a well-known experimental technique, therefore, only the main points relevant to our measurements will be briefly discussed here. The experimental system used for the XPS measurements is the same as shown in fig. 2.5, the only difference being that the sample is illuminated by an internal 1.5KeV x-ray source. Since the kinetic energy of the measured emitted electrons is larger than 300eV, no bias was applied on the sample. Fig. 2.9 shows a typical wide sweep performed on a 50Å thick CsBr-coated K-Cs-Sb photocathode. Electrons leaving the surface with negligible energy loss produce the peaks. The peaks can be correlated to the elements because each element has a unique set of binding energies. The atomic concentration on the surface is extracted from the area under the peaks and the known electron emission intensity at different energies of the elements. The typical error of this measurement is of the order of 5% of the atomic concentration value.

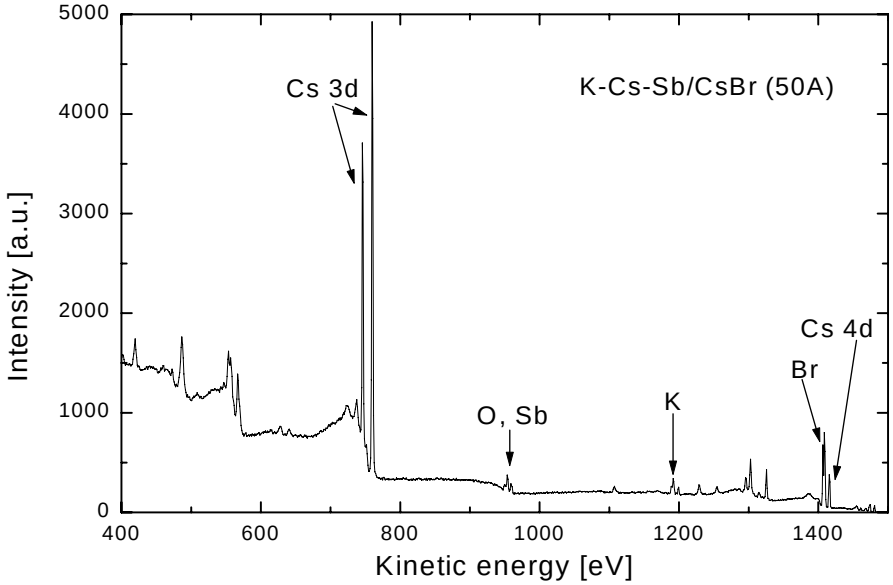

Fig. 2.9: *An XPS wide scan of a K-Cs-Sb photocathode coated with 50Å thick CsBr film.*

It is important to define the meaning of "surface" to which XPS measurements are sensitive. The probability, P, of an electron excited at a distance d from the surface to escape into the vacuum with almost no energy loss is determined by the mean-free-path for inelastic interactions λ and it follows the relation:

(2.1) $$P(d) \sim e^{-d/\lambda}$$

Since λ is typically 25Å, the definition of a surface in these measurements is a few tens of Å thick layer.

2.2 Electron transport: model and simulation.

2.2.1 The model.

The photoemission process from coated photocathodes can be described as a sequence of five steps:

1. Photon absorption.
2. Photoelectron transport within the photocathode.
3. Photoelectron transition through the interface between photocathode and coating film.
4. Photoelectron transport through the coating film.
5. Photoelectron escape into vacuum.

1, 2. Photon absorption and photoelectron transport within the photocathode.

In the present work the first two steps, of photo-absorption and electron transport in the photocathode, were not calculated. Instead we used measured energy distributions of electrons emitted from photocathodes to the vacuum and injected them, after some modification, into the photocathode-coating film interface, as will be explained below. We used our own measured distributions (K-Cs-Sb coated with 50Å CsBr and 50Å CsI) as well as that of others (bare Cs-Sb [51,72] and K-Cs-Sb [73]).

3. Photoelectron transition through the interface between photocathode and coating film.

Modeling the transport of electrons through the interface requires some assumptions concerning the interface nature, because the contact between the two materials modifies their structure near the contact surface, creating an interface with unknown chemical composition and geometrical dimensions. The photocathode surface quality and the coating film evaporation conditions naturally affect the interface. Fig. 2.10 shows the simplified scheme assumed for the interface, namely a step function with zero thickness.

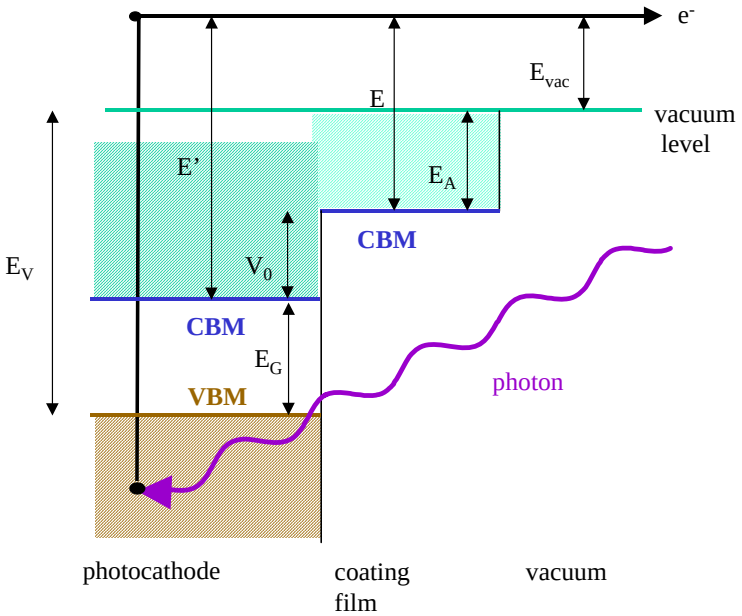

Fig. 2.10: *A scheme of the photocathode-coating film interface. The photon is absorbed in the photocathode resulting in an excitation of an electron from the valence to the conduction band. This electron overcomes the photocathode-coating film interface, transports through the coating film and over the electron affinity into vacuum.*

Normally, the energy scheme at the interface of two materials is determined by the equalization of their Fermi levels. In our case, there is no data on the exact location of the Fermi levels of either species and therefore we use a different approach. From the experimental QE spectra taken with a bare photocathode and coated ones, we can extract the shift in the cutoff (red boundary) wavelength. From this we may define the location of the vacuum level with respect to the valence band maximum (VBM) of the coated photocathode, namely E_V; and using the known energy gap of the photocathode, E_G, we can locate the photocathode conduction band minimum (CBM). We further use the known electron affinity of the coating film, E_A, to locate the CBM of the coating relative to the vacuum level and thus to the CBM of the photocathode. This defines the barrier V_0.

(2.2) $$V_0=E_V-E_G-E_A$$

Table 2.2 summarizes the values of E_G, E_A and E_V for the interfaces under investigation.

Photocathode			**Coating film**		**interface**
material	E_G (eV)	E_A^{PC} (eV)	material	E_A (eV)	E_V (eV)
K-Cs-Sb	1.0 [74]	1.1 [74]	CsI	0.2 [75]	2.65
			CsBr	0.4 [76]	2.25
			NaI	1.5 [57]	2.35
Cs_3Sb	1.6 [46]	0.45 [46,51]	CsI	0.2	2.40
			CsBr	0.4	2.45
			NaI	1.5	2.55

Table 2.2: The energy gap (E_G) and electron affinity (E_A^{PC}) values of the photocathodes considered in this work; the electron affinity of the coating film and the photoemission threshold of the coated photocathodes (E_V), extracted from QE measurements.

The initial energy of the photoelectron relative to the photocathode CBM, E', is modified when crossing the barrier V_0, into E relative to the coating film CBM in the coating film. The direction of the electrons after crossing the interface was assumed to be uniformly distributed within a cone of angle ϕ_c, derived from momentum conservation:

(2.3) $$\phi_c=\cos^{-1}\left(\sqrt{\left(1-E/E'\right)}\right)$$

A very important consideration in modeling the transport of electrons through the interface was found to be multiple crossing of the interface. The path of an electron, determined by a sequence of collisions, may carry it from the coating film back to the photocathode. Such an electron was given a probability, P(E), to be absorbed in the photocathode. Naturally, it could return to the coating film with the probability (1-P(E)). For the purpose of calculating P(E), the electron was treated as a wave function under the influence of a double-step potential barrier, as shown in figure 2.10:

(2.4)
$$P(E)=\frac{E'\cdot E+E'\cdot E_{vac}+E\cdot E_{vac}+E^2-4E\sqrt{E'\cdot E_{vac}}+2V_0\cdot E_A\cdot\cos(2d\sqrt{2m_e\cdot E}/\hbar)}{E'\cdot E+E'\cdot E_{vac}+E\cdot E_{vac}+E^2+4E\sqrt{E'\cdot E_{vac}}+2V_0\cdot E_A\cdot\cos(2d\sqrt{2m_e\cdot E}/\hbar)}$$

where E is the electron energy relative to the conduction band minimum (CBM) of the coating film, $E_{vac}=E-E_A$ is the electron energy in vacuum, E' is the electron energy relative to

the CBM of the photocathode, V_0 is the difference between the CBM of the coating film and the photocathode, d is the coating film thickness and m_e is the electron mass.

4. Photoelectron transport through the coating film.

The model [48,76,77] treats the transport in the coating film as a classical process, composed of a sequence of electron-phonon scatterings, each modifying the electron energy and direction. Although it is a classical model, some of the parameters, such as the mean-free-path between collisions, are calculated using a quantum mechanics approach The photoelectrons induced in the photocathode have energy of 0-4eV, which is less than the energy gap of the alkali-halide coating film (typically 6eV). Therefore, the photoelectrons cannot release another electron from the coating film, and the dominant interactions are those of the electrons with the lattice vibrational modes. The model takes into account both optical and acoustic phonon-electron interactions. It assumes that the acoustic phonon-electron scattering is a pseudo-elastic process, due to the low energy exchange and almost isotropic electron angular deflection involved in such interaction. Although evaporated alkali-halide films are polycrystalline, the coating film is considered as a perfect single crystal. Impurities, and lattice defects are not accounted for. For a more detailed discussion of the model treating successfully electron transport in alkali-halide films see [48,76,77].

5. *Photoelectron escape into vacuum.*

A photoelectron reaching the surface of the coating film with an energy E greater than the coating film electron affinity, would be emitted into the vacuum with the same probability $P_{vac}(E)$ as a wave function passing a potential step of amplitude of E_A:

$$P_{vac}(E) = 4\sqrt{(E \cdot Evac)}/\left(E + Evac + 2\sqrt{(E \cdot Evac)}\right) \quad (2.5)$$

In order to follow the trajectory of photoelectrons from the photocathode across the interface into the coating film, we need to know their correct energy distribution. We used the experimental distributions, as mentioned above, but they need to be corrected because they were measured after emission into vacuum (across the electron affinity barrier) while we need them inside the material just before emission. Two possibilities exist:

1. Using data from thinly coated photocathode (50Å CsI or CsBr) and correcting for the coating E_A, This has the advantage that it already includes the effects due to transport through the interface, which we cannot treat rigorously. The corrected distribution follows the realtion:

$$P_{in}(E)=P_{meas}(E_{vac}-E_A)/P_{vac}(E) \quad (2.6)$$

where $P_{in}(E)$ is the probability for an electron of energy E before the escape into vacuum and $P_{meas}(E)$ is the measured probability for an electron of energy E to be emitted into vacuum.

2. Using data from bare photocathodes and correcting for the difference between photocathode electron affinity (E_A^{PC}) and the interface barrier (V_0). In this case the corrected distribution follows the relation:

$$P_{in}(E)=P_{meas}(E_{vac}-E_A^{pc}+V_0)/P_{vac}(E+V_0) \quad (2.7)$$

2.2.2 The Monte-Carlo calculations

The Monte-Carlo (MTC) approach, which is a purely numerical method, is a statistical sampling technique making use of random numbers in order to solve a problem. This method was successfully applied from the early 1940's to a wide range of scientific problems. A complete review of the theoretical and practical aspects of the MTC approach can be found in [78].

In the electron transport field, the MTC technique appears to be a natural method for simulating the physical interactions undergone by the considered electrons along their path. We used direct simulation in which the sampling is directly performed from well-characterized single scattering laws and the trajectory of the particle is followed interaction by interaction. Two basic assumptions were utilized in our direct MTC calculations:

- The scattering centers are randomly distributed. Therefore the electrons interact at random points within the material bulk.
- The interactions of the incident electrons with the solid take place locally and instantaneously. Hence, between two successive scatterings, the electron can propagate freely, its energy and momentum remaining unaltered. The trajectory of such an electron moving within the solid can thus be described as a succession of straight lines connected at the points where the collisions occur and where the electron energy and direction are changed.

More details concerning the direct MTC scheme and its flow chart can be found in ref. [79].

The probability of an electron, induced by a photon of an energy hν, to be emitted from a coated photocathode and the energy distribution of the photoelectrons induced by photons of that energy were calculated as follows:

1. The probability of an electron of energy E to be emitted into vacuum and the energy distribution induced by N such electrons were calculated. The electron was "injected" into the coating film at a known initial position. E was varied in steps of 0.025-0.1eV.
2. The weighted average of the transmission probability and of the electron energy distribution was calculated. The weight distribution is the initial energy distribution (eq. 2.5) and it represents the probability of an electron of energy E to be present at the initial position, when illuminating the photocathode with photons of energy hν.

In order to determine the value of the free parameter, E_{loss}, we calculated and minimized the difference between simulation and measurement as a function of E_{loss}. We varied E_{loss} between 0 and 0.5eV. This variation resulted in a negligible effect on the energy distribution. However, the QE attenuation length, L, (see discussion in section 2.3.2.3) was clearly affected by the variation of E_{loss} as can be seen in figure 2.11. Figure 2.12 shows the difference between simulated and measured QE attenuation length, Δ, as a function of E_{loss}, where Δ is defined by:

$$\Delta = \sum_{\substack{\text{photon-energy} \\ \text{coating-film}}} \left(L_{calculated} - L_{measured}\right)^2 / N \qquad (2.8)$$

and N is the number of photon energies and coating films. The minimum value of Δ was found at E_{loss} value of 0.20±0.03eV.

The convergence of the simulation results as a function of the number of simulated events, N, was tested for $N=10^2 - 10^7$. The number of simulated events was chosen to be 10^5 and 10^6

for calculations of the transmission probability and the energy distribution, respectively. This number provided a typical statistical uncertainty of about 2%.

It was also useful to check the statistical behavior of the MTC calculation, for a given number of events. For this purpose, five independent simulations were performed and compared, each of 10^5 events of 1eV electron transport through a 30nm thick CsI film on a K_2CsSb photocathode. The obtained transmission probability overlapped within 2%.

The number of times an electron trajectory passed from the coating film to the photocathode and back to the coating film varied with the electron energy, film thickness and the value of V_0. It was typically 3 for an electron with an initial energy of 1eV and could reach 11 for electrons with initial energy of 4eV.

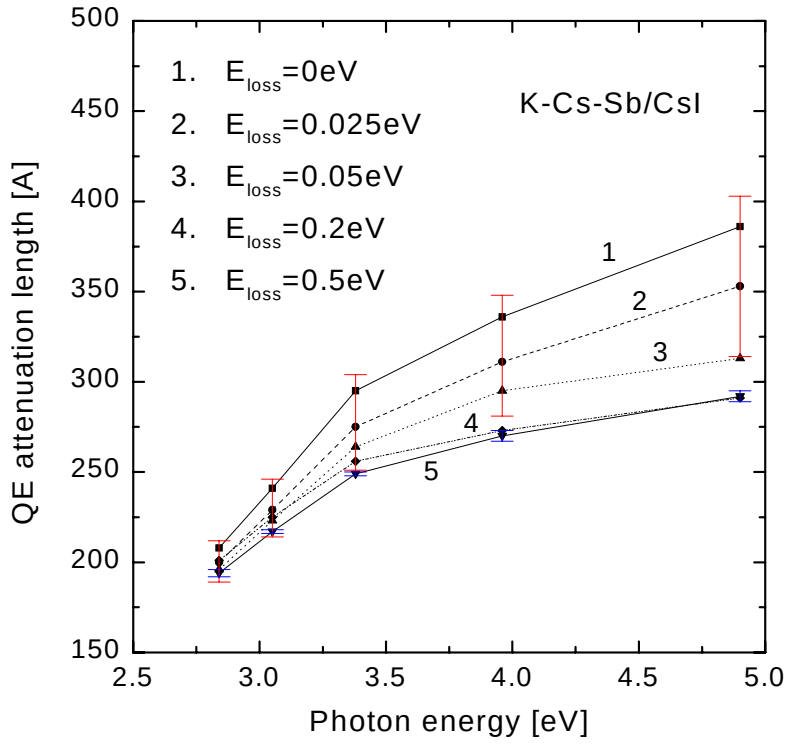

Fig. 2.11: *The QE attenuation length in CsI on a K-Cs-Sb photocathode, as a function of the photon energy, calculated for different values of the free parameter E_{loss}. The error bars originate from the fit to exponential decay, and cover 90% of all possible fits. For the purpose of clarity only the error bars of the curves representing E_{loss}=0.2eV and 0.025eV are displayed.*

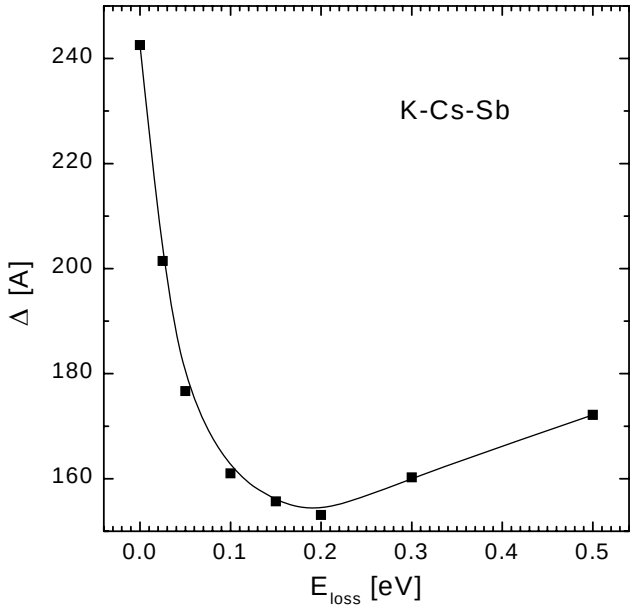

Fig. 2.12: *The difference, Δ, between simulated and measured QE attenuation length in CsI- and CsBr-coated K-Cs-Sb photocathodes as a function of the free parameter* $E_{loss.}$

2.3 Results

The stoichimetric formula of the photocathodes prepared in this work was not investigated systematically. In order to determine the exact formula, one would need to investigate the influence of the preparation parameters on the stoichiometry. This was not within the scope of this work, which focussed on the study of the coatings of these photocathodes. Therefore, Although Cs_3Sb and K_2CsSb are the most probable formulas we will use the general notation Cs-Sb and K-Cs-Sb throughout this work when referring to our results.

2.3.1 Bare alkali-antimonide photocathodes

Cs-Sb and K-Cs-Sb photocathodes have been prepared routinely in our setups. Figure 2.13 shows the distribution of the absolute QE spectra of 22 K-Cs-Sb and 29 Cs-Sb photocathodes produced in our first setup. The mean QE values for Cs-Sb are superior to 15% at 250-350nm and are typically 30% at 185-325nm for K-Cs-Sb. A comparison of the spectral sensitivity of our photocathodes and commercial vacuum photomultipliers photocathodes is presented in figure 2.14. The photocathodes quality in the spectral range of 250-450nm is comparable to that seen in commercial products. Both K-Cs-Sb and Cs-Sb photocathodes were found to be stable in vacuum and in high purity methane (fig. 2.15) over periods of a few days.

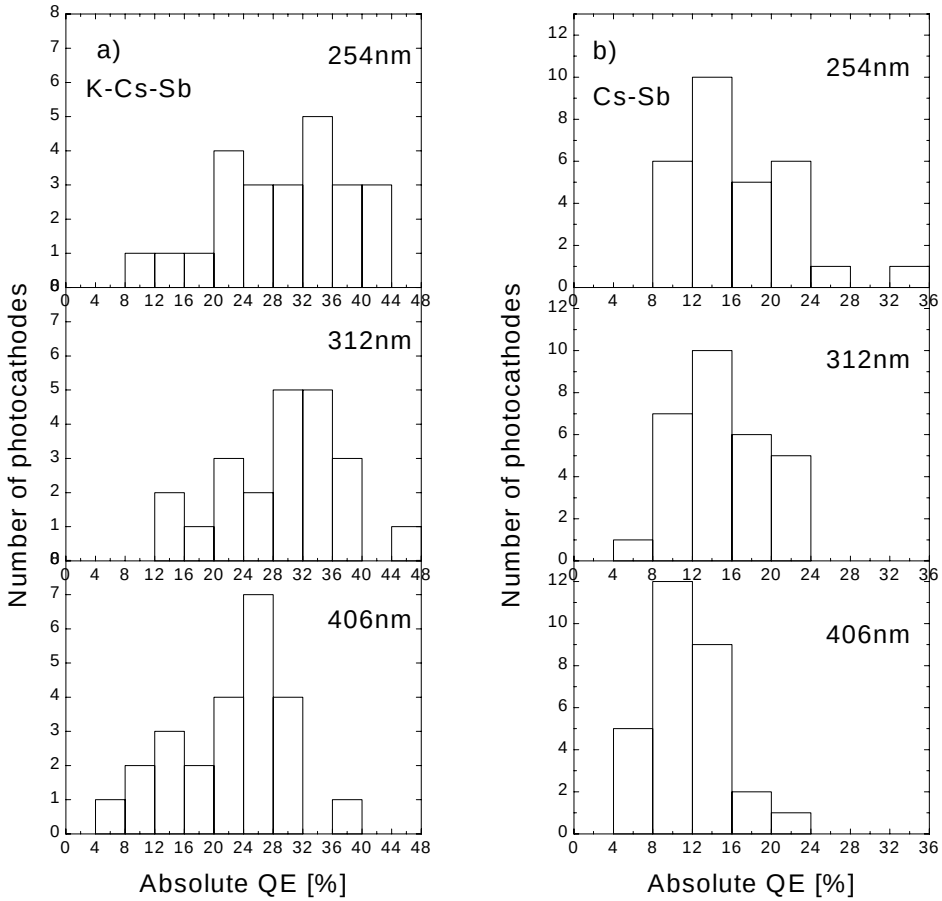

Fig. 2.13: *Distribution of the absolute quantum efficiency values at 254, 312 and 406nm of reflective photocathodes prepared in the setup shown in fig. 2.1. a) 24 K-Cs-Sb photocathodes, the average and rms values, in percents, are 30±9, 32±11 and 22±8 at 254, 312 and 406nm, respectively. b) 29 Cs-Sb photocathodes, the average and rms values, in percents, are 17±6, 15±4 and 12±3 at 254, 312 and 406nm, respectively.*

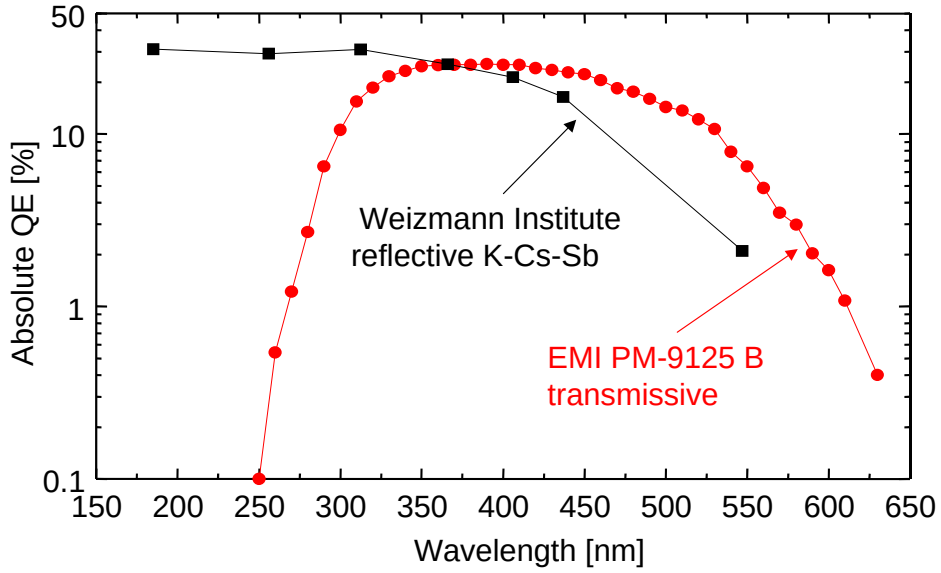

Fig. 2.14: *Absolute QE spectra of a typical K-Cs-Sb photocathode prepared at our setup and of a commercial (EMI PM-9125 B) photocathode of the same type. The decrease in QE of the commercial photocathode at short wavelengths is due to window light transmission.*

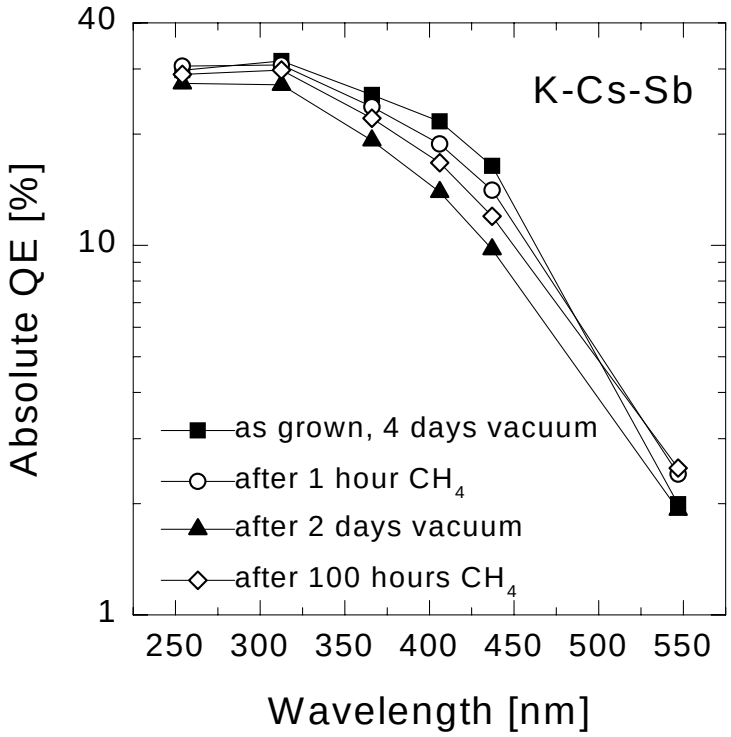

Fig 2.15: *Absolute QE spectra of a bare reflective K-Cs-Sb photocathode in vacuum and in high-purity methane. The photocathode was kept in vacuum, after preparation, for 4 days, then exposed to methane for 1 hour. The chamber was re-pumped and the photocathode kept in vacuum for 2 more days and finally exposed to methane for 100 hours followed by pumping of the chamber. All measurements were performed in vacuum.*

2.3.2 Coated photocathodes

Most of the results in our search for protective layers are summarized in articles [80-86] We tried protecting the photocathodes with materials of three types: oxides (SiO), organic molecules (n-$C_{36}H_{74}$: HTC, ($[CH_3(CH_2)_{16}COO]_2Ca$: CaSt) and alkali-halides (NaI, CsI, CsBr, NaF, CsF).

Some oxides can be very effective protective films, even at extremely thin films. Indeed, native layers of SiO_2 and Al_2O_3 provide efficient sealing from further oxidation of Si and Al. [87,88].

HTC is a long-chain paraffin insulator that can be vacuum-evaporated and is stable in ultra high vacuum and in ambient air [89]. It was reported to have negative electron affinity [90]. CaSt was reported to have a very long electron escape length when forming an organized film [69]. It can be evaporated and is stable in vacuum [70].

Alkali-halides were investigated thoroughly both experimentally [2,63,75,91-95] and theoretically [96-100]. They are known to have good electron transport properties and some are quite stable in ambient air. Their deposition in vacuum is a simple procedure.

The results of oxide and organic protecting layers are summarized in [81]. In general, these attempts as well as the alkali-fluoride coatings were unsuccessful both in terms of low residual absolute QE and poor protection capability of the coated photocathodes when exposed to oxygen.

The most stable photocathodes were achieved with 280Å CsBr, 190Å NaI and 315Å CsI on Cs-Sb and with 335Å CsBr, 225Å NaI and 280Å CsI on K-Cs-Sb photocathodes. Films of a few hundred angstroms thickness were chosen in order to obtain stability in oxygen environment while maintaining a reasonable QE.

2.3.2.1 Chemical composition

The stoichiometry of alkali-antimonide photocathodes is changing with the photocathode depth [101]. This is the result of the preparation procedure, which includes successive evaporations of Sb, K and Cs. A stiochiometry of K_2CsSb on the surface is commonly expected [59].

We used XPS to determine the chemical composition at the photocathode surface. Two sets of measurements were carried out, in the first we characterized bare and CsBr-coated K-Cs-Sb photocathodes, and in the other we investigated CsI-coated K-Cs-Sb photocathodes. Tables 2.3 and 2.4 summarize the atomic concentration of the elements on the surface of the different photocathodes.

	K-Cs-Sb	K-Cs-Sb/50Å CsBr	K-Cs-Sb/320Å CsBr
Cs	4.9±0.2	29±1%	46±2%
Br	---	20±1%	34±2%
K	35±2%	14.5±0.7%	1.5±0.1%
Sb	1.5±0.1%	1.3±0.1%	<0.05%
O	43±2%	16.0±0.8%	6.5±0.3%
C	15.6±0.8%	16.6±0.8%	11.0±0.6%
I	---	0.15%	~0.5%
Si	<1%	<2%	<0.6%

Table 2.3: The elemental atomic concentration on the surface of bare and CsBr-coated K-Cs-Sb photocathodes measured by XPS.

	K-Cs-Sb/50Å CsI	K-Cs-Sb/250Å CsI	K-Cs-Sb/500Å CsI
Cs	17±1%	43±2%	41±2%
I	11±1%	41±2%	40±2%
K	35±2%	1.2±0.1%	2.3±0.1%
Sb	2.9±0.1%	---	---
O	25±1%	6.9±0.3%	7.4±0.4%
C	9.0±0.5%	7.3±0.4%	9.0±0.5%
Si	---	---	---

Table 2.4: The elemental atomic concentration on the surface of CsI-coated K-Cs-Sb photocathodes measured by XPS

Despite using the special vacuum transfer facility, the bare photocathode was contaminated, probably during transfer to the XPS, as can be seen from the dominant presence of carbon and oxygen (59%). Therefore, one cannot draw any exact conclusion from its chemical composition. However, the high concentration of K on the surface as well as its presence on the surface of the photocathodes coated with 50Å thick films and even on the thick coatings is surprising. This may be the result of oxidation and diffusion of K to the surface as will be discussed later. The small presence of Sb on the surface is expected since it is the first element to be evaporated and it is covered with K and Cs. The 50Å coatings may be insufficient for a full coverage of the underlying photocathode. This can be seen from the greater presence of oxygen (and moisture), interacting with the photocathode, on its surface. The thicker coatings protect the photocathode from reaction with oxygen and moisture.

The Cs-to-Br ratio on the surface of the CsBr-coated photocathodes is 1.3 and was also measured for CsBr photocathodes (section 3.2.2). A possible explanation to the excess of Cs is the induction of a photolysis effect by the x-rays, breaking the ionic bonds between Cs and Br. Since Br has a high vapor pressure compared to Cs (at room temperature the vapor pressure of Cs is 0.75×10^{-6}Torr while that of Br is 180Torr [102]), it evaporates, leaving the surface with an access of Cs. It is also possible that the thermal evaporation of CsBr, breaking the ionic bonds, results in the observed stoichiometry. The Cs-to-I ratio on the surface of the CsI-coated photocathodes is approximately 1. Since the vapor pressure of I is lower than that of Br (at room temperature the vapor pressure of I is 4.5×10^{-2}Torr [102]) this may support the first hypothesis. Si originates from the quartz substrate while the presence of I in the CsBr-coated photocathodes is a result of a contamination in the evaporation chamber.

In order to measure chemical composition depth profiles, Ar^+ sputtering and XPS were used alternately. The Ar pressure was typically 10^{-7}Torr and the sputtering steps were 60-120 seconds long. One should note that the sputtering itself might have influenced the results due to a few processes. The first is the breaking of chemical bonds in the sample, leaving some elements free to re-bond to elements in the residual gas. Another process occurs when sputtered material returns to the surface. Finally, the chemical composition at a certain depth may be distorted due to different sputtering rates for different materials. On the average the sputtering rate was about 1Å/sec. The uncertainty in the thickness of the sputtered film increases with the film thickness and it is estimated as 10% of the thickness.

The depth profile of a K-Cs Sb photocathode, coated with 320Å thick CsBr film is presented in figure 2.16a. The first sputtering step cleans the surface from carbon. Cs is concentrated on the surface, while K concentration reaches it maximum after 3 sputtering minutes and Sb is concentrated on the substrate. This is the depth profile that was expected

for a K-Cs-Sb photocathode [101]. The substrate is indicated by a strong increase of the oxygen after 4 minutes of sputtering. A stoichiometry of K_2CsSb can be observed close to the quartz substrate, after 220 seconds of sputtering.

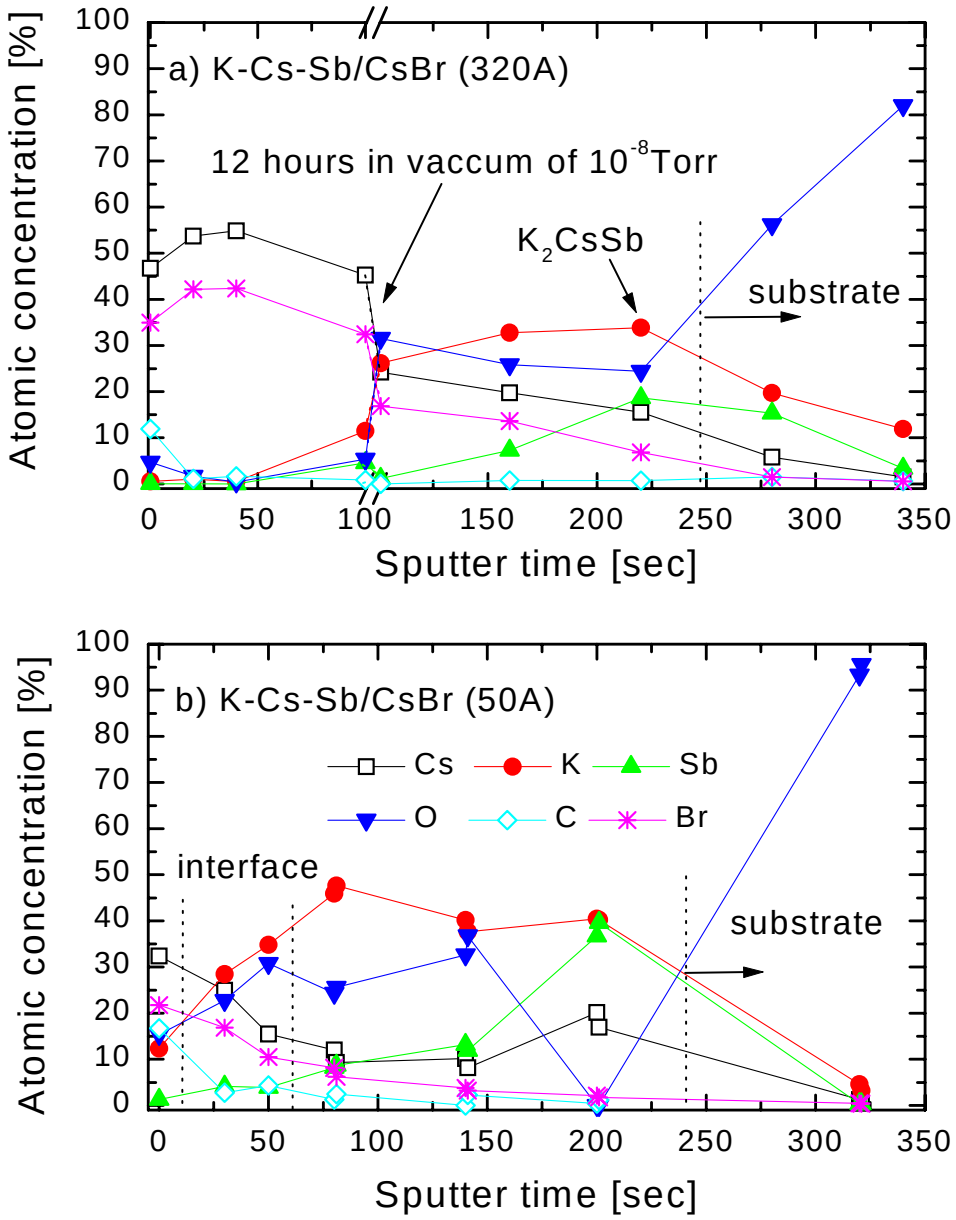

Fig. 2.16: *Depth profiles of the elemental atomic concentrations, obtained from consecutive XPS and sputtering by Ar^+ ions of K-Cs-Sb photocathodes coated with a) 320Å and b) 50Å thick CsBr films. The error in the atomic concentration is 5%, the error in the film thickness, represented by the sputtering time is 10%. The break at 100 sputtering seconds in a) represents 12 hours between consecutive XPS measurements, without further sputtering.*

The photocathode was sputtered for approximately 100sec and its chemical composition was measured immediately after sputtering and again after 12 hours in vacuum of 10^{-9}Torr. The 12 hours interval resulted in a dramatic increase in K and oxygen concentration and a strong decrease in Cs and Br concentration (see the dotted lines in fig. 2.16a). The Cs and Br do not diffuse into the photocathode as can be seen in the following sputtering steps. This was

accompanied by a shift of 0.5ev in the K line, showed in fig. 2.17, indicating its oxidation. This measurement gives an insight to the processes occurring when the photocathode is exposed to oxygen and humidity. The K oxidizes and diffuses to the surface covering the Cs and Br.

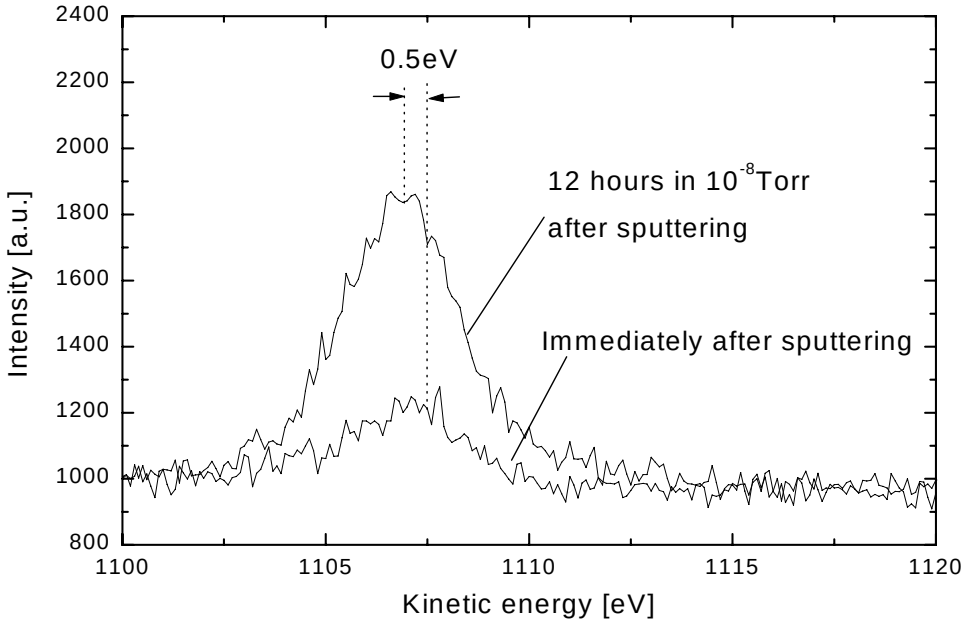

Fig 2.17: *The K_{2S} XPS line measured from an ion-sputtered K-Cs-Sb photocathode coated with 320Å thick CsBr film. The two consecutive XPS measurements were performed at a time interval of 12 hours, in which the photocathode was kept in a vacuum of 10^{-8}Torr. The shift indicates oxidation of the potassium.*

The 50Å thick coating depth profile is presented in fig. 2.16b. As was previously discussed, the thin film does not result in full coverage of the surface and some K is observed on the surface. Indeed, the thin coating does not protect the photocathode from oxygen as is indicated by a large concentration of oxygen on the surface and underneath. In this sample the Br concentration decreases after 50 seconds of sputtering. This is with good agreement with the estimation of a sputtering rate of 1Å/sec. The substrate was reached after about 5 minutes of sputtering, indicating a photocathode thickness of ~250Å. These numbers should be regarded as rough estimations.

The depth profiles of the CsI-coated K-Cs-Sb photocathodes is presented in figure 2.18. In all three samples the Sb presence reaches its maximum on the substrate, while K is dominant in the rest of the photocathode. There seems to be a deficiency of Cs and an excess of Sb in the photocathodes. The photocathode-coating film interface can be estimated to be where I presence is decreased while K and Sb concentrations increase. As expected, the interface has a width with an upper limit that can be roughly estimated from fig 2.18 a) and b) to be 80Å. It is important to note that some of the measured width is due to the uncertainty in the film thickness and to the sensitivity of the XPS to a few tens of Å below the surface. The substrate is indicated by an increase in Si and O presence.

The 50Å thick coating results in a partial coverage of the surface, as is obvious from the small fraction of Cs and I on the surface. For this reason the photocathode-coating film interface position cannot be estimated. It is also clear that the oxygen diffused into the

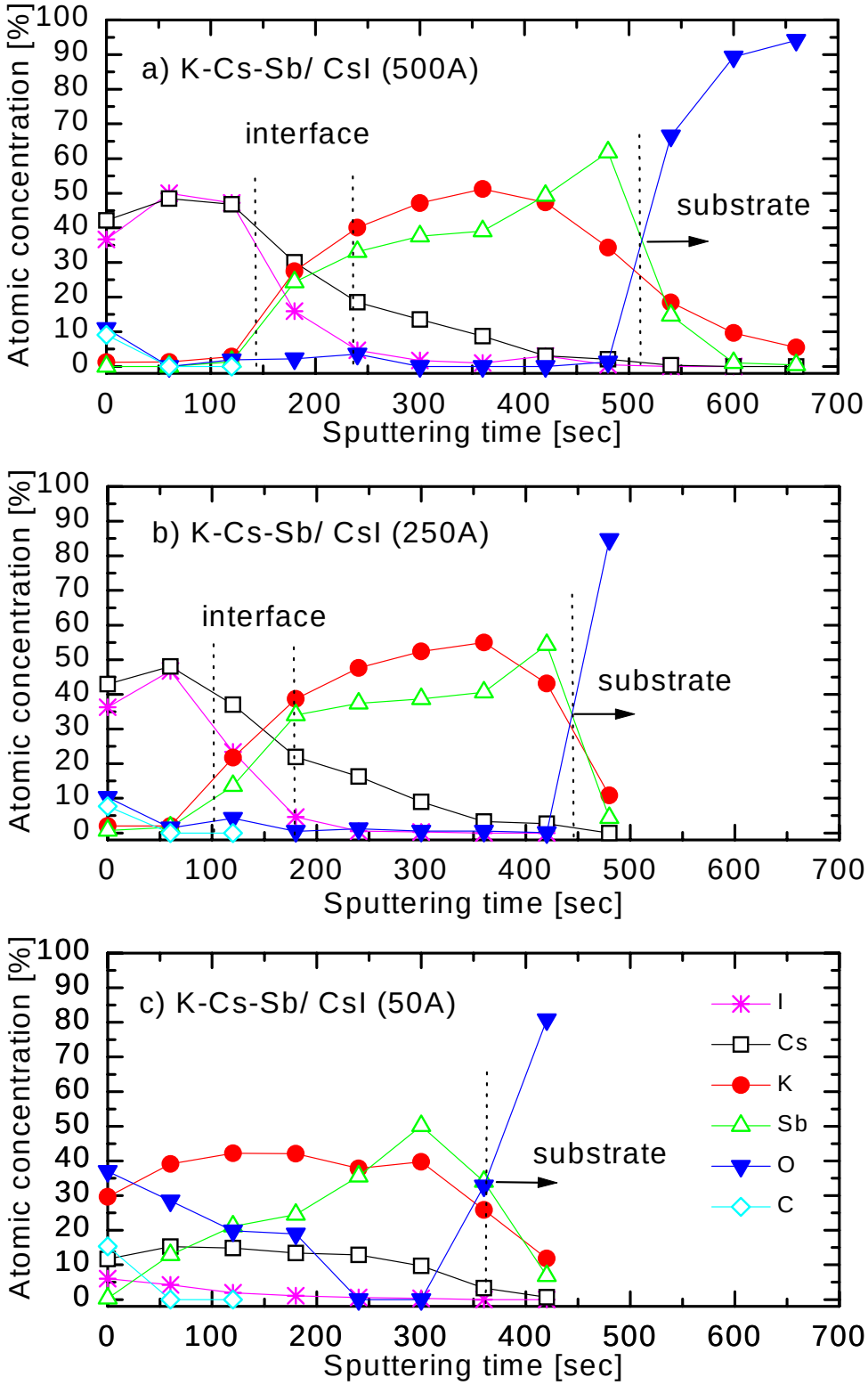

Fig. 2.18: *Depth profiles of the elemental* ***atomic concentrations, obtained from consecutive XPS and sputtering by*** Ar^+ ***ions of K-Cs-Sb photocathodes coated with a) 500Å b) 250Å and c) 50Å thick CsI films. The error in the atomic concentration is 5%, the error in the film thickness, represented by the sputtering time is 10%.***

photocathode, as its concentration is decreasing gradually from 35% at the surface to 0% at the substrate interface. There is an excess of K, observed over the first 200 seconds of sputtering. For example after 75 seconds the stoichiometry is $K_{2.7}CsSb$. this may be related to the exposure of the photocathode to oxygen discussed above.

The two thicker films present a clear coating of CsI. The exposure of the surface to O seems to affect a very thin layer (~10Å), where I presence is slightly reduced. However, a Cs-to-I ratio of 1 is preserved below that layer. At the photocathode-coating film interface the decrease in the concentration of I is faster than that of Cs, because the latter originates also from the photocathode. One can also observe an increase in the presence of O at the photocathode-coating film interface. This may indicate the oxidation of the photocathode in its preparation chamber, before its coating with CsI. However, the presence of oxygen below the interface is negligible, proving that the coating film protects the photocathode from interaction with oxygen.

2.3.2.2 QE spectra

The QE of coated photocathodes depends, naturally, on the coating film thickness. Figure 2.19 shows the QE spectra, in a reflective mode, of CsBr-coated K-Cs-Sb for different coating thickness.

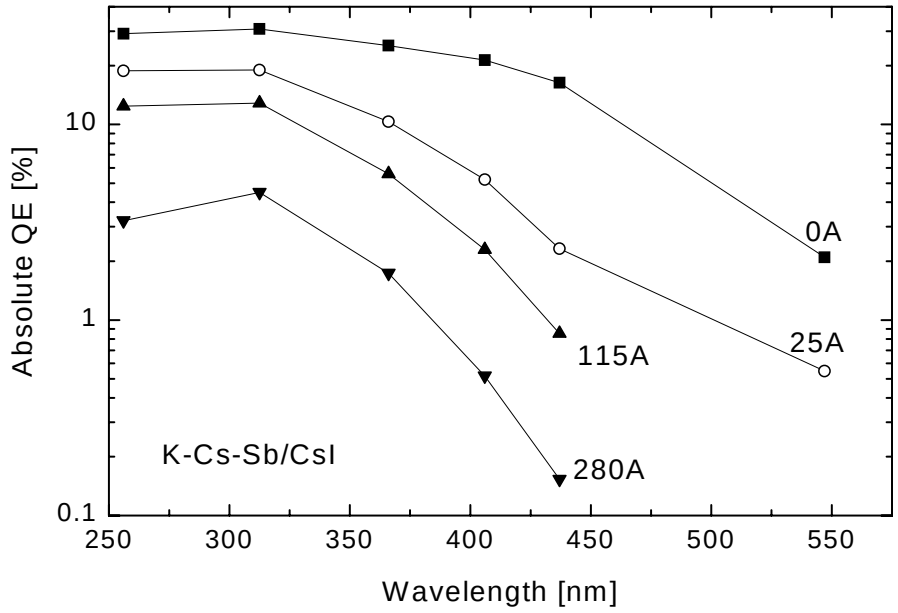

Fig. 2.19: *Absolute QE spectra of a K-Cs-Sb photocathode, Bare and coated with 25Å, 115Å and 280Å thick CsI films, measured in a reflective mode.*

Typical QE spectra of reflective bare and coated K-Cs-Sb and Cs-Sb photocathodes are shown in fig.2.20. The coating films and their thickness presented in the figure are those resulting in a good stability of the coated photocathode in oxygen (see section 2.3.2.5). For other coating materials (CsF, NaF, SiO, HTC and CaSt) the photocathode protection could not be achieved with reasonable QE values. Coating Cs-Sb photocathodes with 315Å thick CsI or 280Å thick CsBr films results in 1-2% QE at 250-375nm, while the 190Å NaI-coated Cs-Sb photocathode has a maximal QE value of 1% at 312nm. Higher QE values were measured for coated K-Cs-Sb photocathodes. The 335Å CsBr-coated and the 280Å CsI-coated K-Cs-Sb photocathodes have a peak of 4.5% at 312nm and QE values superior to 3%

at225-350nm and 185-330nm, respectively. Our best CsBr-coated K-Cs-Sb photocathodes have QE values reaching 7% at 312nm. This value, though about 5 times lower compared to that of a bare photocathode, already has practical applications. Higher QE values (10% at 312nm) can be achieved while maintaining reasonable stability in oxygen by evaporating thinner films, as discussed below (see section 2.3.2.5).

For the CsI-coated K-Cs-Sb photocathodes an increase in the QE is observed at 185nm. This is due to photoemission from the CsI, which by itself is a highly efficient UV photocathode with a photoemission cutoff at 220nm [2]. A similar increase is expected for the CsBr-coated photocathodes at wavelengths shorter than its photoemission cutoff at 170nm [62,63].

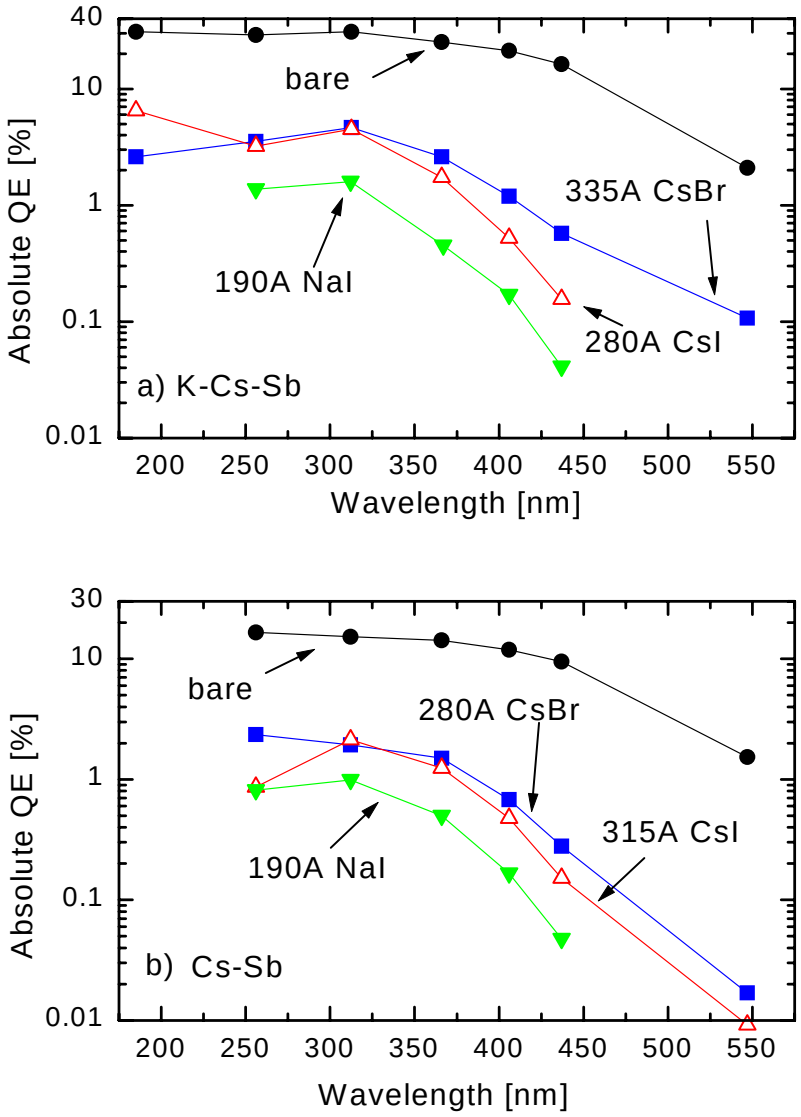

Fig. 2.20: *Typical absolute QE spectra of reflective photocathodes. a) K-Cs-Sb photocathodes: bare and coated with 335Å thick CsBr, 190Å thick NaI and 280Å thick CsI films and b) Cs-Sb photocathodes: bare and coated with 280Å thick CsBr, 190Å thick NaI and 315Å thick CsI films*

2.3.2.3 QE attenuation length

Figure 2.21 shows typical QE attenuation at 312nm as a function of the coating film thickness, for alkali-halide coatings (CsBr, CsI, CsF, NaI, NaF) on K-Cs-Sb and Cs-Sb photocathodes. The smallest attenuation, by a factor of 7, was achieved with CsI and CsBr films on K-Cs-Sb photocathodes. The QE attenuation for organic (HTC and CaSt) and oxide (SiO) coatings on Cs-Sb is presented in figure 2.22. The attenuation of the QE in the alkali-flourides, organic and oxide coatings is much stronger than in CsBr and CsI.

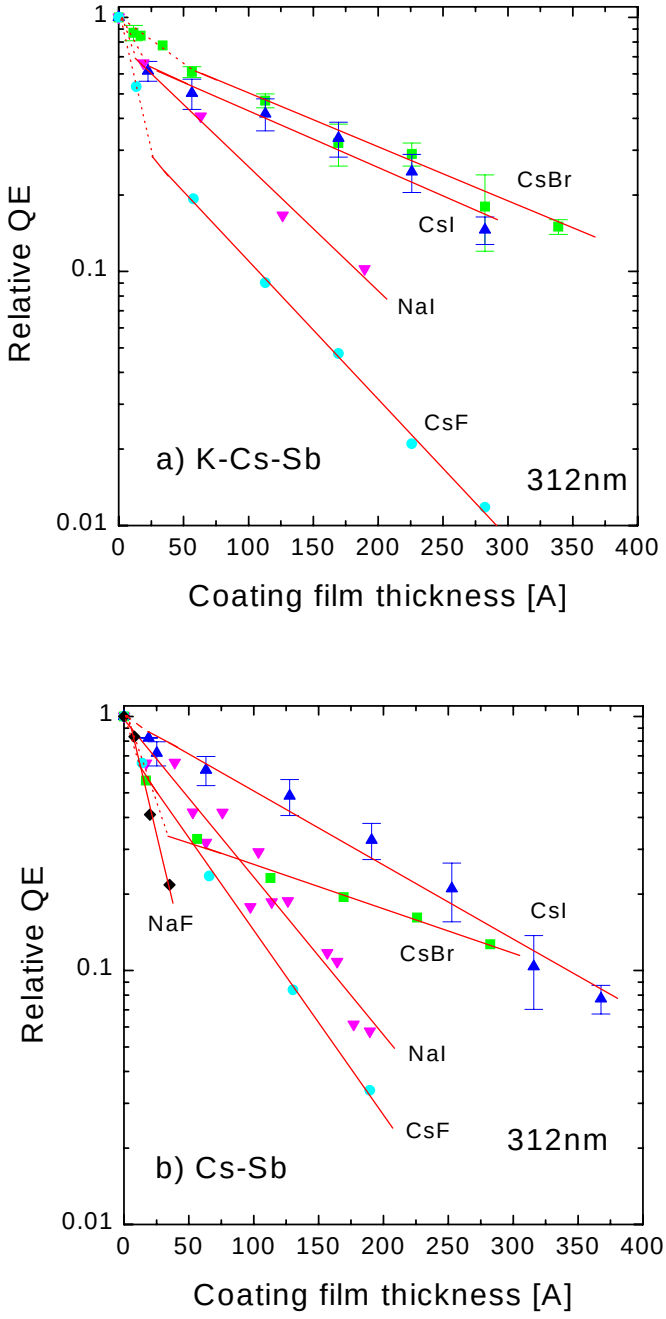

Fig. 2.21: *Relative QE of reflective a) K-Cs-Sb and b) Cs-Sb photocathodes coated with CsBr, NaI, CsI, CsF and NaF protective films, as a function of the film thickness, measured at 312nm (points). Solid lines are exponential fits to the data (excluding the low-thickness points). For the purpose of clarity, only typical error bars are displayed*

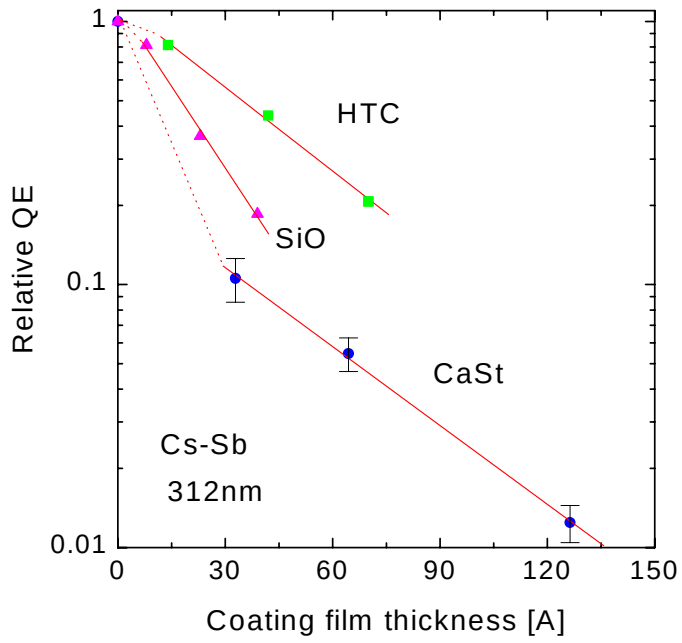

Fig. 2.22: *Relative QE of reflective Cs-Sb photocathodes coated with HTC, CaSt and SiO films as a function of the film thickness, measured at 312nm (points). Solid lines are exponential fits to the data (excluding the low-thickness points).*

The first 10-50Å of the protecting layer may give rise to a strong decrease in QE, followed by an exponential decay for larger film thickness. The initial decrease is probably due to the creation of the new interface between the photocathode and the film, resulting in a change in the electron affinity.

The process of low-energy electron transport through the film explains the exponential decrease observed for thicker films. The slope of the exponential decay represents the attenuation length, L, of the QE, defined as:

(2.9) $$QE(x)\sim\exp(-x/L)$$

where x is the coating film thickness.

(2.10) $$1/L=1/L_e+1/L_{ph}$$

where L_e and L_{ph} are the electron attenuation and photon absorption lengths of the coating film. If the coating film does not contribute to the photon absorption, as is the case in this work, L is determined by the electron attenuation length: $L=L_e$. The electrons induced in the photocathode and injected into the coating film are not mono-energetic. Therefore, the QE attenuation length is related to but differs from the electron escape length because it is a function of the photon energy and not of the electron energy.

The QE attenuation length depends both on the photocathode and on the coating film. This is due to the interface between the photocathode and the coating film, influencing, for very thin films, the structure of the coating film, thus affecting the electron transport through the film.

Figure 2.23 shows the attenuation of the QE of K-Cs-Sb and Cs-Sb photocathode coated with a CsBr film, as a function of the film thickness, at wavelengths of 256nm, 312nm and

437nm. As expected, the QE attenuation over the first 50Å is more pronounced for low energy photons. While the K-Cs-Sb coated photocathode shows the standard transition from the sharp initial decrease in the QE over the first 50Å to the more moderate one for thicker films, the CsBr-coated Cs-Sb shows a unique behavior. The interface thickness is of the order of 100Å, which is considerably larger than any other investigated interface. The transition between the initial decrease and the exponential behavior at large thickness is smooth. It is possible that in this case there was an enhanced diffusion between the photocathode and the interface. However, it is not clear why this was not observed for other interfaces.

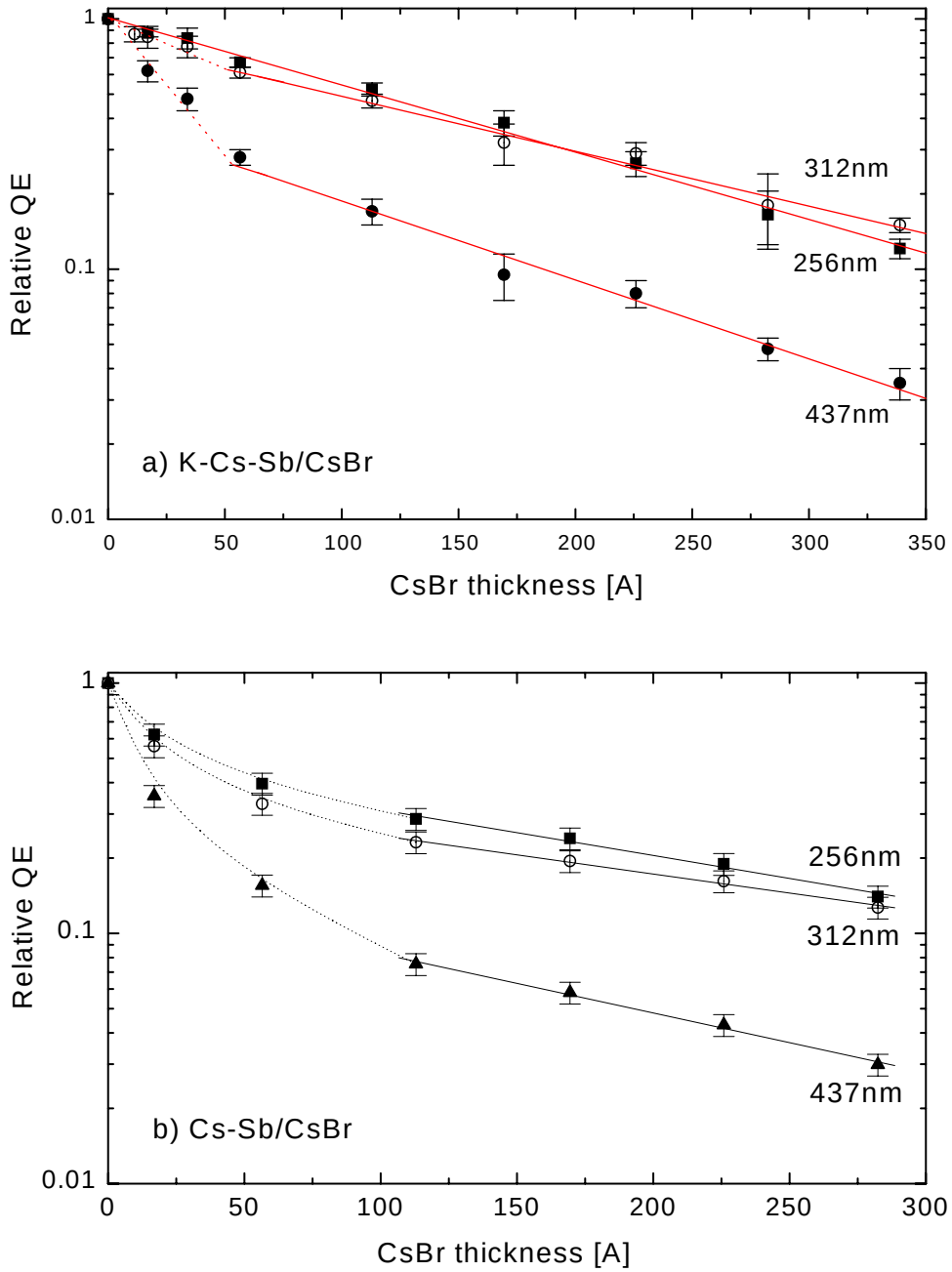

Fig. 2.23: *Relative QE of a reflective CsBr-coated a) K-Cs-Sb and b) Cs-Sb photocathodes, measured at different photon wavelengths as a function of the film thickness. Solid lines are exponential fits to the data (excluding the low-thickness points) shown with dotted line.*

Fig. 2.24 presents the measured QE attenuation length, extracted from the data in fig. 2.21, as a function of the photon energy for alkali-halide coatings on K-Cs-Sb and Cs-Sb photocathodes. CsBr demonstrates the longest attenuation length of the order of a few hundred Å and is followed by CsI, NaI, CsF and NaF. The latest having QE attenuation length of approximately 10Å. With the exception of CsF, the attenuation length has a maximum for photons of 4eV, corresponding to the most energetic photoelectrons emitted from the bare photocathode [51,72,73].

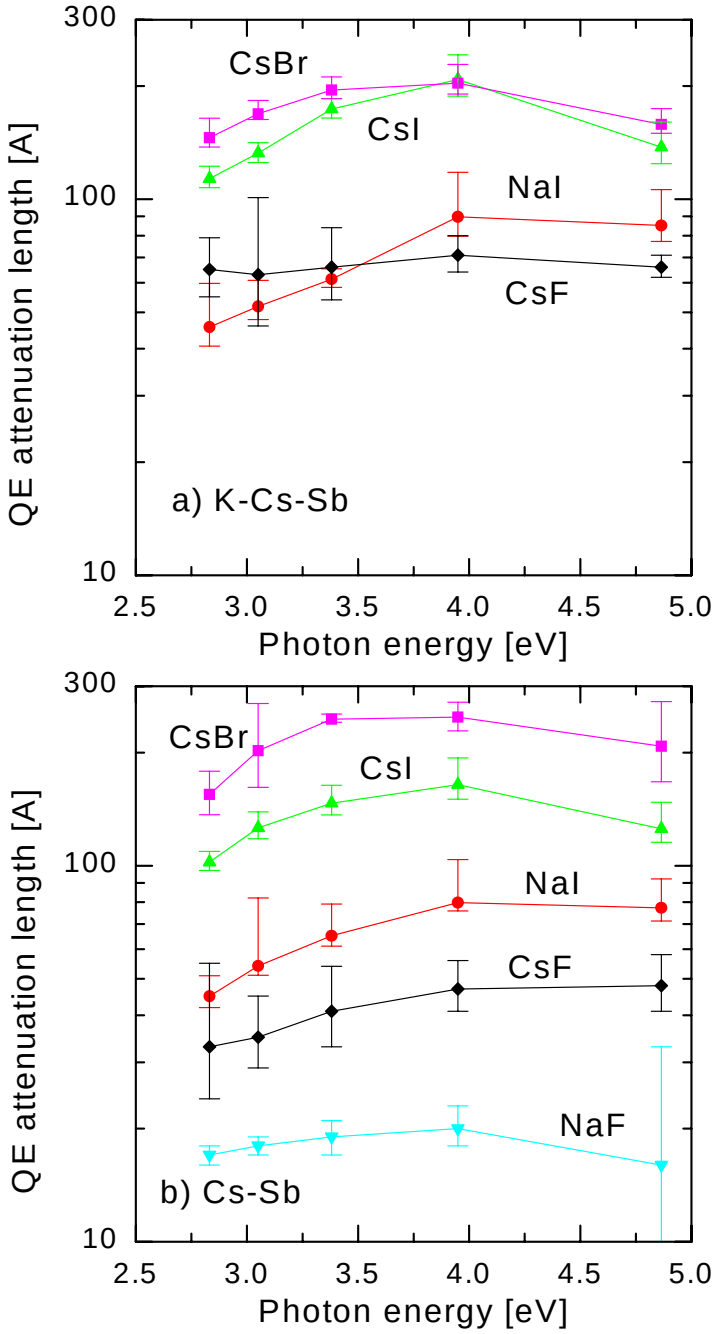

Fig. 2.24: *Measured QE Attenuation length in CsBr, CsI, NaI, CsF and NaF films deposited on a) K-Cs-Sb and b) Cs-Sb photocathodes, as a function of the incident photon energy. The error bars originate from the fit to exponential decay, and cover 90% of all possible fits.*

Figure 2.25 shows the QE attenuation length for HTC, CaSt and SiO coatings, extracted from the data in fig. 2.22. The attenuation length is of the order of a few tens of Å and the maximum at 4eV is not observed as for most of the alkali-halides. The lack of that maximum can be explained by a different electron transport mechanism through the coating film, as can be expected for the organic [69] and oxide films. Another possibility is a chemical interaction between the coating film and the photocathode, influencing the energy distribution of the electrons entering the coating film. The QE attenuation length measured for CsF, NaF, HTC and SiO on alkali-antimonide photocathodes is similar to the one measured by Buzulutskov et al. on CsI photocathodes [68].

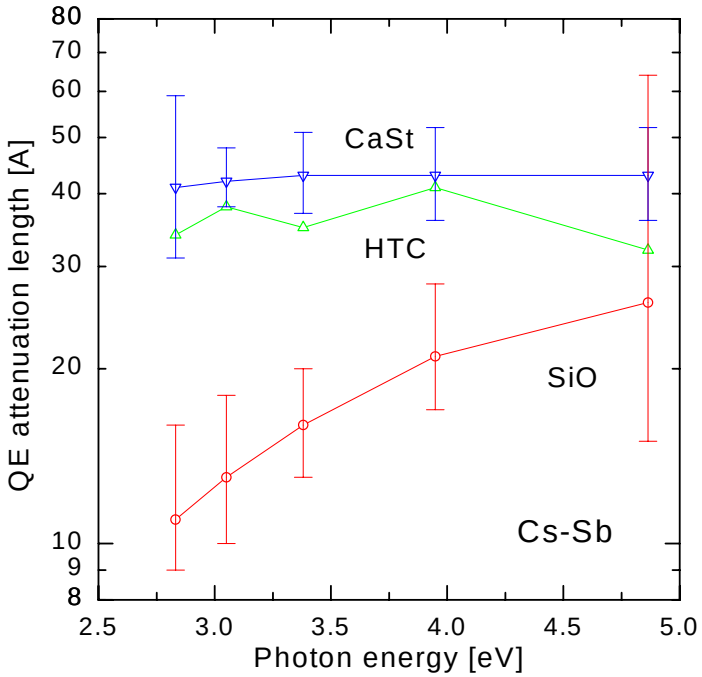

Fig. 2.25: *Measured QE attenuation length in CaSt, HTC and SiO deposited on Cs-Sb photocathodes as a function of the incident photon energy. The error bars originate from the fit to exponential decay, and cover 90% of all possible fits. For the purpose of clarity, the error bars of HTC, of the same order of magnitude as those of CaSt, are not displayed.*

Monte-Carlo calculations of the QE attenuation length based on the model described in section 2.2 were performed. For this purpose we calculated the electron transmission probability for every alkali halide considered and for various film thickness at different photon energies. The thickness was varied from 5nm and up to 35nm with steps of 5nm, in order to keep as close as possible to the experimental procedures. We extracted the QE attenuation length from the slope of the curves of the calculated electron transmission probability logarithm versus the film thickness.

Since there is a spread in the values of the electron affinity available in the literature for alkali-halides considered here, we investigated the sensitivity of the calculated QE attenuation length to fluctuations in the electron affinity. Fig. 2.26 shows the QE attenuation length as a function of the photon energy, calculated for different electron affinity values. The variation in the QE attenuation length is 11% and 5% at photon energies of 2.84 and 4.9eV, respectively. One should note that variation in the electron affinity results in a modification of the initial electron distribution (see equation 2.5). The initial distribution has more low-energy

electrons in the case of lower electron affinity. Since electrons in the energy range of 0-0.5eV are dominant in the case of the low photon energies and since the transmission probability of electrons with less than 0.5eV is strongly attenuated with the film thickness, we observe a short QE attenuation length for low values of electron affinity and photon energy. For higher photon energies, the influence of electrons with an initial energy less than 0.5eV is smaller, therefore this effect of the electron affinity variation is reduced. For the case of higher photon energies, the higher electron affinity results in a shorter QE attenuation length. This is expected, because for thicker films the energy of the electrons reaching the surface is lower, thus they are more affected by an increase in the electron affinity.

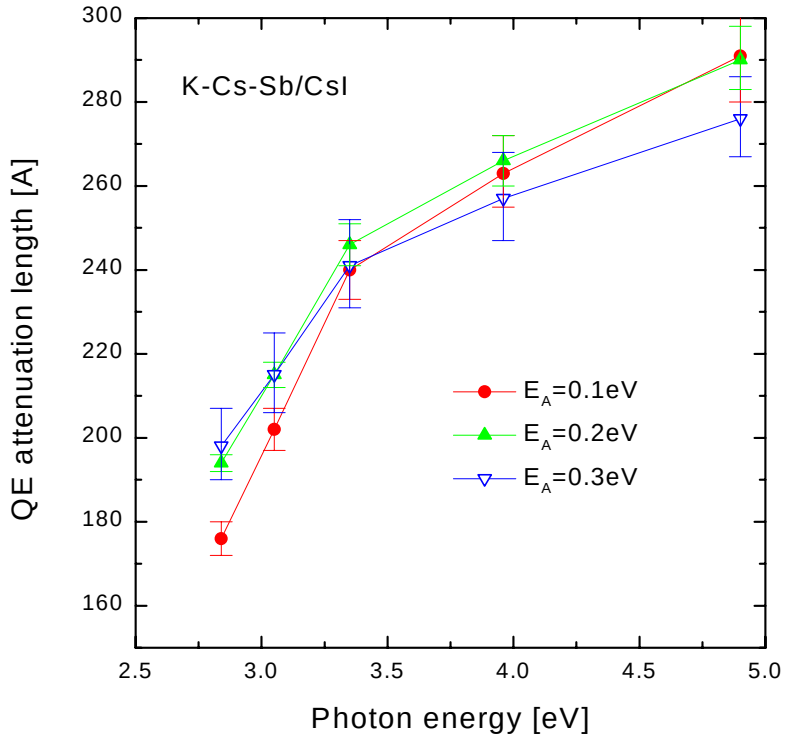

Fig. 2.26: *QE attenuation length in CsI films on a K-Cs-Sb photocathode as a function of the photon energy, calculated for different electron affinity values. The error bars originate from the fit to exponential decay, and cover 90% of all possible fits.*

It is interesting to note that varying the value of V_0 (see figure 2.10) between –1.5eV and 1.5eV resulted in less than 1% fluctuation in the QE attenuation length.

Fig. 2.27 shows two sets of calculations for CsBr-coated K-Cs-Sb photocathodes in which we used different initial electron energy distributions: our own measurements of K-Cs-Sb photocathodes coated with 50Å CsBr (see fig. 2.29), and the data reported in ref. [73]. The QE attenuation length calculated using our own data varies between 88% and 96% of the experimental results for photon energies up to 4eV. The QE attenuation length values calculated using ref [73] are 5 to 35% larger compared to the measured ones. In the model we did not take into account the process involving an electron going from the coating film to the photocathode and exciting another electron. In this case, both electrons would have a low energy resulting in a high probability that neither one would return to the coating film. This process, influencing electrons with energy greater than the photocathode gap energy, is responsible for the measured decrease in the QE attenuation length for photons of 4.9eV.

Indeed, the calculated results do not produce a maximum value for the QE attenuation length at 4eV, and its value for photon energy of 4.9eV is 30% larger than the measured result.

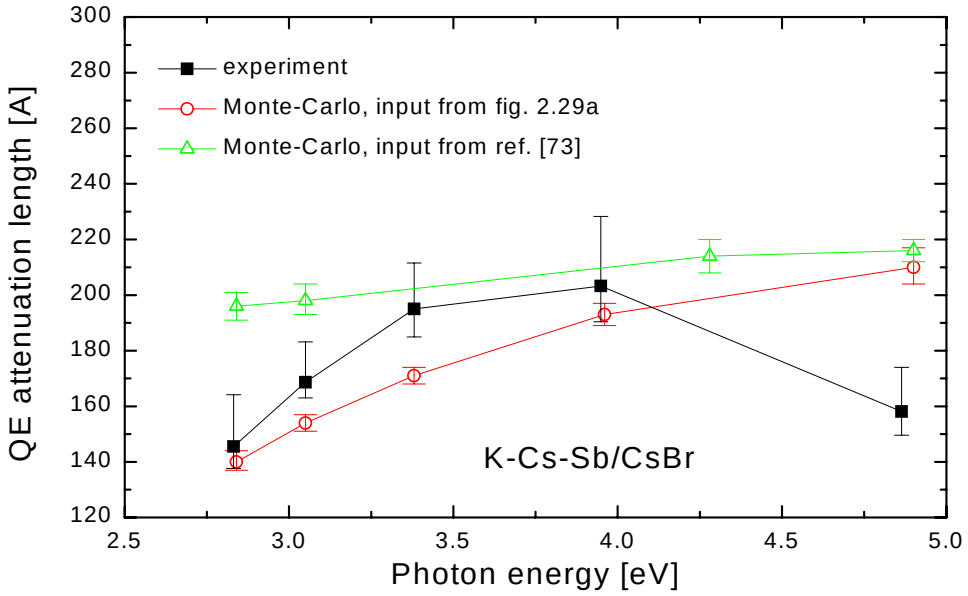

Fig. 2.27: *QE Attenuation length in CsBr films deposited on K-Cs-Sb photocathodes as a function of the incident photon energy. Shown are the QE attenuation length values extracted from measurements, and calculated using ref. [73] and fig. 2.29a as input distributions. The error bars originate from the fit to exponential decay, and cover 90% of all possible fits.*

We also calculated the QE attenuation length using initial electron energy distributions of ref. [51,72,73] for NaI, CsI, and CsBr coatings on K-Cs-Sb and Cs-Sb photocathodes. The results are shown in figure 2.28. In almost all the cases, the calculated values were larger than the measured ones, varying between 75% and 135% for Cs-Sb and 118% to 230% for K-Cs-Sb photocathodes. This could be explained by the grain structure of alkali-halide evaporated films, neglected in our model. It was observed that that the electron escape length in polycrystalline films, decreases with the crystal grain size [103]. A likely explanation for this effect could be the trapping of the photoelectrons at the interfaces between crystellites, as suggested by Cazaux [104]. Since we do not take that trapping into account, the calculated QE attenuation length is longer than the measured values.

It is important to note that the calculated QE attenuation length of CsI is larger than that of CsBr, contradictory to our measured results. This is not understood, and should be further investigated.

For the low-energy visible photons, the difference between calculation and experiment is large. This may originate from neglected impurities and lattice defects, certainly existing in our evaporated films, strongly affecting low-energy electron transport. Another possible reason is that photons in this energy range give rise to photoelectrons of a few tenths of eV. In this low electron energy range, the validity of the electron transport model is questionable, as already discussed in [48,76,77].

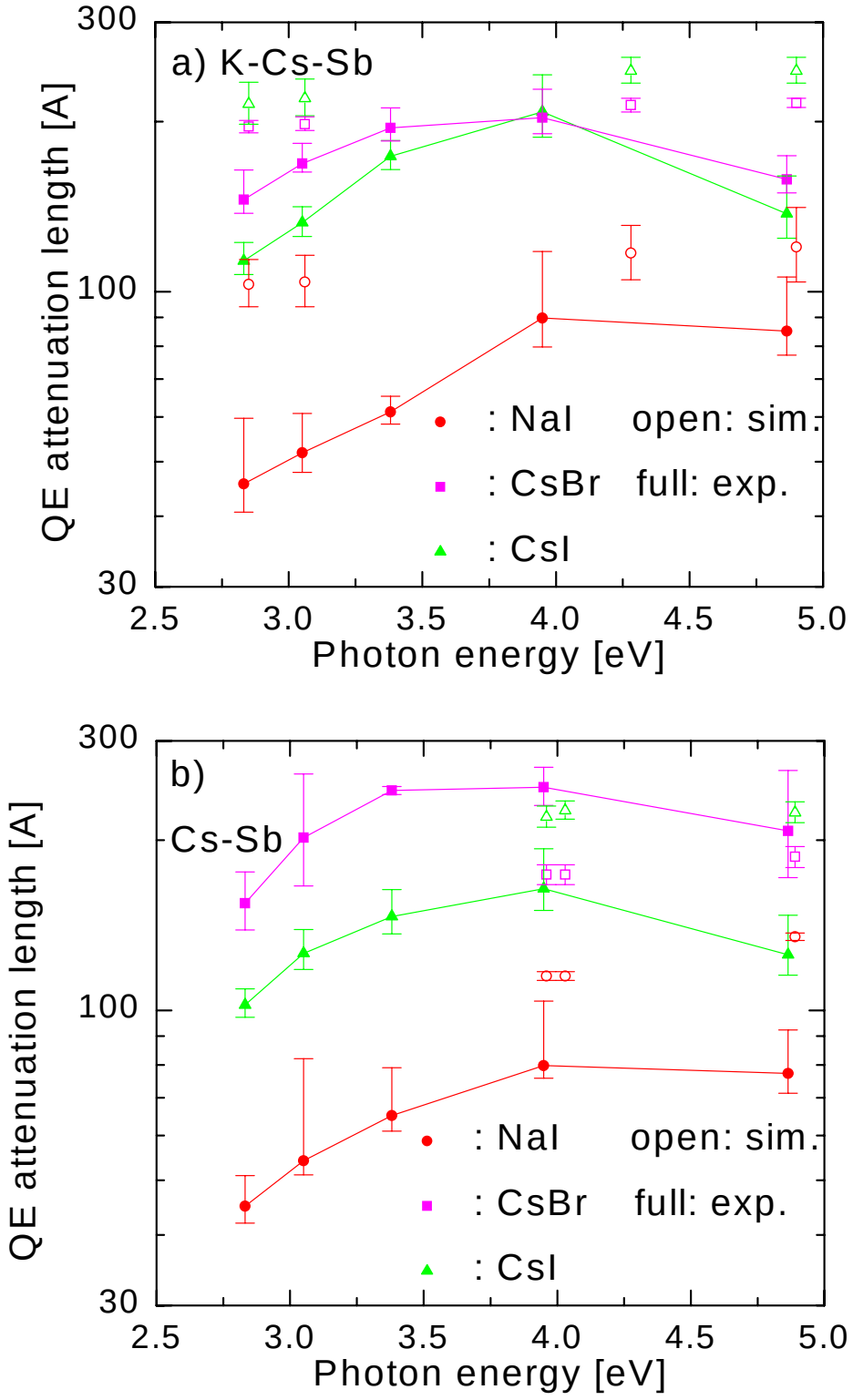

Fig. 2.28: *Measured and calculated QE attenuation length in CsBr, CsI and NaI films deposited on a) K-Cs-Sb and b) Cs-Sb photocathodes as a function of the incident photon energy. The error bars originate from the fit to exponential decay, and cover 90% of all possible fits. The calculation was performed using data from ref. [51,72,73]*

2.3.2.4 Photoelectron energy spectroscopy

The photoelectron energy distributions induced by mono-energetic photons at the 2.85-4.9eV range were measured for K-Cs-Sb photocathodes coated with 50Å and 350Å thick CsBr and with 50Å, 250Å and 500Å thick CsI films. The data, normalized as to have the area under the curve proportional to the QE, is presented in figure 2.29 and tables 2.5-2.9.

For the 50Å CsBr and CsI coatings, the cutoff energy, defined as the highest energy of the distribution, is increasing with the photon energy as was expected. The distribution maximum value is increasing with the photon energy up to 4eV, but for 4.9eV the maximum is at the same or at lower energy compared to 3.96eV. This is another evidence for the onset of a two-electron cascade for photons between 4 and 4.9eV. It is also clear that the shape of the energy distribution for 4.9eV photons is different than that measured for lower energies. This may originate in part from the onset of the two-electron cascade or from photoemission from impurity levels discussed below.

The photoelectron energy distributions measured for thicker coating films (350Å thick CsBr and 250Å and 500Å thick CsI films) are narrower and their peak is at lower energies than that of the thinner coatings. Both effects are more pronounced for the more energetic photons, suggesting that the CsBr and CsI films have larger attenuation for more energetic electrons. Another feature of the thicker film, for CsBr, is that the distribution maximum of 4.9ev photons is the same as for 3.96eV.

The threshold energy for photoemission from the coated photocathode, $E_{threshold}$, was extracted from the cutoff energy, E_{cutoff} and the photon energy, hν:

(2.11) $$E_{threshold} = h\nu - E_{cutoff}$$

E_{cutoff} was extracted from the raw data as the highest energy for which the signal-to-noise ratio is more than 1.5. $E_{threshold}$ was found to be 1.97±0.08eV for the 50Å CsBr coating and 2.0±0.15eV for 350Å thick CsBr coating film.

The threshold energy for photoemission from the CsI coated photocathode was found to be 2.07±0.06eV for the 50Å thick coating, 2.25±0.1eV for 250Å thick film and 2.5±0.2eV for 500Å coating film. One should note that the 50Å thick coating does not result in full coverage of the photocathode surface (see section 2.3.2.1) and this may explain the lower photoemission threshold energy extracted for this film.

Shoulders can be observed in the shape of the electron energy distributions of the CsI-coated photocathodes, indicated in fig. 2.29c-e by arrows. The most pronounced shoulders observed at electron kinetic energies of 0.8 and 1.6eV, for the 250Å thick coating, and at 0.7eV, for the 500Å thick coating, induced by 4.9eV photons. A similar shoulder is observed, for the energy distribution induced by 3.96eV photons, at a kinetic energy of 0.6eV and 0.4eV for the 250Å and 500Å thick coatings, respectively. There may also be a small shoulder for 50Å coating at a kinetic energy of 1.6eV for the 4.9eV-induced distribution.

The origin of the shoulders induced by 3.96eV and 4.9eV photons at electron kinetic energies of 0.6eV and 1.6eV, respectively, are the same, because the energy difference is the same between the two shoulders and the two inducing photons. We believe that this structure is an indication of a photoemission channel, other than the one discussed so far, requiring approximately 3.3eV for photoemission. This is the reason that it is observed only for the two higher energy photons. This photoemission may originate in impurity levels in the photocathode or in the coating film.

Although no internal structure was observed for the CsBr coating, it is possible that the different shape, observed for the 4.9eV photons compared to lower energies at the 50Å thick coating, originates, in part, from photoemission from impurity levels in the CsBr film. This could explain the large number of electrons in the kinetic energy range of 1.5-2eV.

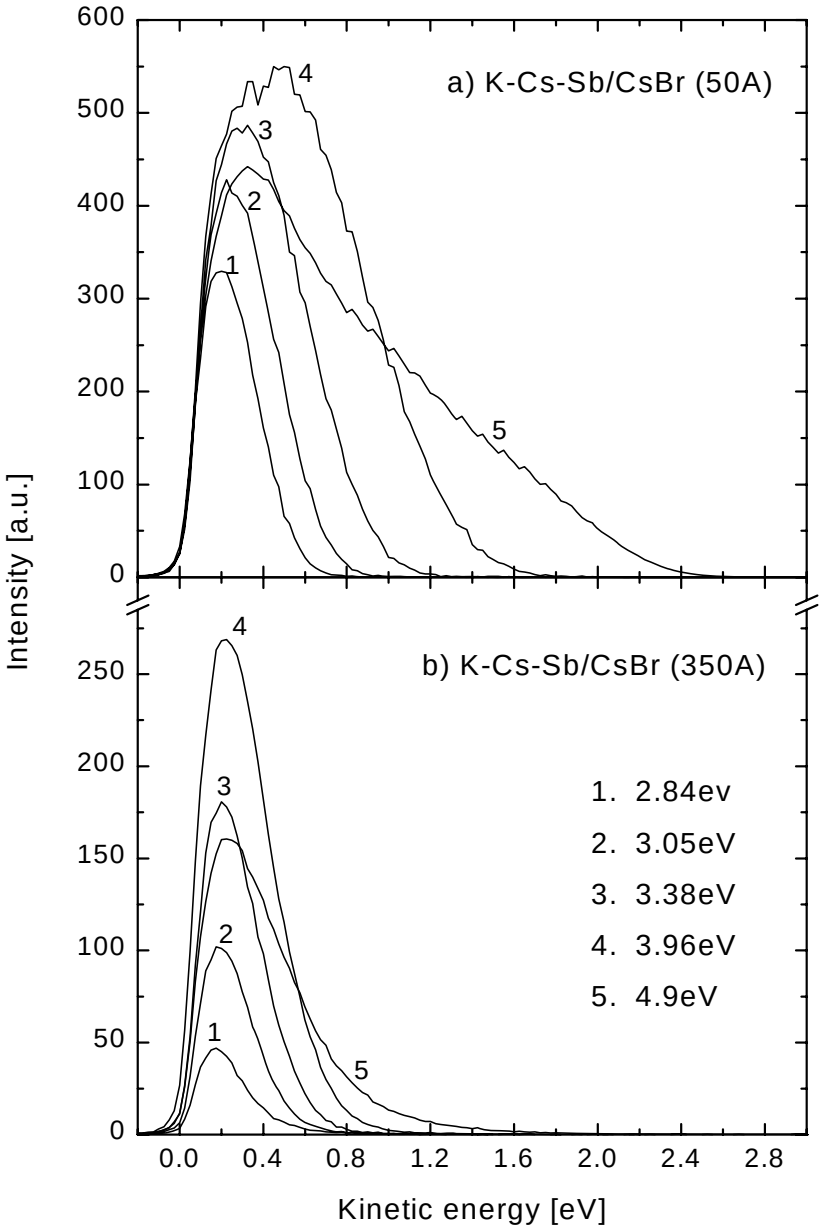

Fig. 2.29: Photoelectron energy distributions from K-Cs-Sb photocathode coated with a) 50Å and b) 350Å thick CsBr films, c) 50Å, d) 250Å and e) 500Å thick CsI films, induced by 2.85-4.9eV photons. The data is normalized as to have the distribution integral proportional the QE. The arrows indicate shoulders in the shape of the photoelectron energy distributions.

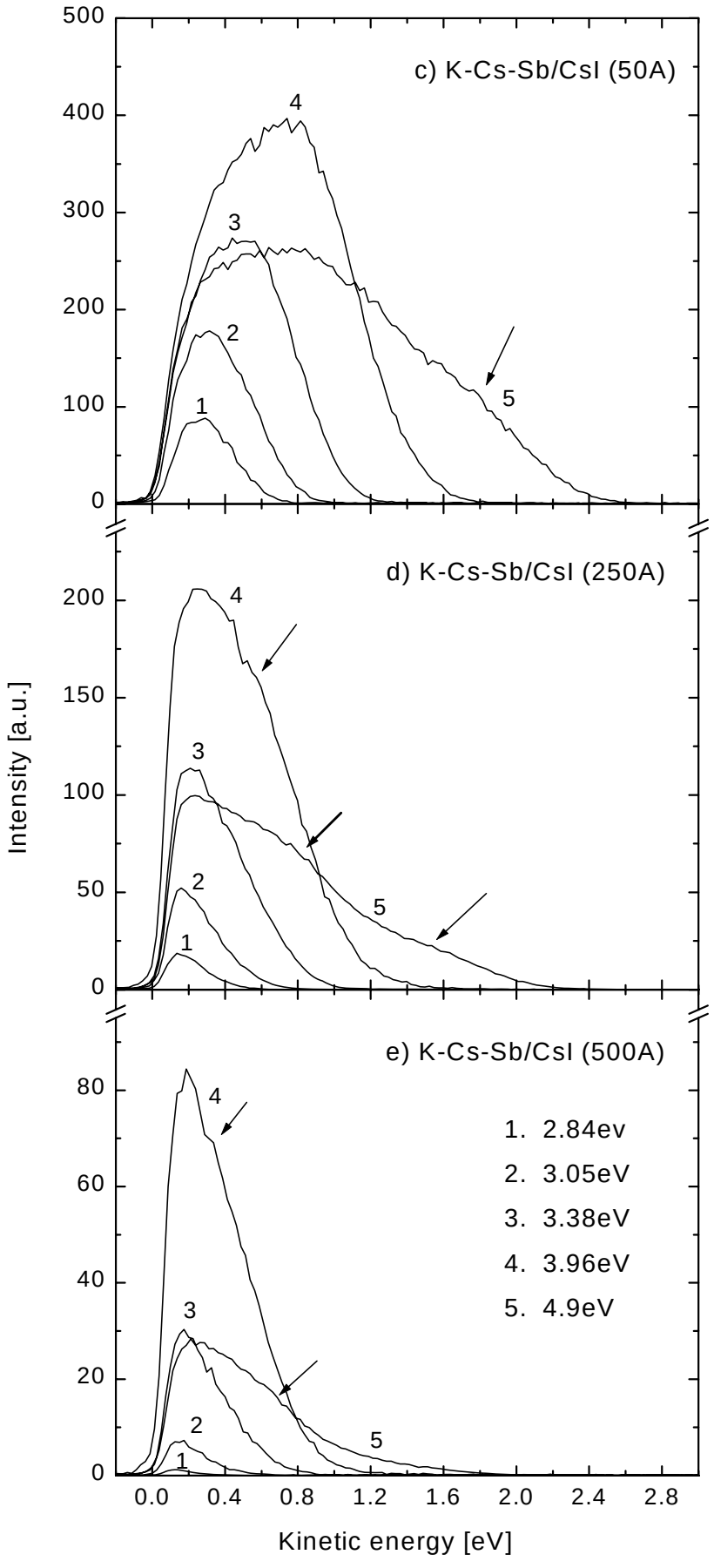
c) K-Cs-Sb/CsI (50A)
d) K-Cs-Sb/CsI (250A)
e) K-Cs-Sb/CsI (500A)
1. 2.84ev
2. 3.05eV
3. 3.38eV
4. 3.96eV
5. 4.9eV
Intensity [a.u.]
Kinetic energy [eV]

Photon energy [eV]	Maximum energy [eV]	FWHM[eV]	Cutoff energy [eV]	Photoemission threshold [eV]
2.84	0.20±.04	0.39±.08	0.90±.04	1.95
3.05	0.22±.04	0.49±.08	1.10±.04	1.95
3.38	0.30±.04	0.67±.08	1.40±.05	1.98
3.96	0.46±.04	0.99±.08	2.00±.04	1.96
4.9	0.32±.04	1.30±.08	2.9±.2	2.0

Table 2.5: PES data of K-Cs-Sb photocathodes coated by 50Å thick CsBr films.

Photon energy [eV]	Maximum energy [eV]	FWHM [eV]	Cutoff energy [eV]	Photoemission threshold [eV]
2.84	0.17±.04	0.26±.08	1.15±.05	1.7
3.05	0.18±.04	0.31±.08	1.15±.05	1.9
3.38	0.19±.04	0.35±.08	1.40±.05	2.0
3.96	0.22±.04	0.40±.08	1.80±.05	2.15
4.9	0.23±.04	0.49±.08	2.75±.05	2.15

Table 2.6: PES data of K-Cs-Sb photocathodes coated by 350Å thick CsBr films.

Photon energy [eV]	Maximum energy [eV]	FWHM [eV]	Cutoff energy [eV]	Photoemission threshold [eV]
2.84	0.25±.04	0.34±.08	0.8±.05	2.04
3.05	0.28±.04	0.49±.08	1.0±.05	2.05
3.38	0.45±.05	0.70±.08	1.3±.05	2.08
3.96	0.75±.05	1.00±.08	1.9±.05	2.06
4.9	0.7±.1	1.55±.08	2.80±.05	2.10

Table 2.7: PES data of K-Cs-Sb photocathodes coated by 50Å thick CsI film.

Photon energy [eV]	Maximum energy [eV]	FWHM [eV]	Cutoff energy [eV]	Photoemission threshold [eV]
2.84	0.14±.04	0.24±.08	0.68±.05	2.16
3.05	0.16±.04	0.30±.08	0.85±.05	2.2
3.38	0.18±.04	0.46±.08	1.10±.05	2.28
3.96	0.25±.04	0.71±.08	1.70±.05	2.26
4.9	0.24±.04	0.93±.08	2.50±.05	2.4

Table 2.8: PES data of K-Cs-Sb photocathodes coated by 250Å thick CsI film.

Photon energy [eV]	Maximum energy [eV]	FWHM [eV]	Cutoff energy [eV]	Photoemission threshold [eV]
2.84	0.13±.04	0.18±.08	0.68±.05	2.16
3.05	0.15±.04	0.24±.08	0.75±.05	2.30
3.38	0.18±.04	0.34±.08	0.92±.05	2.46
3.96	0.19±.04	0.44±.08	1.26±.05	2.70
4.9	0.20±.04	0.65±.08	2.17±.05	2.75

Table 2.9: PES data of K-Cs-Sb photocathodes coated by 500Å thick CsI film.

We simulated the photoelectron energy distribution using our model. For this purpose we used as an input, for each photon energy, the energy distribution measured for the 50Å coatings corrected for the energy loss due to the electron affinity (eq. 2.6). This has the advantage that it already includes the effects due to transport through the interface, which we cannot treat rigorously. The number of simulated events was 10^6 resulting in a negligible statistical uncertainty of a few tenths of a percent for the peak position and the FWHM of a calculated electron energy distribution.

The effect of varying the electron affinity on the electron energy distribution was investigated. Figure 2.30 shows the energy distribution induced by 3.38eV photons, from a K-Cs-Sb photocathode coated with 50nm CsI film. As the input energy distribution was modified due to the variation in the electron affinity (equation 2.5), the calculated energy distribution was influenced as well. One can see that a 0.1eV shift in the electron affinity shifts the peak position by 0.1eV.

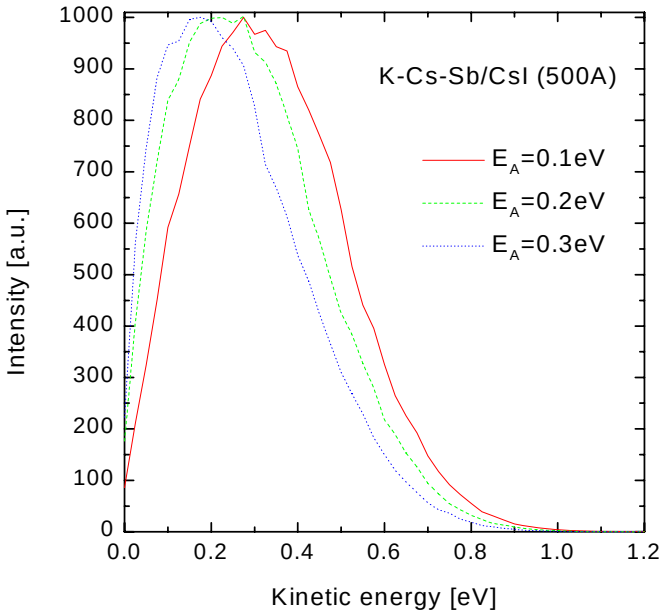

Fig. 2.30: *Normalized photoelectron energy distributions from K-Cs-Sb photocathode coated with 500Å thick CsI film induced by 3.38eV photons calculated for different electron affinity values.*

Varying the value of V_0 (see figure 2.10) between –1.5eV and 1.5eV resulted in no fluctuation in the peak position or the FWHM of the electron energy distribution.

We simulated the photoelectron energy distributions for 350Å CsBr coating and for 250Å and 500Å thick CsI coatings. The input, calculated and measured distributions for CsBr and for 250Å thick CsI coatings, induced by 3.96eV photons are shown in figure 2.31. There is a good agreement between the measured and simulated distributions, indicating the validity of our model.

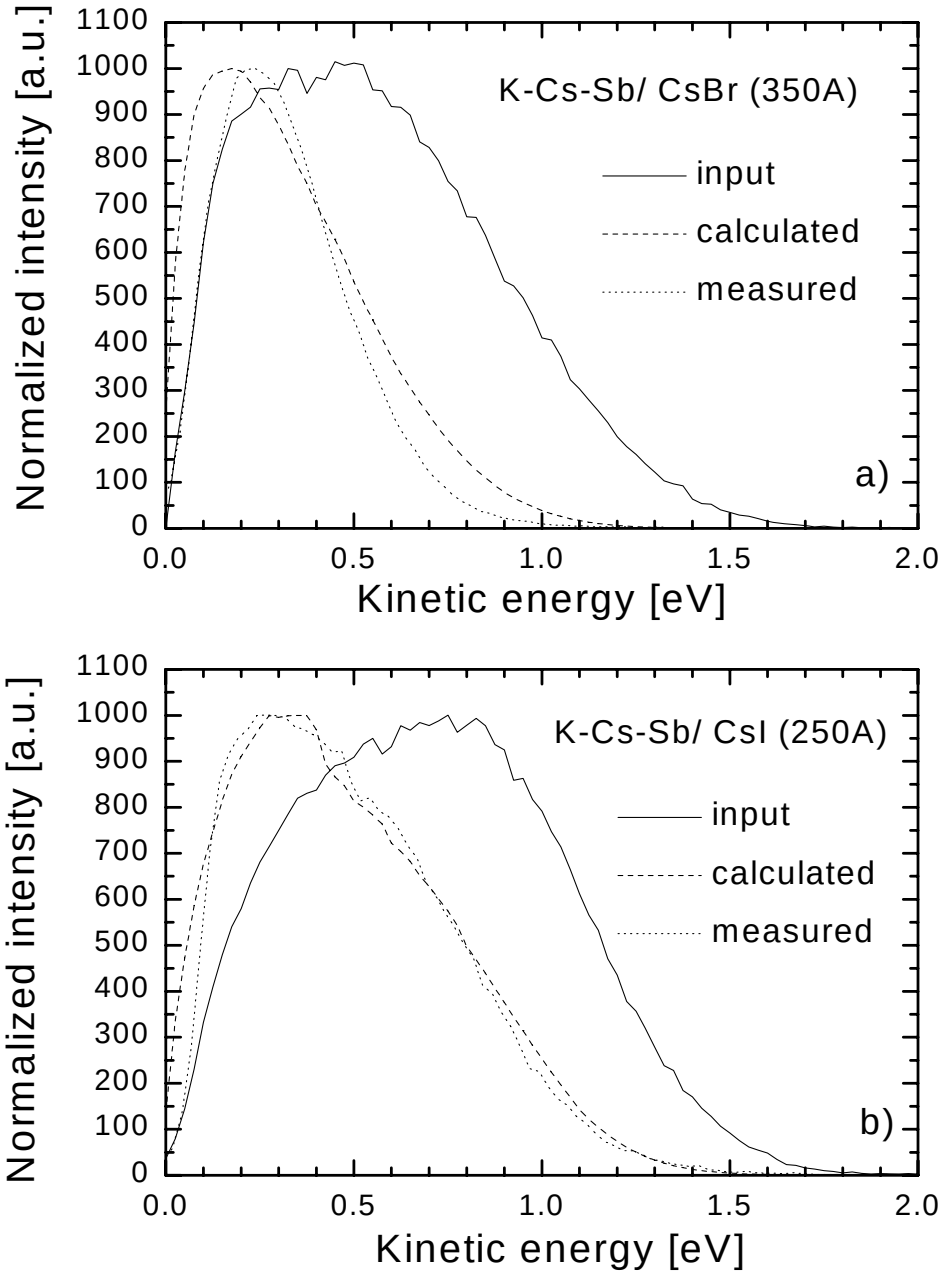

Fig. 2.31: *Simulation and experimental normalized photoelectron energy distribution from K-Cs-Sb photocathode coated with a) 350Å thick CsBr and b) 250Å thick CsI films, induced by 3.96eV photons. The input energy distributions are shown as well.*

Figures 2.32 - 2.34 show the peak position and the FWHM values of the calculated and measured electron distributions from CsI- and CsBr-coated K-Cs-Sb photocathodes. The simulated distributions for different energies show that the peak energy and the FWHM values increase with the photon energy, in agreement with the experimental results. The calculated FWHM is in good agreement with the experimental data and the peak energy is at lower energy for CsBr coatings and at higher energies for CsI coatings compared to our experimental data.

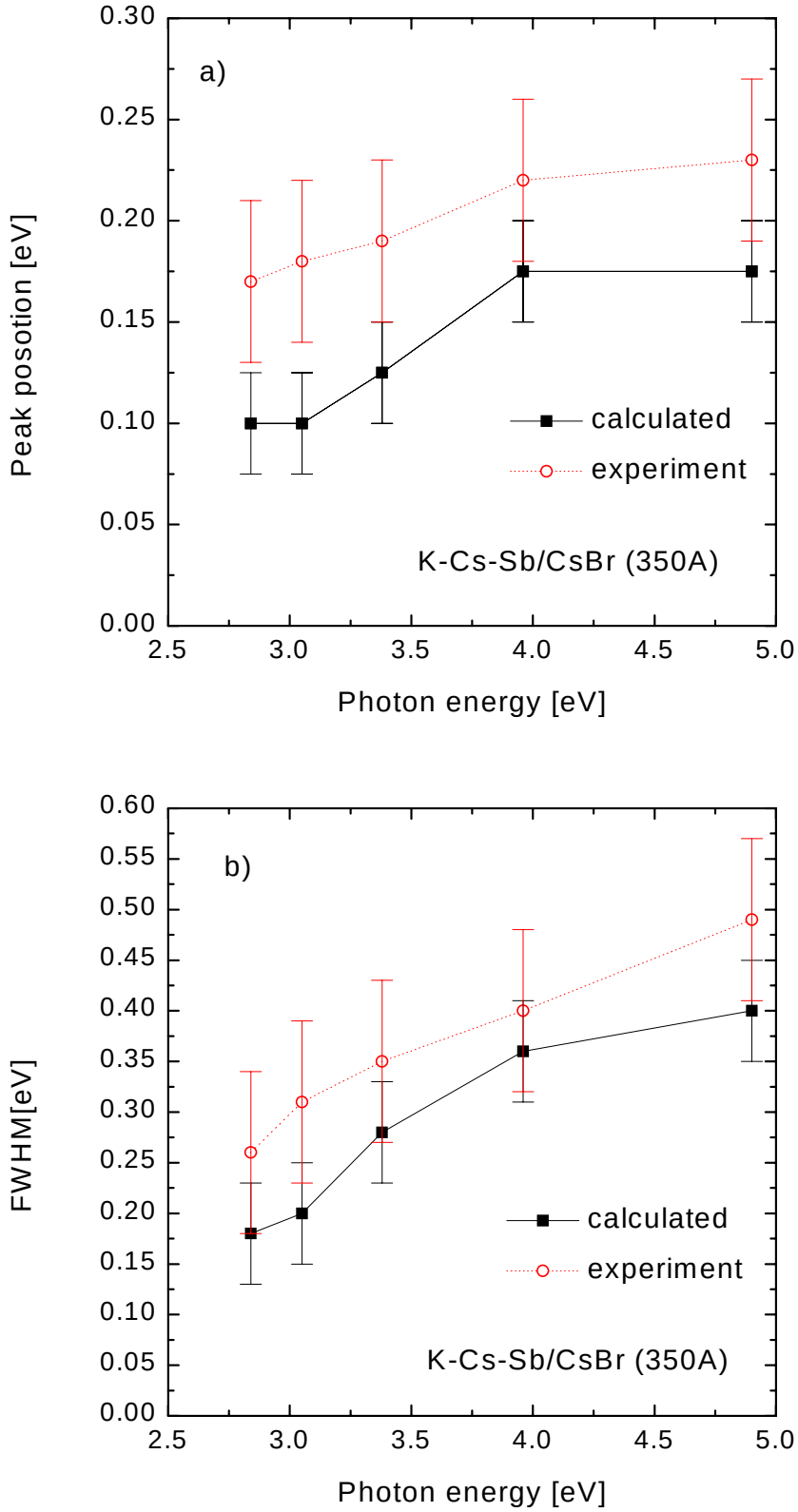

Fig. 2.32: *Calculated and experimental data of a) the peak position and b) the FWHM value of photoelectron energy distributions from a K-Cs-Sb photocathode coated with 350Å thick CsBr film, as a function of the photon energy.*

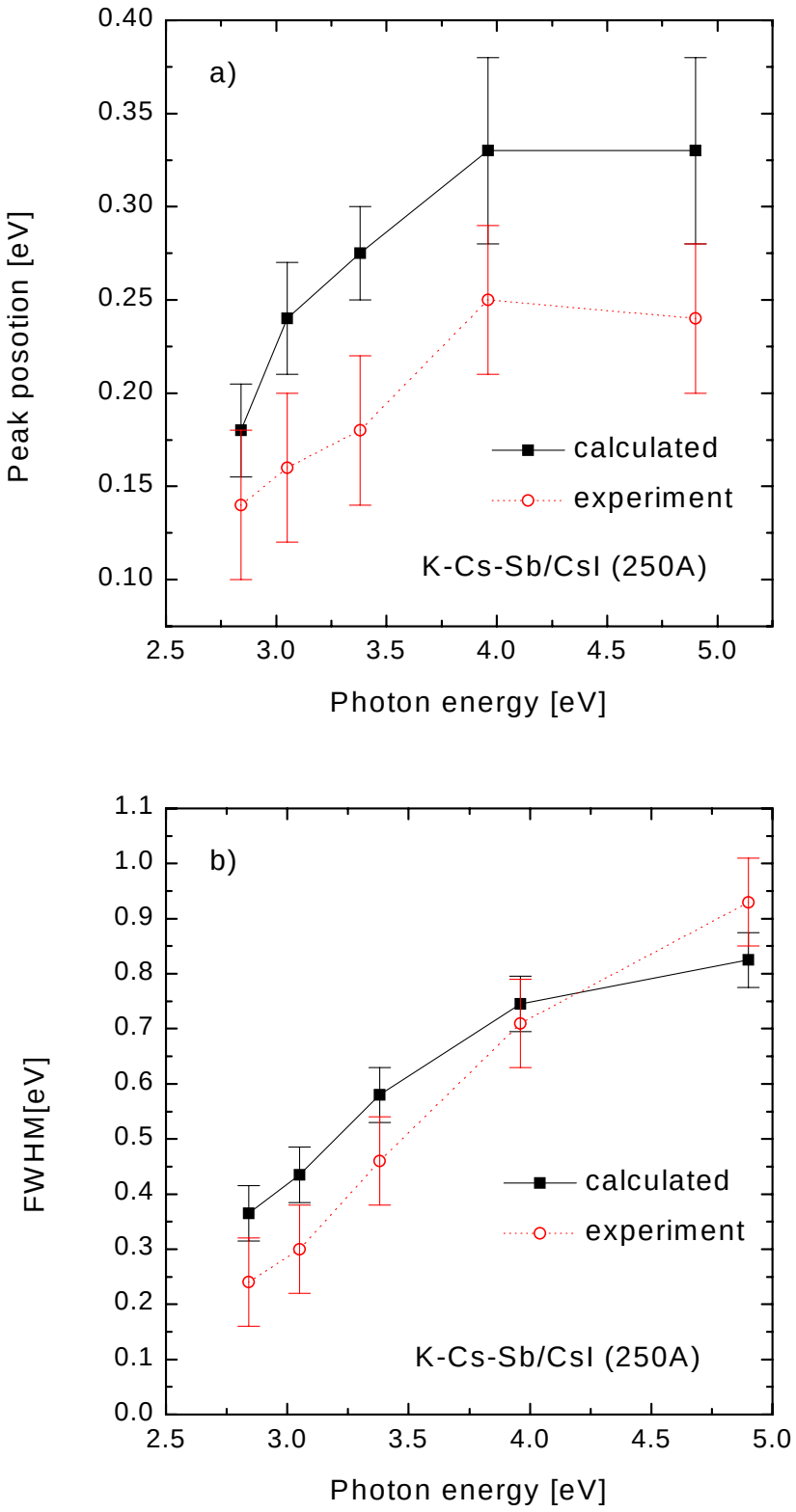

Fig. 2.33: *Calculated and experimental data of a) the peak position and b) the FWHM value of photoelectron energy distributions from K-Cs-Sb photocathodes coated with 250Å thick CsI films, as a function of the photon energy.*

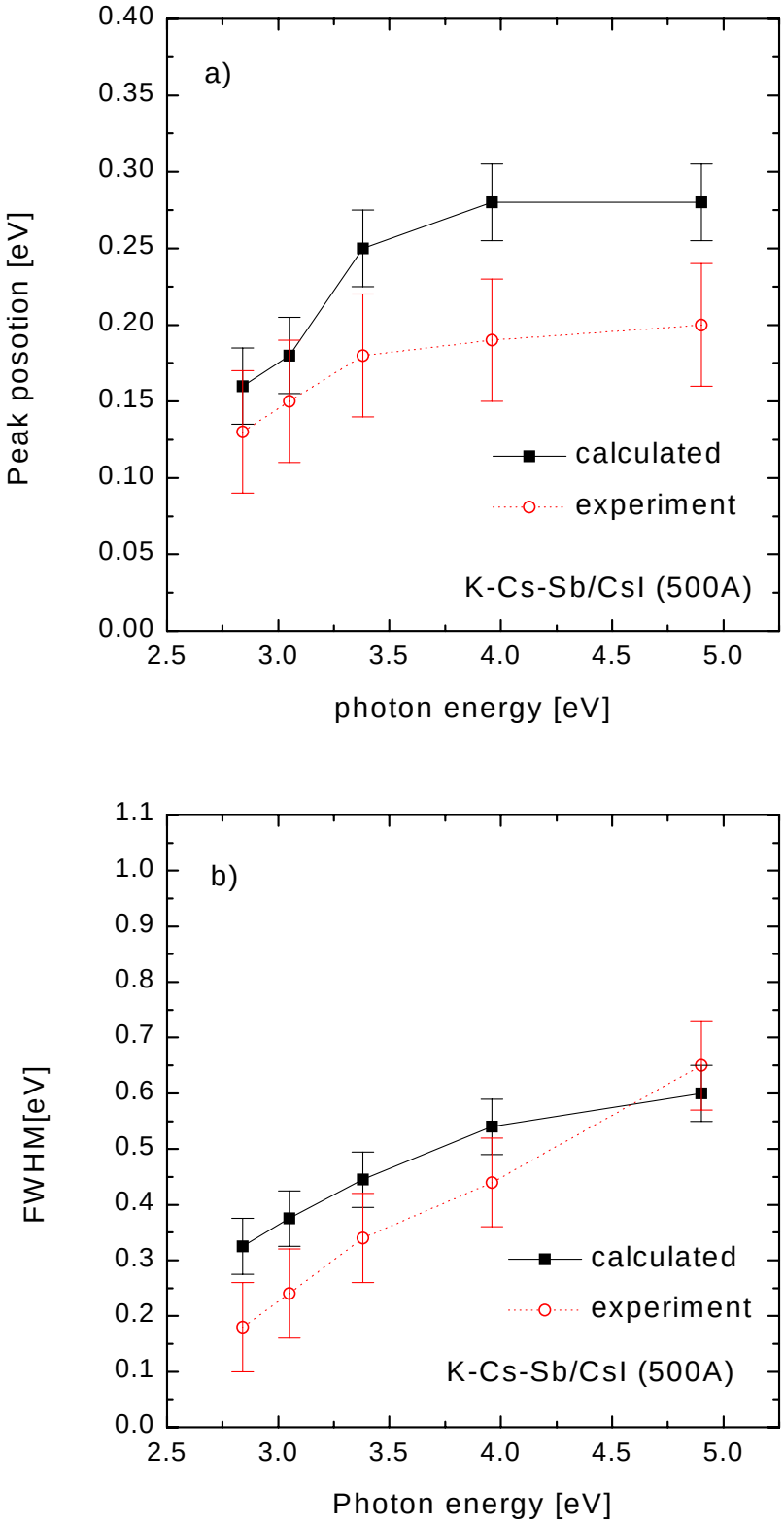

Fig. 2.34: *Calculated and experimental data of a) the peak position and b) the FWHM value of photoelectron energy distributions from K-Cs-Sb photocathodes coated with 500Å thick CsI films, as a function of the photon energy.*

The discrepancy between experimental and calculated results may originate from an inaccuracy in the photoelectron-input distribution. The measured photoelectron energy distribution for 50Å thick coating, which is the simulation-input distribution, does not represent correctly the photoelectron energy distribution after 50Å in thicker films because both its roughness and its surface states effects are enhanced. The surface states influence on the photoelectron transport through 50Å thick coatings is much stronger than on thicker films. This is due to the greater order in the thicker films. Their effect is of lowering the peak energy. The film thickness is not uniform and at 50Å and was shown to have discontinuities. Since the photoelectron attenuation depends exponentially on the film thickness its thinner parts dictate the effective thickness of the film. Therefore the roughness widens the photoelectron energy distribution and increases the peak energy. This effect is negligible for thicker coating films. It is speculated that for CsI, for which the XPS measurement of 50Å thick coating showed a clear trace of the underlying photocathode, the input distribution is wider and its peak energy is higher than the true one, giving rise to the same distortion in the output distribution. For CsBr, having a better coverage of the surface by a 50Å thick film, the effect of the surface roughness is smaller and it might be affected more strongly by surface states, resulting in lowering of the input distribution peak energy.

Another possible reason for the discrepancy is that photons in this energy range give rise to photoelectrons of a few tenths of eV. In this low electron energy range the validity of the electron transport model is questionable, as already discussed in [48,76,77].

Since there is a certain inaccuracy in the coating film thickness, we investigated the dependence of the electron energy distribution on the coating film thickness. We estimated the error of our thickness measurement to be ±5%. For the CsBr coating film, a variation of ±5% in the coating film did not affect the calculated distribution peak position while the calculated FWHM decreases by approximately 5% for thicker films.

2.3.2.5 Stability in gaseous environment

CsBr, CsI and NaI coatings result in a dramatic increase of the alkali-antimonide photocathode stability under exposure to oxygen. Figure 2.35 shows the evolution of the absolute QE of bare and coated Cs-Sb and K-Cs-Sb photocathodes as a function of the residual oxygen pressure inside the chamber. Each data point represents an exposure of a photocathode, for 5 minutes, to oxygen at a known pressure, followed by quantum efficiency measurement at 312nm, in vacuum. The bare photocathodes totally degrade after a 5 minutes exposure to 10^{-5}Torr of oxygen; while the CsI- and CsBr- coated K-Cs-Sb photocathodes remain stable even when exposed to 150Torr, corresponding to the partial pressure of oxygen in air. CsBr-coated Cs-Sb and NaI-coated K-Cs-Sb photocathodes display similar stability in oxygen but a lower QE, and CsI- and NaI-coated Cs-Sb photocathodes have lower QE and poorer stability. The QE of CsI-coated K-Cs-Sb photocathodes remains practically unchanged even after a 1.5 hours exposure to 150Torr of oxygen, as shown in fig. 2.36.

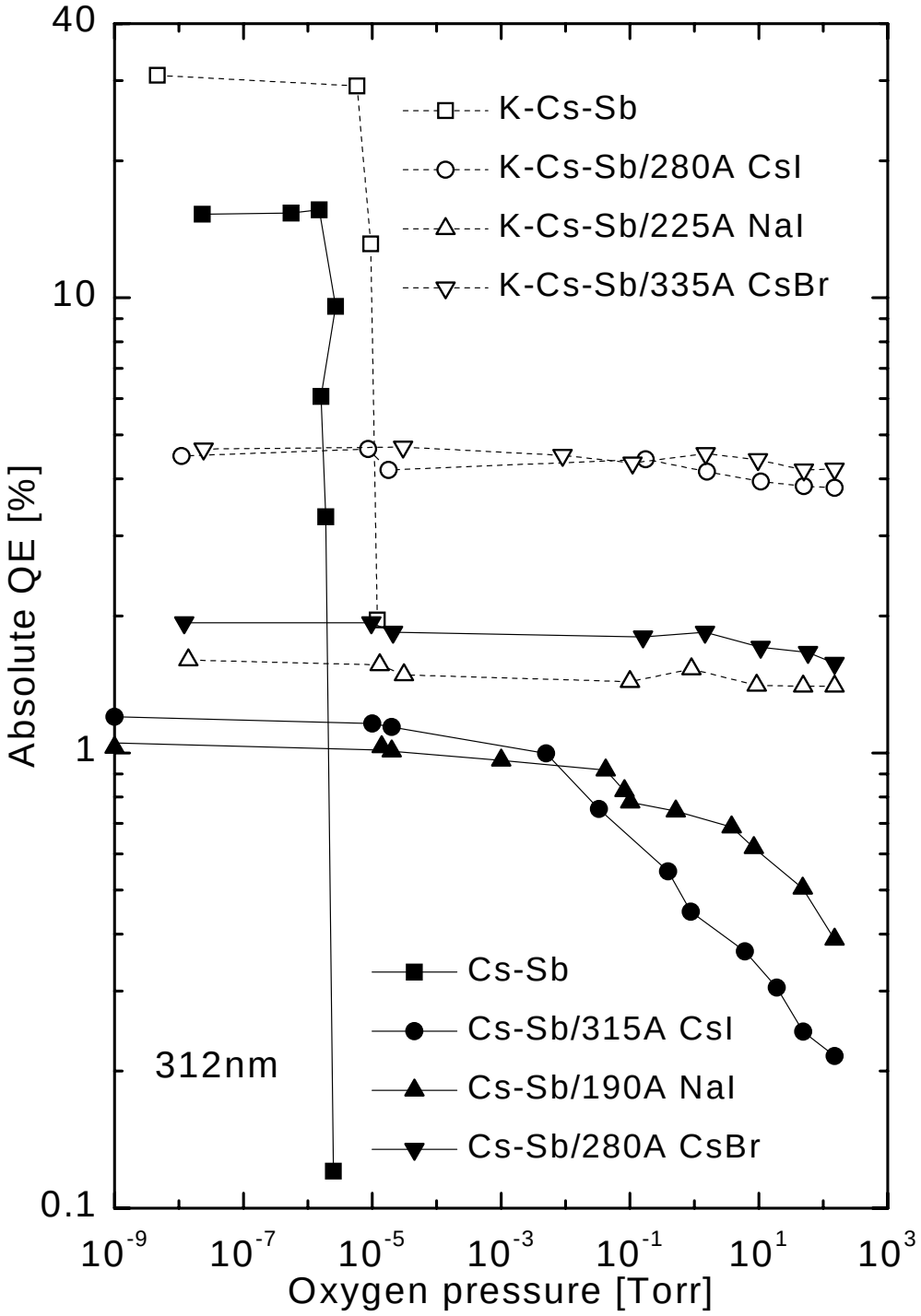

Fig. 2.35: *The result of alkali-antimonide photocathode exposure to O_2. Shown is the absolute QE measured at 312nm of reflective K-Cs-Sb photocathodes: bare and coated with 335Å thick CsBr, 225Å thick NaI and 280Å thick CsI films and of Cs-Sb photocathodes: bare and coated with 280Å thick CsI, 190Å thick NaI and 315Å thick CsBr films, as a function of the residual oxygen pressure. Exposure time at each data point is 5 minutes, followed by a QE measurement in vacuum.*

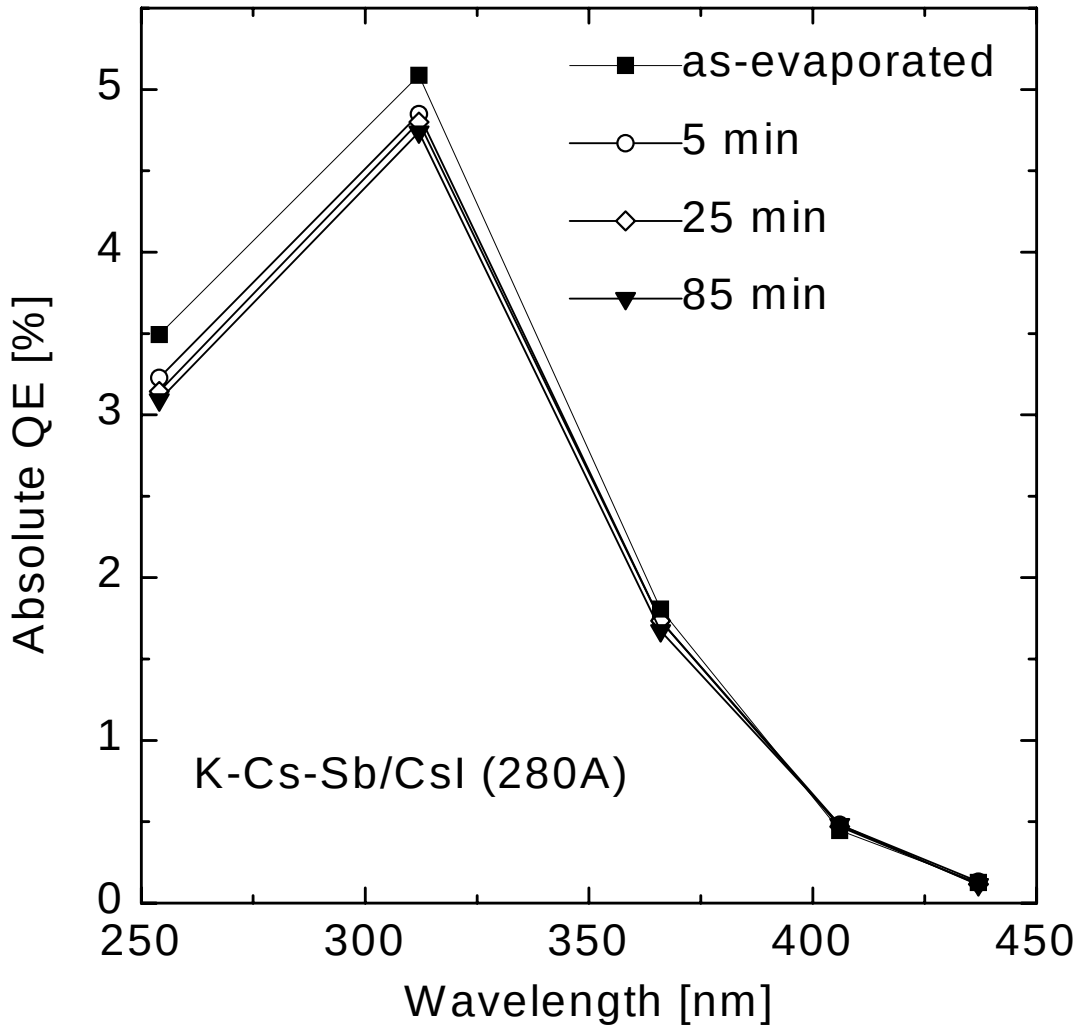

Fig. 2.36: *Evolution of the QE of a K-Cs-Sb photocathode coated with 280Å thick CsI film, subjected to an exposure to 150 Torr of oxygen. Shown are the absolute QE spectra before exposure and after different integral exposure times: 5 min, 25 min and 85 min*

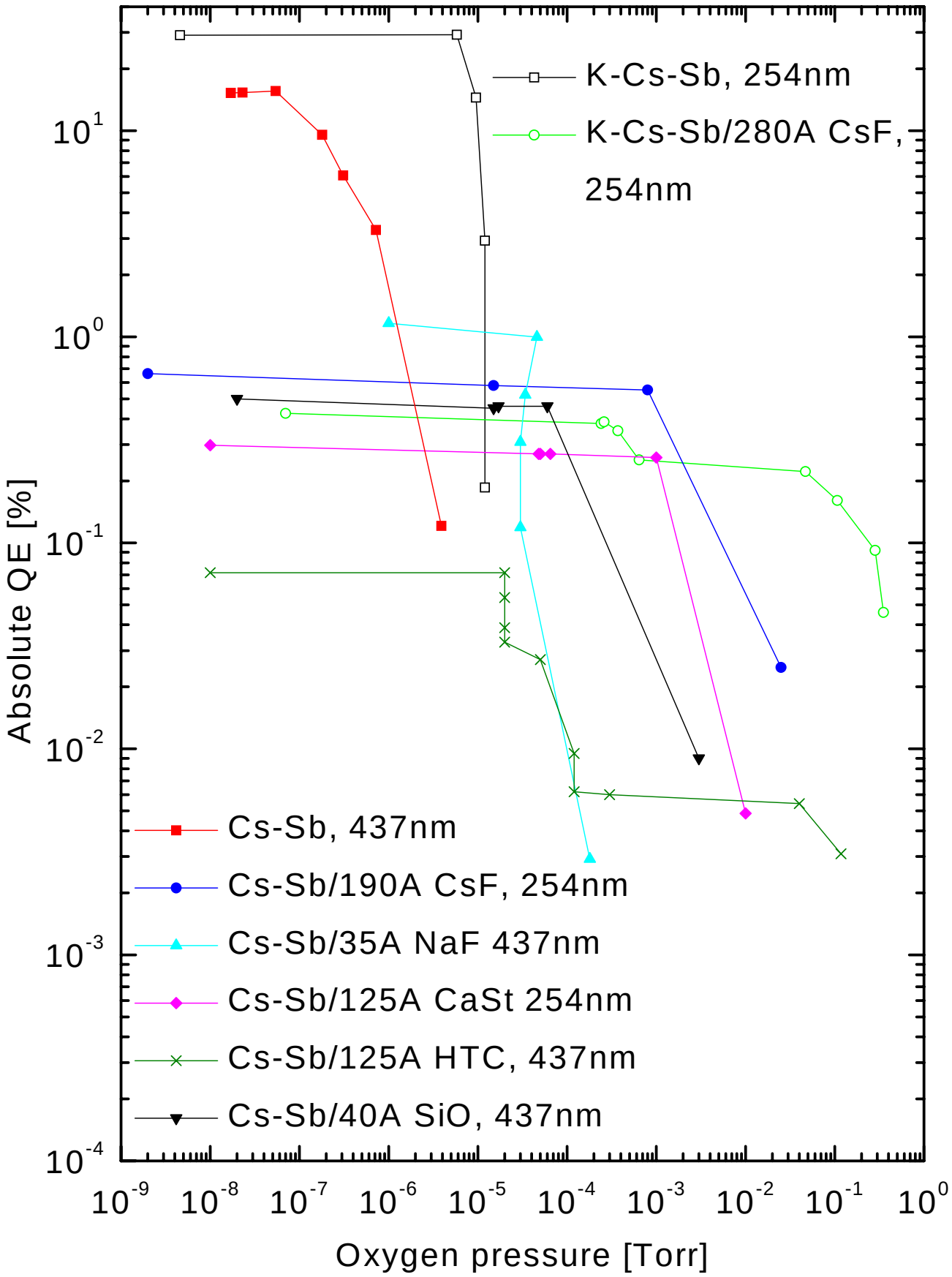

Fig. 2.37: *The results of photocathode exposure to O_2. Shown is the absolute QE measured at 254nm and 437nm of reflective K-Cs-Sb photocathodes: bare and coated with 280Å thick CsF and of Cs-Sb photocathodes: bare and coated with 190Å thick CsF, 125Å thick HTC, 125Å thick CaSt and 35Å thick NaF films, as a function of the residual oxygen pressure. Exposure time at each data point is 5 minutes, followed by a QE measurement in vacuum.*

For the rest of the coating films, the photocathodes displayed smaller stability in oxygen. Figure 2.37 shows the evolution of the absolute QE of Cs-Sb coated with CsF, NaF, HTC, CaSt and SiO. CsF coated K-Cs-Sb and the bare photocathodes are shown as well. Most of these coated photocathodes lost their sensitivity when exposed to oxygen pressures smaller than 0.1Torr. The reasons for the protection capability of some materials and the lack of it in others are not clear. For some coatings, such as NaF and SiO, the film may be too thin to form a continuos layer. One should note that with the exception of CsF, the coating films resulting in a successful protection are thicker than those that did not protect. In general, an improved stability could be obtained by depositing thicker films of all materials, but the QE values would be too low for any practical application.

The coating film thickness is a compromise between the need for efficient electron transmission (high quantum efficiency), and the need for high stability when exposed to gas impurities. Figure 2.38 shows the results of exposing bare and CsI-coated K-Cs-Sb photocathodes to oxygen. The bare photocathode, with an initial quantum efficiency of 30%, cannot withstand an exposure to even 10^{-5}Torr of oxygen. Coating the photocathode with a 225Å thick CsI film results in a quantum efficiency of 10% and stability for up to 0.1Torr of oxygen. A 280Å thick CsI film coating results in a 4-5% quantum efficiency and a stability at 150Torr of oxygen up to an hour and a half. The optimal film thickness therefore depends on the specific application for which the photocathode is required, on the gas purity (usually a ppm level) and on the foreseen post-evaporation handling.

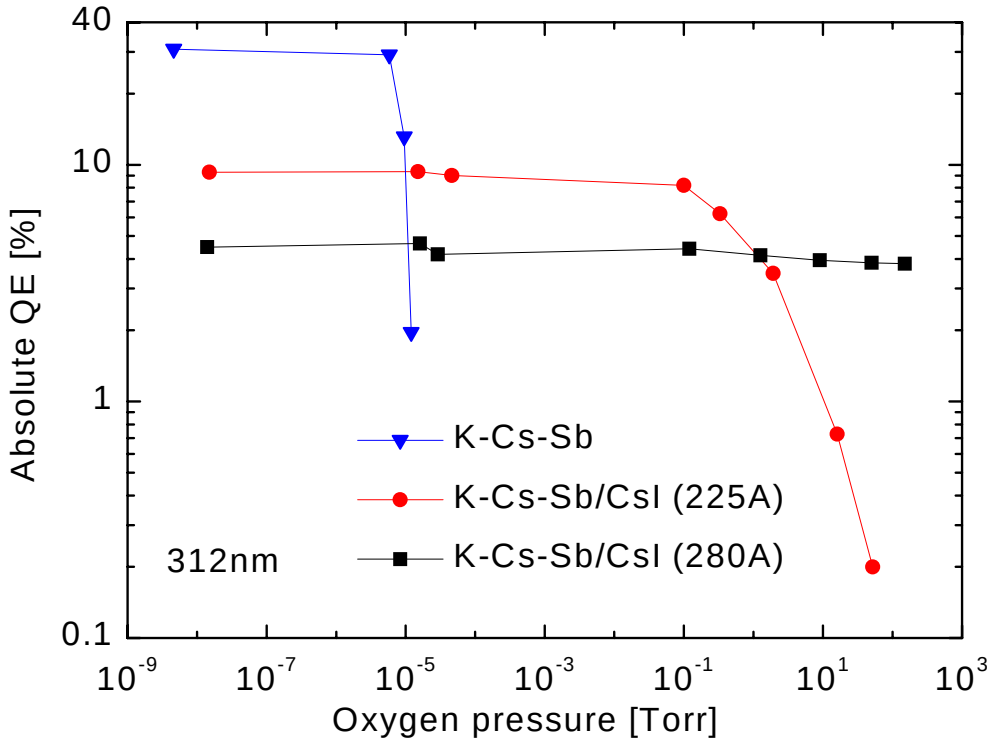

Fig. 2.38: *The evolution of the absolute quantum efficiency of K-Cs-Sb photocathodes exposed to oxygen. Shown are the results of bare and coated photocathodes with 225Å and 280Å thick CsI films, as a function of the residual oxygen pressure. Each data point represents 5 minutes of exposure to oxygen followed by quantum efficiency measurement in vacuum.*

It is known that alkali-halide and alkali-antimonide films are particularly sensitive to moisture. The results of exposing K-Cs-Sb photocathodes, coated with 335Å thick CsBr and 280Å thick CsI films, to water vapor are shown in figure 2.39. Each data point represents 5 minutes of exposure to water vapor at a given pressure, followed by quantum efficiency measurement in vacuum. The water vapor pressure was measured using a residual gas analyzer for low pressures, and a hygrometer for higher pressures. Both coated photocathodes are completely degraded when exposed to 10^{-5}-10^{-4} Torr of water vapor. The difference between the two is within the experimental error and thus insignificant. A possible explanation for this degradation is the hygroscopic nature of CsBr and CsI. This is supported by the results of a recent extensive SEM study of the surface morphology of alkali-halide films [64]. It shows that uniformly evaporated CsBr and CsI films, a few tens of nm thick, form clusters after being exposed to a humid environment. Such cluster forming of the coating film exposes the underlying K-Cs-Sb photocathode to moisture, resulting in its degradation

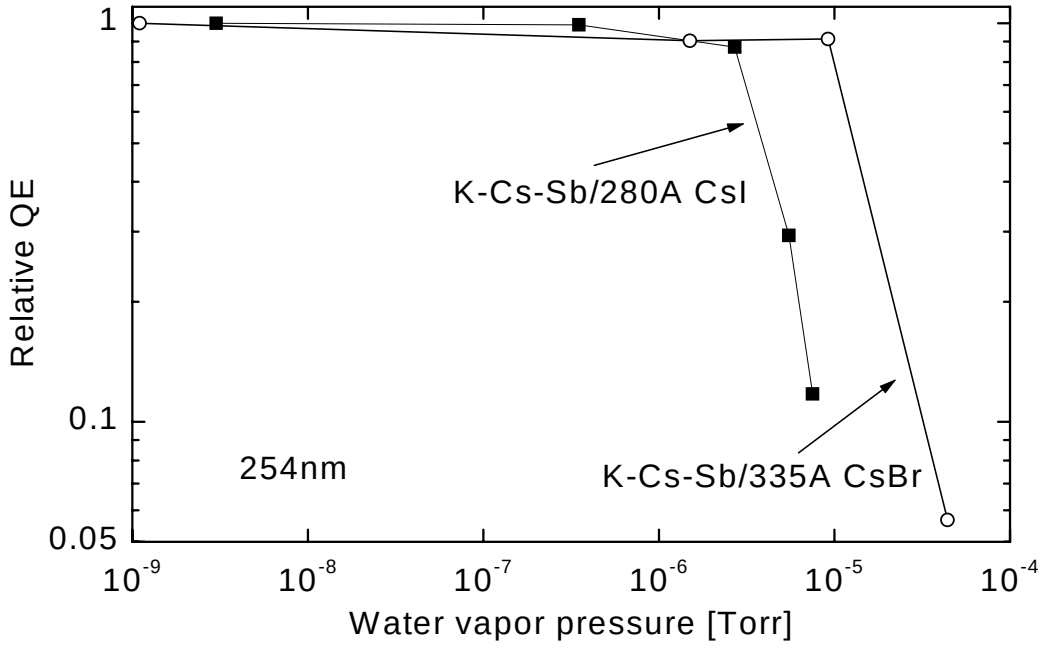

Fig. 2.39: *The evolution of the relative quantum efficiency of coated K-Cs-Sb photocathodes exposed to water vapor. Shown are the results of photocathodes coated with 335Å thick CsBr and 280Å thick CsI films, as a function of the residual water vapor pressure. Each data point represents 5 minutes of exposure to water vapor, followed by quantum efficiency measurement in vacuum, at a wavelength of 254nm.*

We also exposed CsBr-coated K-Cs-Sb and NaI-coated Cs-Sb photocathodes to ambient air with water partial pressure of 10 Torr. Fig. 2.40 shows the result of exposing K-Cs-Sb photocathodes coated with 335Å of CsBr to ambient air for 5 minutes, had no effect on the composite photocathode up to 0.1 Torr. However, exposing them to higher pressures resulted in a fast decay in QE, probably due to moisture. Heating the photocathode in vacuum did not restore the QE. A Cs-Sb photocathode coated with 195Å thick NaI film was exposed for 5 minutes to 50Torr of oxygen and for 5 more minutes to 60Torr of air with a partial water pressure of 1.1×10^{-2}Torr. A strong decrease n the QE was observed. However, the photocathode recovered fully after heating in vacuum for a few hours. For some wavelengths one could observe even an enhancement of the QE, the origin of which is not well understood.

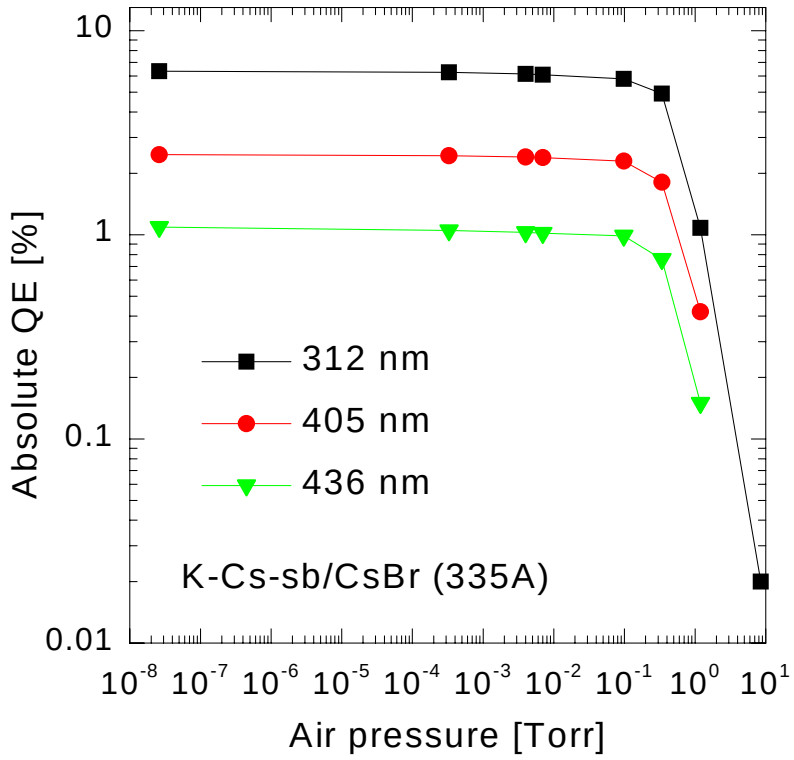

Fig. 2.40: *The evolution of the absolute quantum efficiency of K-Cs-Sb photocathodes coated with 335Å of CsBr, exposed to ambient air with water partial pressure of 10Torr, at different photon wavelengths. Each data point represents 5 minutes of exposure to water vapor, followed by quantum efficiency measurement in vacuum.*

2.3.2.6 Surface charging

The effects of high photon flux on the QE of CsBr-coated K-Cs-Sb photocathodes was investigated. Surface charging was measured in 1atm. of methane at wavelength of 254nm with photon flux between 2×10^9 and 3×10^{10} photons/sec mm^2. A potential of +300V was applied to the anode cylinder, located approximately 5mm away from the photocathode. The results are shown in fig. 2.41. For photon flux of 2×10^9 photons/sec mm^2, practically no charging was observed. For the unrealistically large flux of 3×10^{10} photons/sec mm^2, a decrease of 10% in the photocurrent was measured in the first 5 seconds, followed by a decrease of another 15% over half an hour. The photocurrent recovered within 15 minutes after stopping the illumination. No charging was observed for bare K-Cs-Sb photocathodes, even at the highest photon flux.

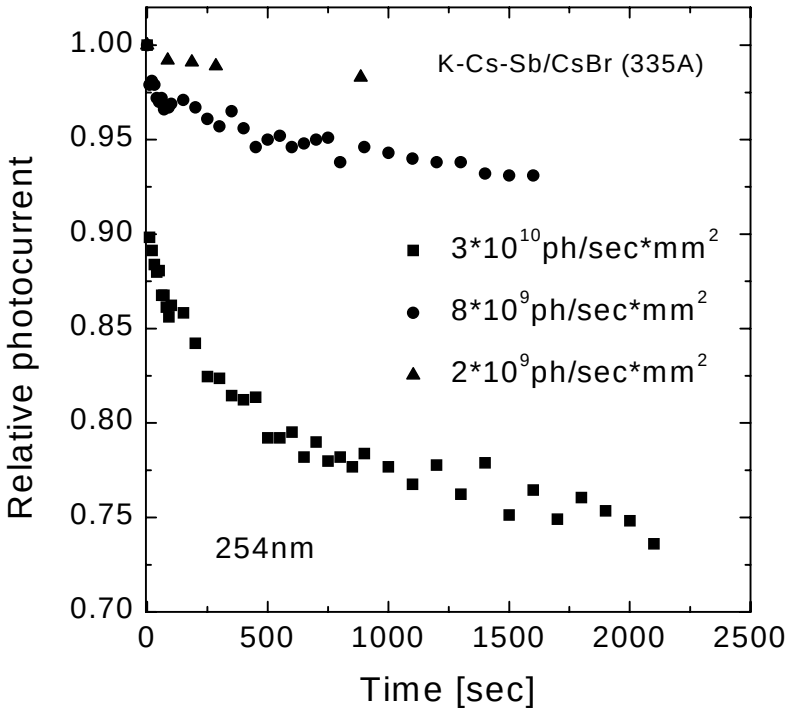

Fig. 2.41: *Charging up of a K-Cs-Sb photocathode coated with 335Å of CsBr. Shown is the relative photocurrent of the photocathode as a function of time for photon flux of 30, 8 and 2 GHz/mm^2.*

2.3.2.7 Photon aging

Aging of the CsBr-coated K-Cs-Sb photocathode by photon impact was measured under similaronditions, at wavelengths between 254 and 633nm at a photon flux of 3×10^{10} photons/sec mm^2. Figure 2.42 shows the aging as a function of the number of accumulated photons per mm^2. A QE decrease by 50% was measured after accumulating 6×10^{15} photons/mm^2. No clear dependence of the aging on the photon flux or wavelength was observed. To evaluate this degradation one could think of a critical application like mammography or radiography requiring very high instantaneous X-ray flux. For instance, with a scintillator coupled to a photocathode and a gaseous multiplier, the QE will decay by 10% after 10^{14} photons/mm^2, equivalent to about 10^5 radiographic images. It is interesting to note that the QE of the bare photocathode remained unchanged after accumulating 3×10^{15} photons/mm^2. Photon aging of thick and thin CsBr photocathodes was investigated in a separate setup. A 300Å thick CsBr, aged in the same conditions showed no degradation up to 10^{14}ph/mm^2 [62]. The mechanism responsible for the aging process in alkali-halides, discussed in the past by many authors [2,62,105] is being investigated. It may be related to photolysis of CsBr or to ion displacement in the coating layer due to electron accumulation in the interface between the photocathode and the coating film and in the coating film.

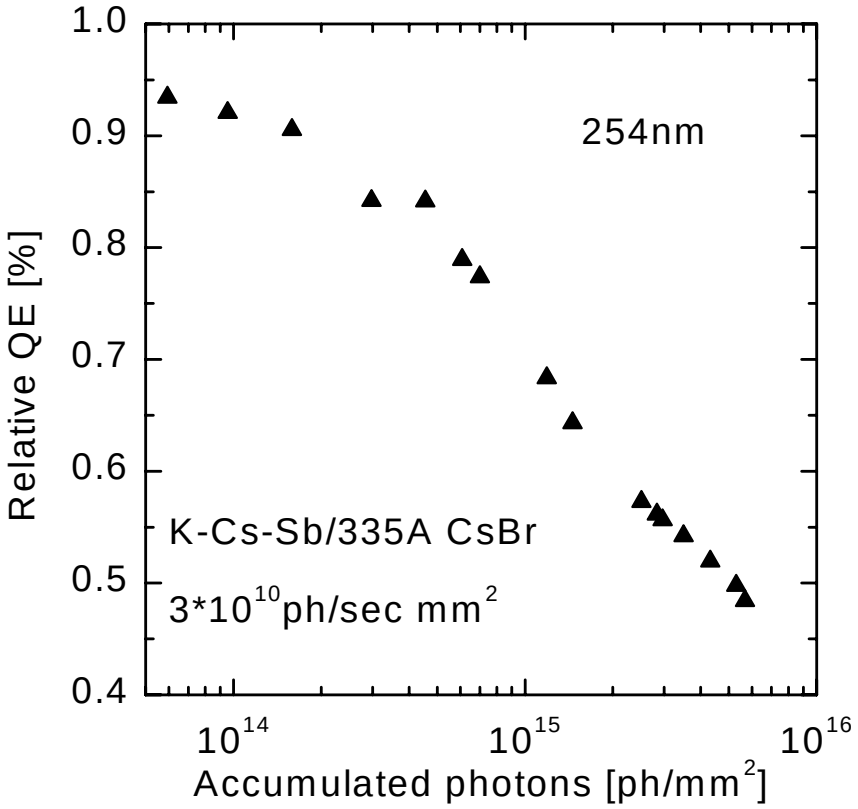

Fig. 2.42: *Aging by photons in a current collection mode (with no gain) at 254nm, under photon flux of 3×10^{10} photons/sec mm^2 in 1 atm. CH_4, of a K-Cs-Sb photocathode coated by a 335Å thick CsBr film, as a function of the total number of accumulated photons per mm^2.*

2.3.2.8 Gas multiplication.

The stability of operation of our composite photocathodes was investigated under gas multiplication. The study was done in a parallel-plate multiplying geometry, in which all ions hit the photocathode, in 1atm. of high purity methane. A positive voltage was applied to a mesh electrode placed 1 mm away from the photocathode surface; the photocurrent was recorded from the photocathode. Figure 2.43 shows a gas multiplication curve measured in a parallel-plate mode, using a semitransparent K-Cs-Sb photocathode coated with a 335Å thick CsBr film. Stable gains of 10^4 and more were measured at 1 atm of methane for both CsBr- and CsI-coated K-Cs-Sb photocathodes. The exponential behavior of the gain with the applied potential indicates the absence of secondary effects.

Aging of photocathodes by back drifting avalanche ions could be one of the major problems when coupling a photocathode to a gaseous electron multiplier. Therefore, a detailed study of the long-term performance of the photocathodes under gas multiplication should be performed. In the frame of this work only very preliminary results could be obtained due to some technical difficulties. The measurements showed that the aging of a photocathode coated by 280Å CsI thick film is comparable to the known aging of CsI photocathodes [2,62]. Ways of reducing and preventing ion aging and secondary photon effects in gas avalanche photomultipliers will be discussed in chapter 4.

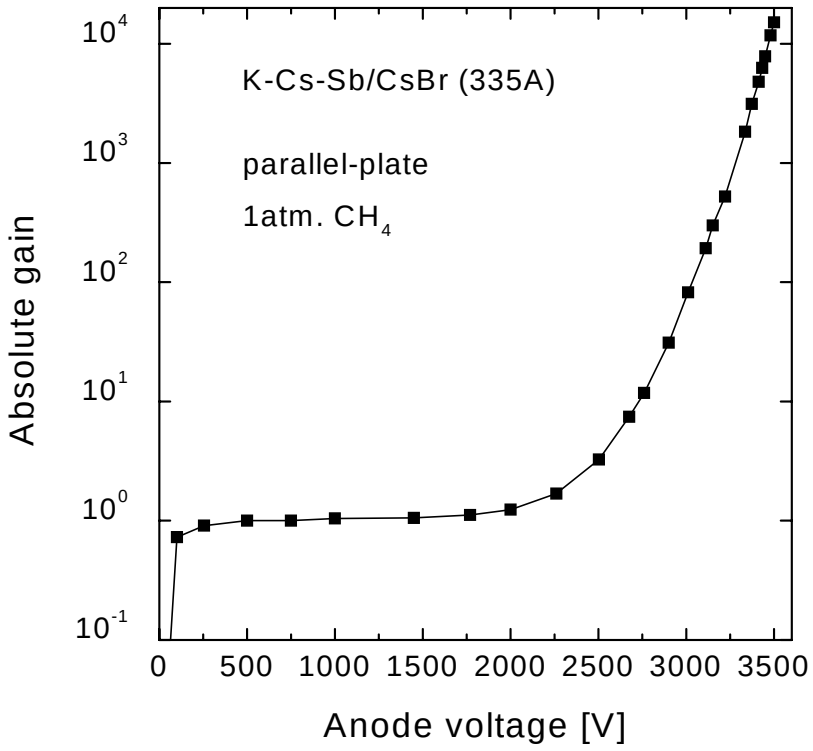

Fig. 2.43: *Absolute gain as a function of anode voltage of a 1 mm gap parallel plate gas electron multiplier. The multiplier is at 1 atm of methane, coupled to a semitransparent K-Cs-Sb photocathode coated with 335Å thick CsBr film.*

2.3.3 Photocathodes with removable coating

We investigated a method, suggested by Sommer [106], for protecting alkali-antimonide photocathodes, with removable coatings. The idea consists of coating the photocathode, after production, with a protective film. The purpose is for transfer, installation in a detector or in another instrument, or storage in gas or poor vacuum. The film can be later removed by moderate heating in vacuum rendering the photocathode ready for use.

The coating material should be chemically inert with respect to the photocathode substance and compatible with ultra high vacuum at room temperature. It should also evaporate at a temperature below 130^0-150^0C, which is the limit of thermal stability of most alkali-antimonide photocathodes. We used HTC, having a low sublimation point (120^0C), as a removable coating for Cs-Sb photocathodes.

Fig. 2.44 shows experimental data of the QE of a Cs-Sb photocathode under the cycle of coating and removing 1.5μm and 0.8μm thick HTC films. The cycle includes HTC deposition, melting by heating the photocathode to 80^0C followed by cooling to room temperature, exposure to oxygen and removal by heating to 140^0-150^0C. The melting process, performed at a temperature lower than that required for evaporation, modifies some of the film properties, making them more transparent to light and less permeable to gas. The QE of a Cs-Sb photocathode coated with a 0.8μm thick HTC film was reduced approximately by a factor of 2 after exposure to 150 Torr of oxygen for 20 minutes. This may result in a QE of the order of 10% in the 300-350nm spectral range after exposure to oxygen, compared to 5% achieved for permanent coating. However, the problem of contamination of the vacuum chamber during removal of the HTC film remains to be solved.

Thin film (200-650Å) removal did not result in an appreciable degradation of the photocathode emissive properties. However, for thicker films, HTC removal requires thermal treatments lasting over 20 minutes thus degrading the photocathodes. Our results indicate that the optimal thickness of the HTC coating should be kept between 0.15 and 0.8μm, to assure best protection capability. Thinner films do not fully cover the photocathode and thicker films lose their protection capability, presumably due to cracking, induced by internal mechanical stress and large temperature variation [107].

A more detailed discussion of the removable coating method and the experimental results can be found in [86,108].

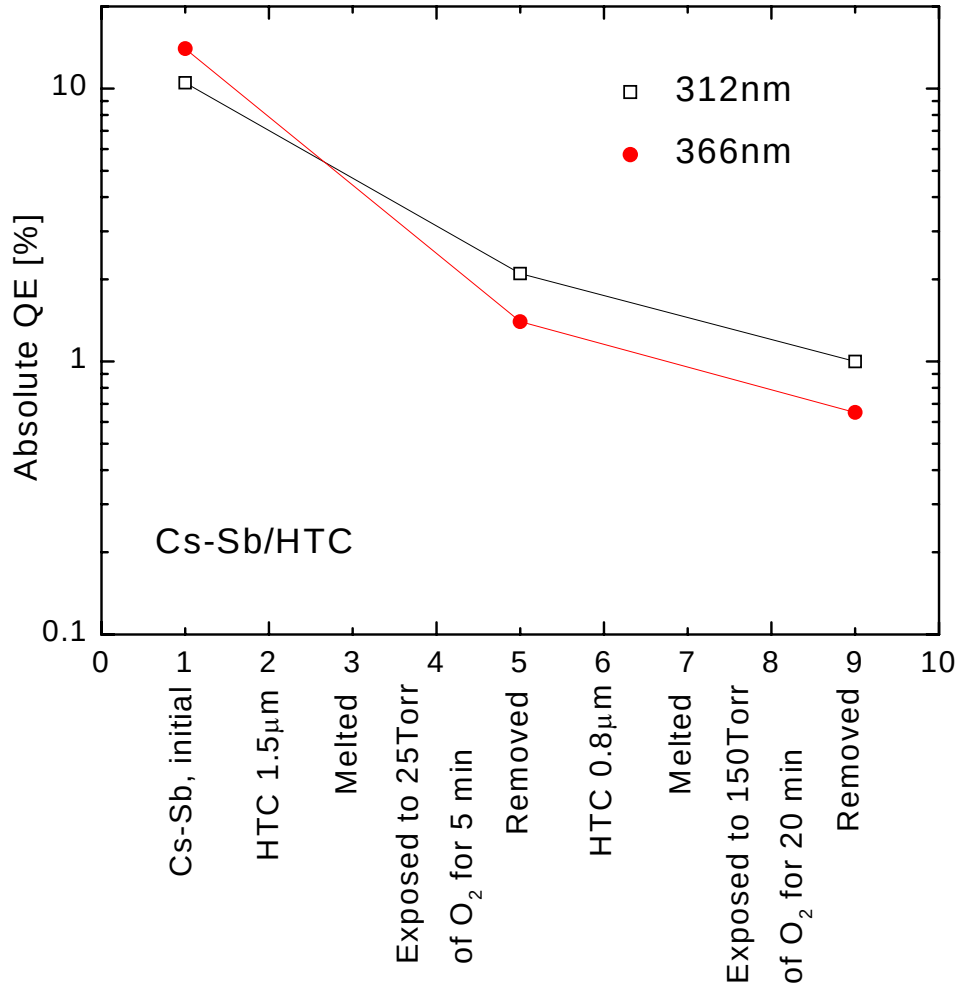

Fig 2.44: *Treatment of a Cs-Sb photocathode with thick HTC films. The QE values at 312 and 365nm measured for a bare photocathode before HTC coating and after its removal are shown. The following treatments were applied: 1) initial Cs-Sb deposition, 2) coating with 1.5μm thick HTC film, 3) HTC melting, 4) exposure to 25Torr of oxygen for 5min, 5) HTC removal, 6) Coating with 0.8μm thick HTC film, 7) HTC melting, 8)exposure to 150Torr of oxygen for 20min, 9)HTC removal*

3. Photocathodes for the UV range.

A related subject of research included in this work was the study of photoconverters in the UV range. The investigations focussed on a search for robust, air-stable photocathodes capable of operation in gas avalanche UV photomultipliers. Materials with wide band gap such as CsI are preferable because they are “solar-blind”. Diamond and CsBr films may fulfill those requirements and the main results are summarized in this chapter.

3.1. Diamonds films

CVD diamonds and diamond like carbon (DLC) films, are radiation hard and robust wide band-gap materials, sensitive in the near-UV range. CVD diamonds prepared by Microwave or Hot Filament Plasma [109], are polycrystalline with sp^3 (diamond like) bonds. DLC films deposited by C ion implantation at very low energies [110] are amorphous and exhibit a mixture of sp^2 (graphite-like) and sp^3 bonds. The DLC surface is rich with defects and is characterized by an sp^2-rich layer, its thickness depends on the growth conditions. We measured the photoemission properties of CVD diamonds and DLC films in order to understand the effect of their preparation parameters and of surface treatments on the energy band structure and to optimize the QE of these materials.

3.1.1 Experimental setup

We conceived two complementary experimental setups, operating in two wavelength ranges: Vacuum UV (140-240nm) and near UV-to-visible (200-700nm), for the study of photoemission from diamond and diamond-like films. The vacuum UV setup consists of a vacuum-operated monochromator (Jobin-Yvon H20 VUV), with a 30W / MgF_2 window deuterium lamp. The near-UV to visible setup is based on an air-operated double monochromator (Oriel 77250) with a 1000W Xe lamp (Oriel 6269). Samples are mounted within a vacuum chamber of 10^{-5}Torr. Photoelectrons induced by the impinging photons in selected wavelengths induce a photocurrent that is recorded and normalized against calibrated standards into an absolute QE. The calibration is verified in the overlapping range of the two systems, 200-240nm. The dark current, permitting the measurement of absolute QE of 10^{-4} and 2×10^{-10} in the first and second setup, respectively limited the sensitivity.

3.1.2 QE spectra.

Figure 3.1 shows typical absolute QE spectra of two CVD diamond photocathodes and of a DLC film (85% sp^3) measured in 140-320nm spectral range. The QE of CVD diamond films is about 20-50 times higher than that of DLC films. This may be related to the difference in the structure of the layers, implying a difference in the energy bands and in the electron transport properties.

The absolute QE values of different DLC films having 10-85% sp^3 bonds, of a CVD diamond and of graphite, in 200-320nm spectral range are shown in figure 3.2. The QE of the 85% sp^3 DLC film is considerably higher than that of all the other DLC samples. However, the small difference between the photoemission of the other DLC films, suggests that the main factor determining their QE may not be the sp^3 fraction but the sp^2-rich surface layer. More details on the photoemission of DLC films, which were abandoned by us as candidates for UV photocathodes can be found in [111].

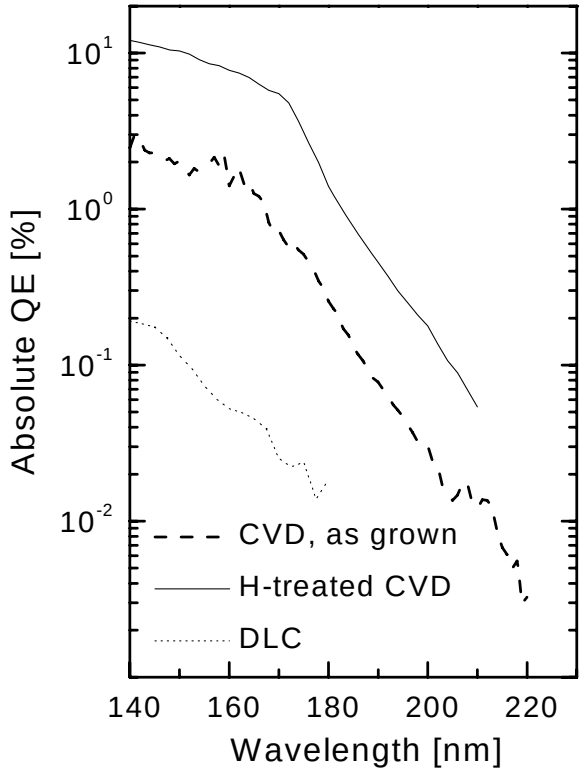

Fig. 3.1: *Typical absolute QE spectra of a CVD diamond: as grown and treated by post-growth H_2 plasma and of a DLC film of 85% sp^3 bonds.*

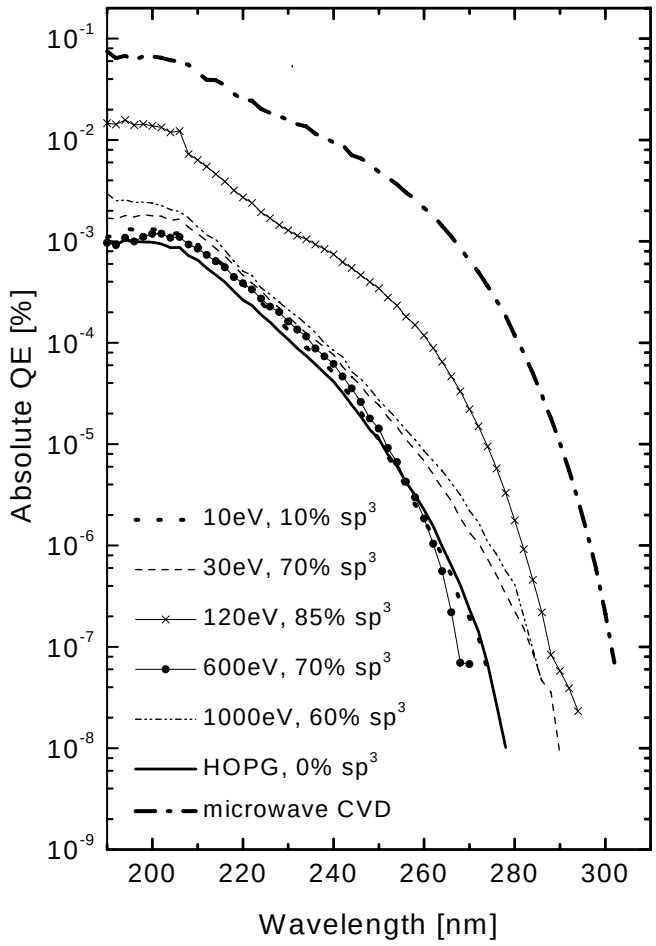

Fig. 3.2: *Absolute QE spectra of DLC films, prepared at different C ions implantation energy, having 10-85% sp^3 bonds, of a CVD diamond film and of graphite, in 200-320nm spectral range.*

3.1.3 Surface termination of CVD diamond films.

Considering the possible dependence of the CVD photoemission of the surface structure, purity and chemical termination, we have studied the effect of different surface treatments, attempting to achieve hydrogen, nitrogen and oxygen termination of CVD diamonds. For this purpose we combined Auger electron spectroscopy (AES) surface analysis with photoemission measurements. The best values of 12% QE at 140nm, were measured after hydrogen plasma and are presented in figure 3.1. This process has two roles: on one hand it is etching the remnants of graphitic material from the sample and on the other hand it is H-terminating the surface. H-termination prevents surface reconstruction of the diamond, providing low resistivity and often negative electron affinity. Although the measured QE is inferior to the QE of other UV photocathodes, e.g. CsI (40% at 150nm [2]), it could be interesting for applications where the efficiency can be scarified in favor of radiation hardness and robustness. Storage of hydrogenated CVD diamonds under ambient conditions for several days resulted in oxygen adsorption with a subsequent two-fold degradation of the photoemission properties. The film reaches though a stable QE value of 6% at 150nm. The original QE values were restored by re-hydrogenation. This work is summarized in [112-115].

3.2 CsBr photocathodes

CsBr is a solar-blind UV photocathode, investigated very little in the past [48,51,75]. Our interest in it was raised by the successful protection of alkali-antimonide photocathodes by their coating with 335Å thick CsBr films. We therefore studied their photoemission properties and their stability in ambient air and under gas multiplication. The results are presented in detail in ref. [62]

3.2.1 Experimental setup

The experimental setup included a high vacuum (10^{-7}Torr) evaporation chamber, coupled to a vacuum-UV (140-240nm) monochromator equipped with a D_2 lamp, described in section 2.1.1. CsBr photocathodes were thermally evaporated, and their thickness was determined using a quartz crystal thickness monitor. After the sample preparation, its absolute QE was measured in situ, in a reflective mode, by the method described for diamond films. Some of the samples were heated, in situ, to 70^0C, with a built-in water heat exchanger.

3.2.2 Chemical composition.

XPS measurement was performed on a 2000Å thick CsBr photocathode. The photocathode was evaporated and transferred to the XPS facility under high vacuum, with no exposure to air, as described in section 2.1.4. The surface was found to contain atomic concentration of 50% Cs, 39% Br, 2.5% O and 8%C. The Cs to Br ratio on the surface is 1.3. A possible explanation to the excess of Cs is the induction of a photolysis effect by the x-rays, breaking the ionic bonds between Cs and Br. Since Br has a low vapor pressure compared to Cs, it evaporates, leaving the surface with an access of Cs. It is also possible that the thermal evaporation of CsBr, breaking the ionic bonds results in the observed stoichiometry. Exposing the photocathode to ambient air outside the vacuum chamber, for 10 minutes, did not change its surface chemical composition.

3.2.3 QE spectra.

The QE spectra of 300Å and 5000Å thick CsBr films are shown in figure 3.3. The photoemission cutoff is approximately at 174nm, and the QE values measured at 150nm were 15% and 21% for the thin and thick photocathodes respectively. Heating the photocathodes to 70^0C resulted in an enhancement in the QE that saturated after 4 and 6 hours for the thin and thick photocathodes respectively. The heat treatment also shifted the red boundary to 190-195nm. The best QE value measured after heat-enhancement reached 35% at 150nm. The heat enhancement, previously observed on other photocathodes [116] may be the result of removal of water from the surface, or more probably, due to bromine desorption during the heating process [62].

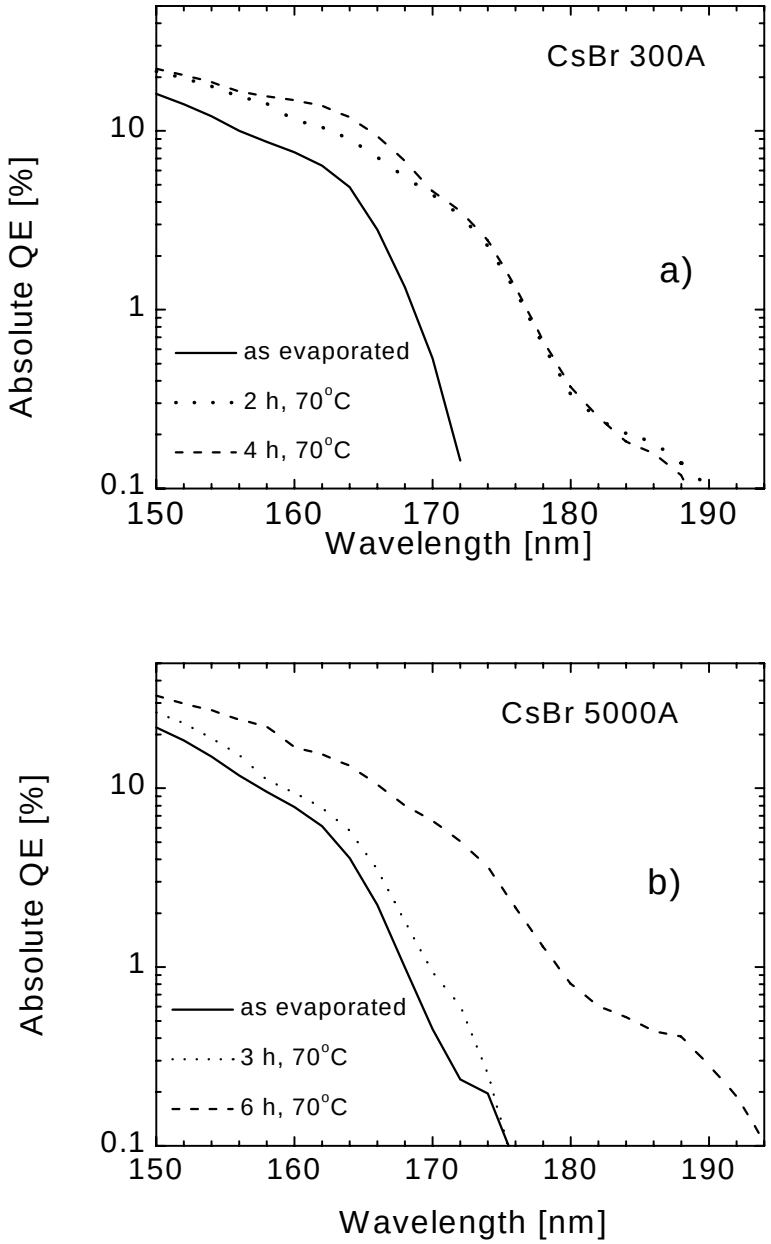

Fig. 3.3: *Absolute QE spectra of CsBr photocathodes. a) 300Å thick photocathode, as deposited and after 2 and 4 hours at 70^0C and b) 5000Å thick photocathode as deposited and after 3 and 6 hours at 70^0C.*

3.2.4 Photoelectron energy spectroscopy.

Photoelectron energy distribution was measured by the method described in section 2.1.4. Figure 3.4 shows the energy distribution induced by 4.9eV photons. The photoemission threshold of CsBr, taken from ref. [62,63] is 7.3eV; therefore, the signal is probably emitted from impurity levels located inside the energy gap. Due to the low electron yield, no distribution was measured for 6.7eV. Exposing the photocathode to ambient air for 10 minutes did not change the energy distribution measured for 4.9eV photons (see fig. 3.4). However, a small signal was measured at photon energy of 3.96eV, which was not present before exposure to air.

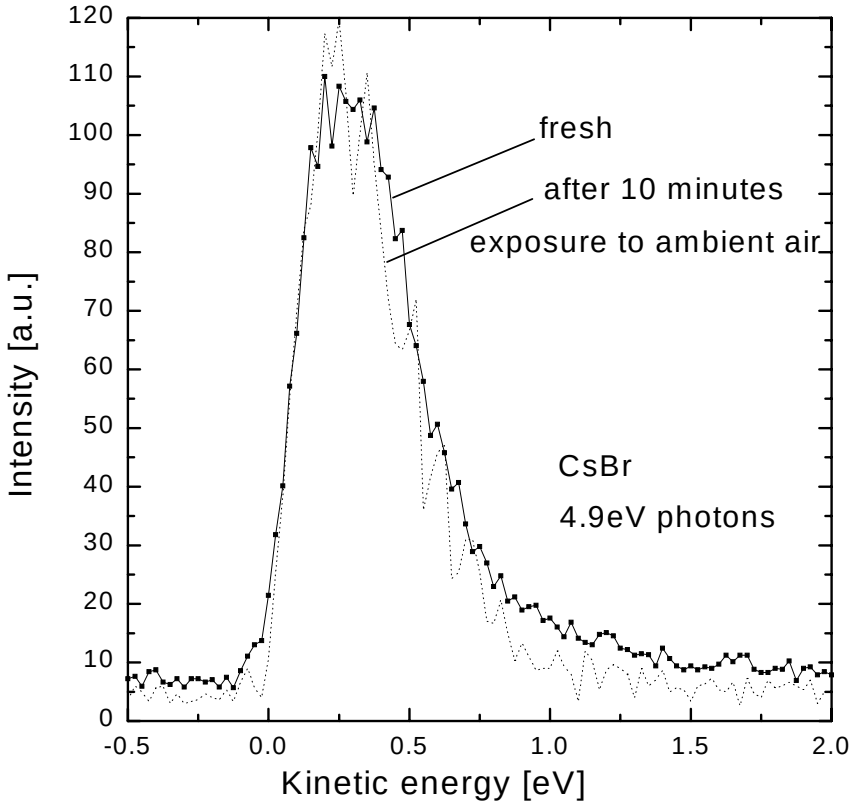

Fig. 3.4: *Photoelectron energy distributions from a 2000Å thick CsBr photocathode, induced by 4.9eV photons. Shown are the normalized distributions from the photocathode as deposited and after a 10min exposure to ambient air.*

An interesting phenomenon was observed when exposing CsBr to x-ray illumination. Figure 3.5 shows the photoelectron energy distribution, induced by 4.9eV photons, before and after illumination of the photocathode for 10 sec, with 1.5keV x-rays. After the short illumination the photoyield is 15 times larger than observed before illumination. This effect decays rapidly on a scale of minutes, and then slower on a scale of hours until it reaches the original intensity after 60 hours. We speculate that the x-rays created meta-stable impurity levels by breaking the periodic structure of the photocathode. The photoemission at 4.9eV, which is from impurity levels, was enhanced due to the higher density of states at the impurity levels, and then decayed over a few hours as the density of the impurity states returned to its original value.

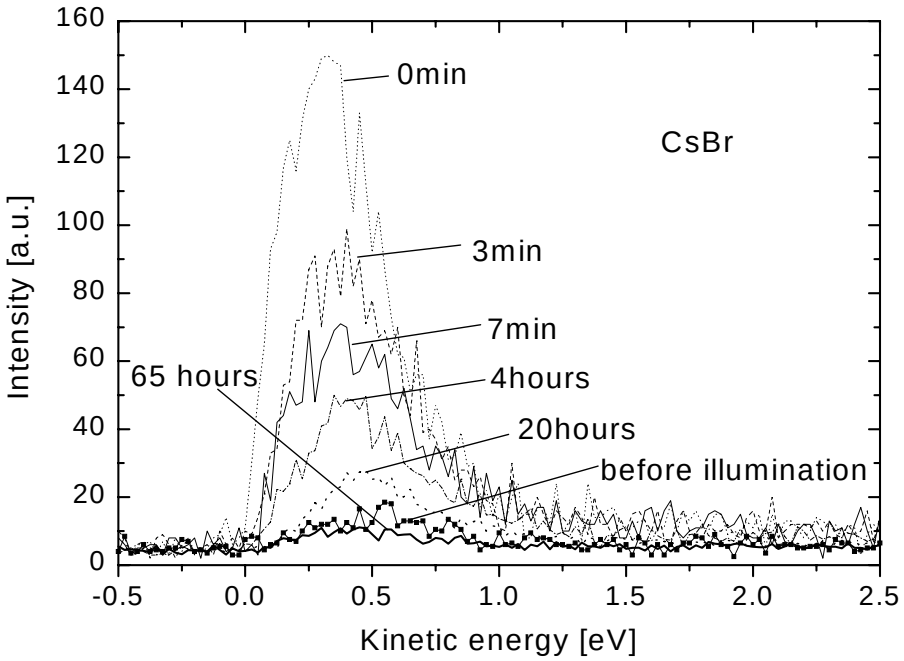

Fig. 3.5: *Photoelectron energy distributions from a 2000Å thick CsBr photocathode, induced by 4.9eV photons. Shown are the distributions before and at different times after a 10sec illumination of the photocathode by 1.5keV x-rays.*

3.2.5 Stability in gaseous environment.

Air was introduced into the chamber, for different time periods, followed by QE measurement in vacuum. It was observed that a short-term exposure (20 min) to air inside the chamber does not deteriorate the QE value. However a 25% drop in QE was observed after 9 hours of exposure to humid air inside the chamber. The exposure of the same photocathode for 40 minutes outside the chamber, resulted in a further 30% decay in QE. Extensive scanning electron microscope (SEM) study of the surface morphology of CsBr [64] showed that CsBr films, when exposed to humidity, undergo a drastic morphological transformation, the small grains coalesce into large, separated grains. This is believed to cause the QE decay in air, by the considerable reduction in surface-coverage.

3.2.6 Aging by photons and ions

Photon aging studies of thin (300Å) and thick (5000Å) CsBr photocathodes in vacuum and in 1 atm. of CH_4 were carried out. The results are presented in fig. 3.6. 20% loss of QE in vacuum was observed after ~10μC/mm^2 and in gas after more than 230μC/mm^2 and 130μC/mm^2 for the thin and thick photocathodes, respectively. This is in agreement with results of photon aging of CsI [95], where aging in gas was considerably slower than in vacuum. We hypothesize that the QE decay is caused by the photolysis process, whereby the chemical bond between Cs and Br is broken and Br atoms are evaporate from the surface leaving it rich with Cs. The process of Br evaporation should be considerably slowed down in gas.

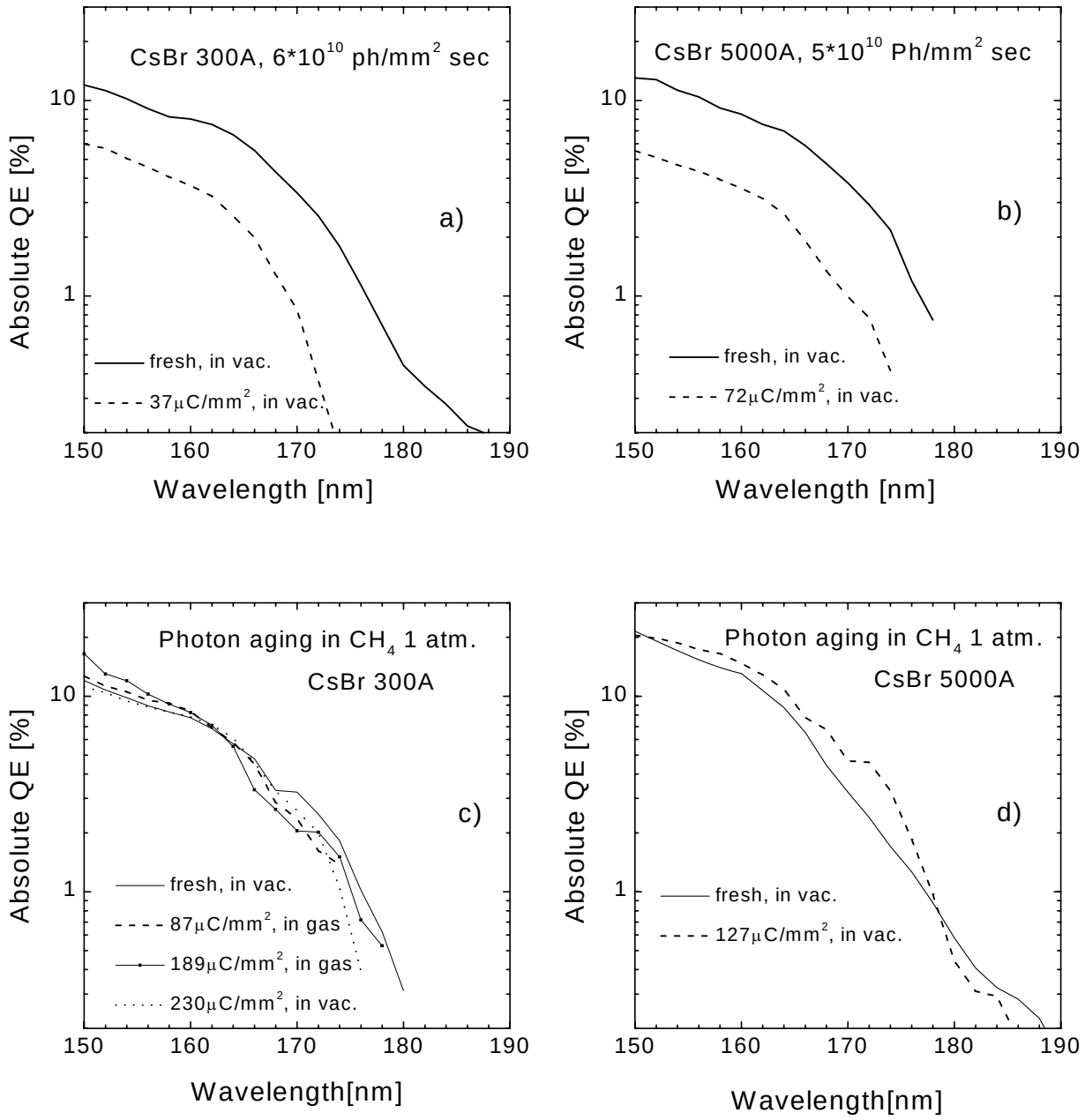

Fig 3.6: *Photon induced aging of CsBr photocathodes a) in vacuum, 5000Å thick CsBr photocathode, b) 1 atm. methane, 5000Å thick CsBr photocathode and c) 1 atm. methane, 300Å thick CsBr photocathode. Shown are the absolute QE spectra measured in vacuum before and at the end of the aging test.*

Aging by avalanche ions was investigated in 50Torr CH_4, at gas gains of 10^3 and 10^4, in parallel-plate avalanche mode. In general, thick photocathodes were more stable than thin ones. Fig. 3.7 shows the results of aging of a thick and thin CsBr photocathode at gas gains of 10^3 and 10^4. 20% loss of QE was observed at a gain of 10^3 after 13μC/mm^2 and 1.5μC/mm^2 for thick and thin photocathodes respectively. The photocathodes aging at a gain of 10^4 was much slower, and no aging was observed for the thick one. It is surprising that high gas gain caused less aging than the low one. This phenomenon is not yet explained and further investigations are required. Comparing CsBr to CsI ion aging, shows that for low gas gain CsI is more stable while for higher gas gains CsBr is aging far less than CsI.

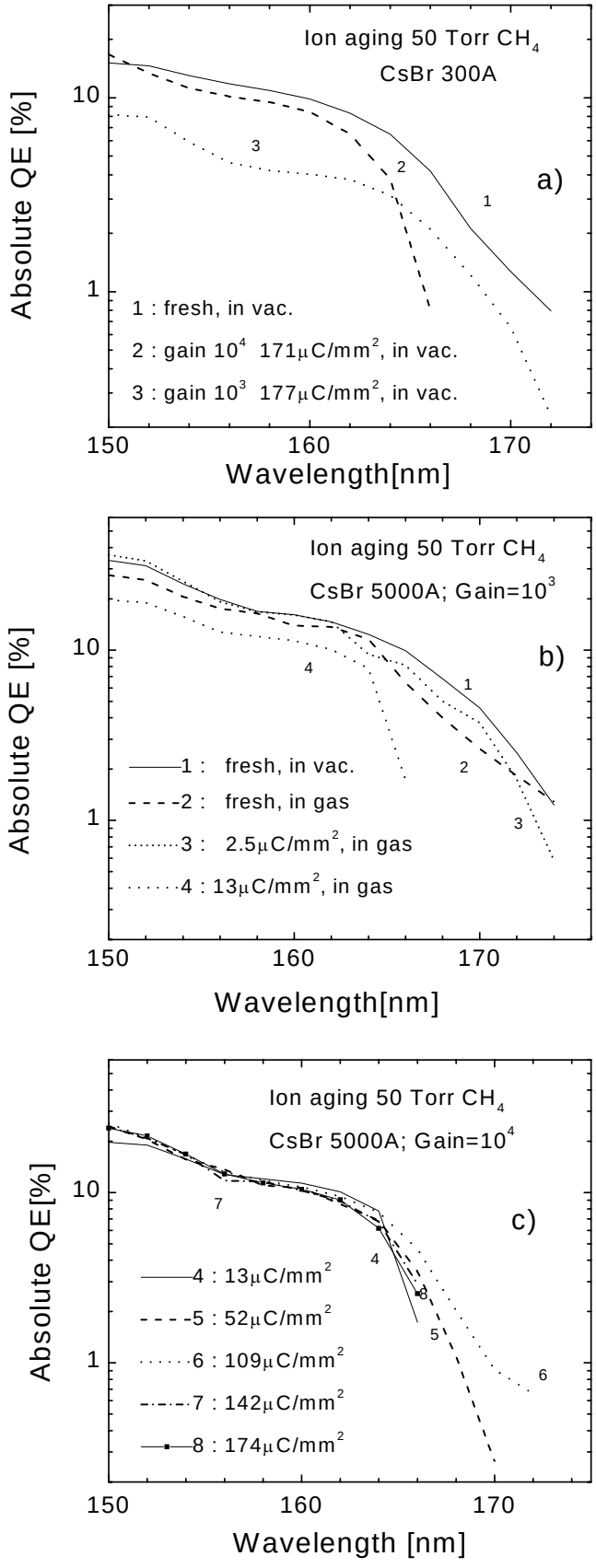

Fig. 3.7: *Ion induced aging of 5000Å thick CsBr photocathode in 50Torr of methane with a gas gain of a) 10^3 and b) 10^4. Shown are the absolute QE spectra measured in vacuum before and at the end of the aging test.*

4. Gas avalanche electron multipliers

As discussed in section 1.2.1, the type of electron multiplier coupled to the photocathode plays a crucial role. On one hand it should provide high gain and permit good electron extraction efficiency, in order to efficiently detect single photons and on the other hand, its operation mode should prevent an accelerated degradation of the photocathode and limit its exposure to avalanche generated, photon- and ion-feedback effects. In addition, the photoelectron extraction efficiency strongly depends on the counting gas and on the electric field at the photocathode vicinity due to electron back-scattering process [43]. A high electric field increases the electron extraction efficiency, but it also increases the velocity of the back-drifting ions, causing a faster degradation of the photocathode surface.

The worst choice for an electron multiplier would be the parallel-plate avalanche chamber, where a high field is applied between the photocathode and a parallel anode electrode. Here all avalanche-induced ions sputter the photocathode at high velocity. Multi-step avalanche chambers, where the avalanche process occurs in successive parallel-grid elements, would be a better choice; it offers very high gain and only a fraction of the avalanche ions return to the photocathode [37]. Large-area CsI-based photon detectors generally employ multiwire proportional chambers (MWPC) [3]. Here, the avalanche is limited to the vicinity of anode wires and the ions have a high velocity only there; they slow down at the photocathode region. Also, due to the field line distribution, only a fraction of the ions reach the photocathode.

The recently developed micro-pattern gas avalanche electron multipliers [44] and the GEM [45] are attractive for photocathode-based photon detectors because their combination provides high gain, fast pulses and a considerably reduced ion-feedback to the photocathode. The GEM may greatly reduce photon-feedback effect. Here we present the results of our investigations, mostly of the very particular operation of these multipliers at low gas pressures.

Operating a gaseous multiplier at low-pressure gas has a few advantages over the standard operation at atmospheric pressure. Low gas pressure operation of the multipliers is characterized by fast ion clearance from the avalanche region and large electron diffusion in the avalanche. These considerably reduce space charge effects and allow reaching high counting rates [117]. The expansion of the avalanche size due to the large diffusion at low gas pressures also results in a larger number of electrodes on which a signal is induced. This enables a more accurate interpolation of the charge distribution, leading to a better localization resolution. The dependence of the gas amplification on the reduced electric field, E/p [118], results in higher gains at low-pressure compared to standard atmospheric conditions. However, the ions reaching the photocathode at low pressure are more energetic and may therefore induce more damage to the photocathode [37].

4.1 Micro-pattern multipliers

The micro-pattern electron multipliers are composed of metal electrodes deposited on an insulating substrate (glass or silicon) [44]. The electrodes may be shaped as alternating anode and cathode strips as in fig 1.1 (micro-strip [119]), as dot-like anodes surrounded by a circular cathode rings (micro-dot [120]), as cathode strips over-layered with thinner anode strips (micro-gap [121]) or in other patterns. Fig. 4.1 shows a scheme of a micro-dot electron multiplier. The typical size of an anode-cathode cell would be 100-200μm and the anode diameter would be less than 20μm. In a photo-detector combining a photocathode and a

micro-pattern electron multiplier, the electrons, emitted from the photocathode, drift towards the micro-pattern electrode where they are multiplied. The avalanche ions are collected partially by the patterned cathodes (see fig. 1.1), reducing the flux of ions back-drifting to the photocathode and allowing for high counting rates. The ion reduction depends upon the electric field configuration.

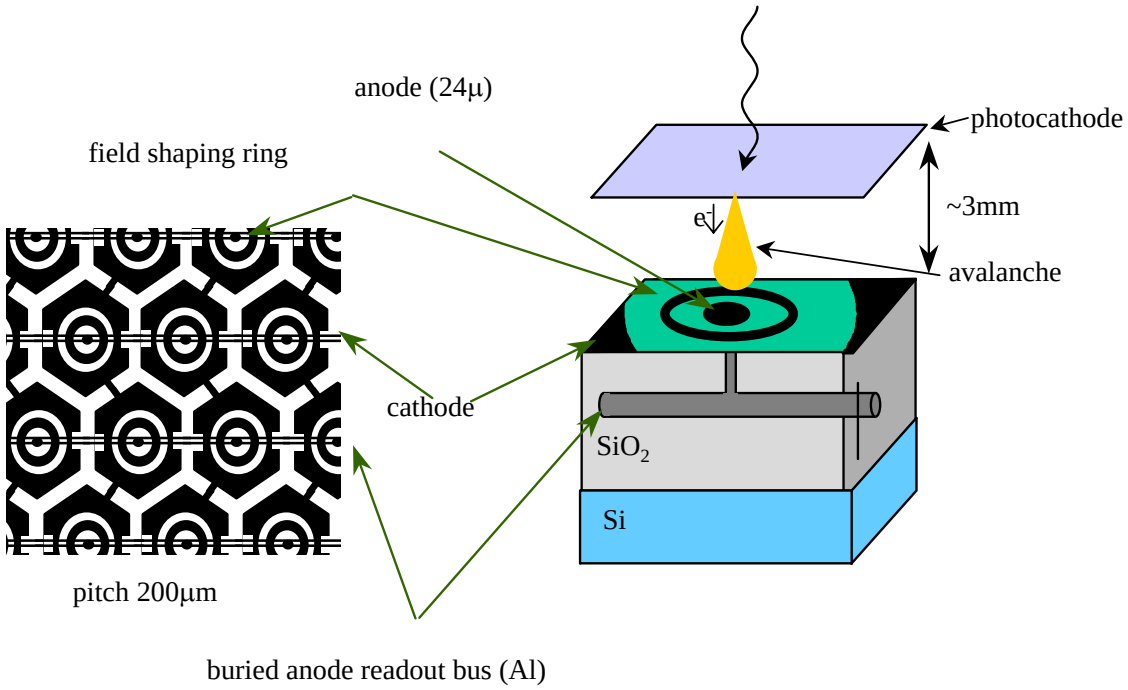

Fig. 4.1: *A scheme of the micro-dot gas avalanche chamber and of a typical electrode layout having 200μm pitch structure. The avalanche is taking place around small anode dots and parts of the ions are collected at the cathode rings.*

We operated the micro-strip and the micro-dot detectors at low pressures of 5-100Torr in hydrocarbon gases [40,122,123]. Stable operation at gains of 10^3 and 10^5 were measured for micro-strip and micro-dot detector equipped with a photocathode, respectively. The gain could be a hundred times larger when the multiplication started in the drift region, under high electric field, and was followed by multiplication at the micro-patterned electrode (see fig. 1.1).

Very large and fast (2-3nsec rise time) single-electron pulses were measured using a fast current amplifier. In the case of a micro-dot multiplier, the pulses, shown in fig. 4.2, were large enough to be recorded without an amplifier [123].

The fraction of back-drifting avalanche ions was measured for a micro-strip geometry operated at different voltages and gas pressures. Increasing the anode-cathode strip potential difference results in a decrease of the fraction of back-drifting ions because more ions are collected at the cathode strips. Decreasing the gas pressure in the detector resulted in a decrease in the fraction of back-drifting ions from 40% at atmospheric pressure to 20% and 10% at 50 and 10 Torr respectively [122].

a) b)

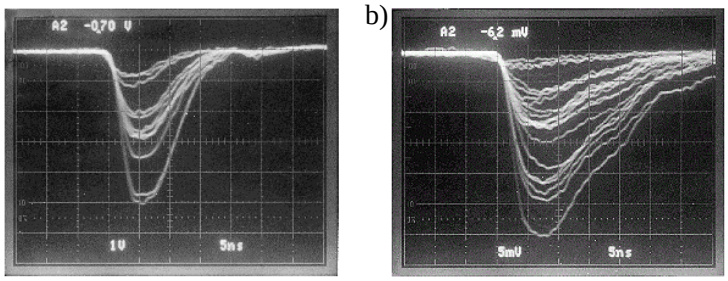

Fig. 4.2: *Photographs of single electron pulse of micro-dot electron multiplier, recorded a) after a fast (0.5 nsec rise time) amplifier and b) directly from the anodes on a 50Ω impedance, at 60 Torr C_3H_8. The rise time is ~3nsec in both cases.*

4.2 The Gas Electron Multiplier (GEM)

The GEM [45,124] could particularly suit our application due to its very special electrode geometry. Figure 4.3, shows a scheme of a GEM. It consists of an array of small (50-100μm in diameter) apertures in a metal-coated 50μm thick, Kapton foil. A voltage difference applied across the GEM electrodes leads to a strong dipole field inside the apertures. Photoelectrons, extracted from the photocathode, are strongly focused into the GEM apertures and undergo a multiplication; they are then transmitted to a further multiplication element such as a micro-strip or a micro-dot electrodes.

a)

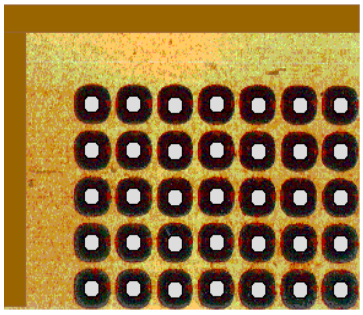

b)

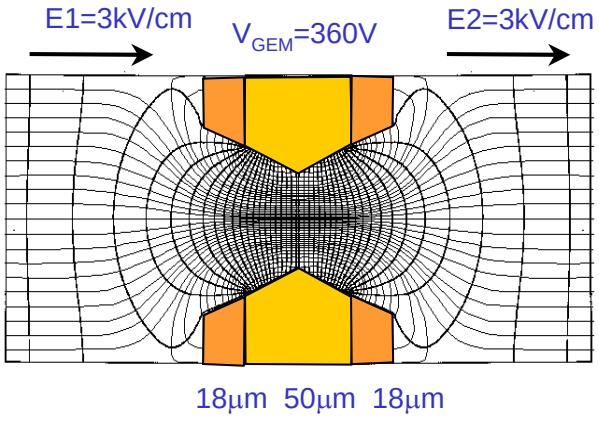

Fig. 4.3: *The Gas Electron Multiplier. Shown are a) the GEM array of small apertures in a cooper-coated kapton foil and b) the electric field lines in one aperture.*

We operated GEM at gas pressures ranging from a few Torr to 1 atmosphere [125-127]. Fig. 4.4 shows GEM multiplication curves, measured at 40-400Torr using different gases. The GEM gain was more than 10^4 at lower pressures and gains of 1000 could be achieved at the

higher-pressure range. The GEM can be employed as a preamplifiying element, preceding another electron multiplier [124,125]. Some gain on the GEM will permit reducing the gain of the following multiplication element, leading to more stable operation. Multi-stage multipliers would allow for reaching higher gains, increasing the sensitivity to single electrons, as discussed below.

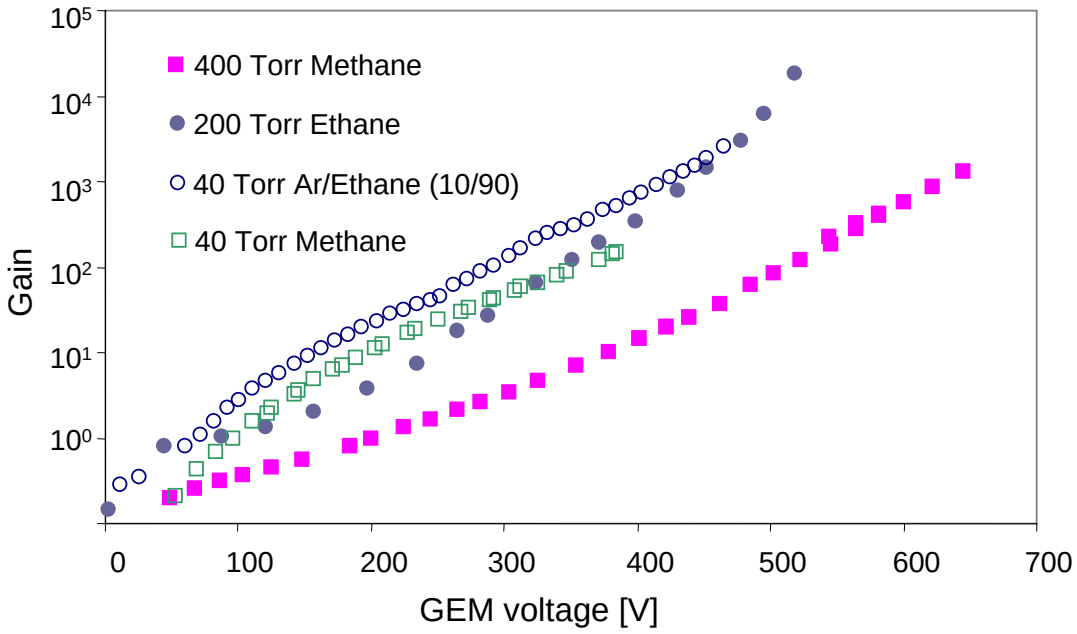

Fig 4.4: *Gain curves as a function of the potential across the GEM, for different gases and pressures.*

We showed that inserting a GEM between the photocathode and another multiplying element reduces the photon feedback, which limits the gain of photon detectors and distorts the image [125]. At some electric field configurations, the GEM would also block a fraction of the back-drifting avalanche ions. Both the photon- and the ion-feedback would be decreased farther by cascading a few GEM elements, as is shown schematically in fig. 4.5 [41]. This detector, in which the GEMs are the only gas multiplication elements and the readout is performed using a printed circuit board, reached high gains of 10^6 at atmospheric pressure (see fig. 4.6) as well as very fast anode signals of a width of 15nsec [41]. Furthermore, such multi-GEM multiplication structure could operate in pure noble gases. Due to the screening of photon feedback, gains above 10^5 were reached in pure argon [41].

By optimizing the electric fields above and below the GEM and by initiating a small pre-amplification before the GEM, detection efficiency of 100% for single photoelectrons was achieved [127]. It was demonstrated that the pre-amplification may improve the photoelectron detection efficiency only if the lateral spread of the pre-amplified cluster is large compared to the GEM's aperture pitch. Hence the electron diffusion plays a crucial role. The pre-amplification at the photocathode-GEM gap is also beneficial for reaching full electron extraction efficiency from the photocathode, as the electron back-scattering to the photocathode is practically eliminated [43]. We have recently sealed a CsI-based gaseous photomultiplier equipped with a 3-GEM element [128].

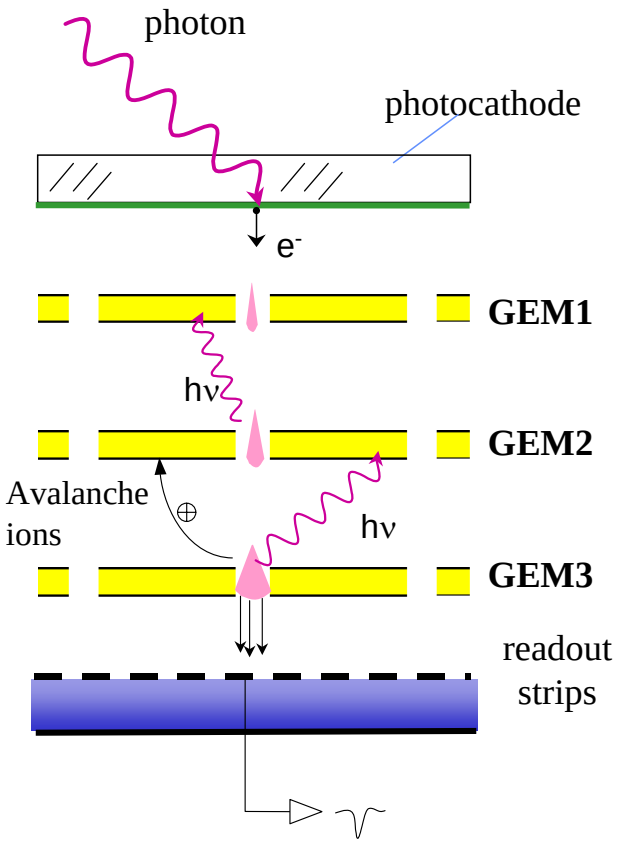

Fig 4.5: *A multi-GEM photomultiplier consisting of a cascade of GEMs coupled to a photocathode. Each GEM operates at a low gain, resulting in a high total gain. The resulting avalanche induced pulses can be recorded on a two-sided printed circuit board, without any additional multiplication, providing 2D localization of single photons. The GEM elements screen the photocathode from photon-feedback and reduce ion-feedback effects.*

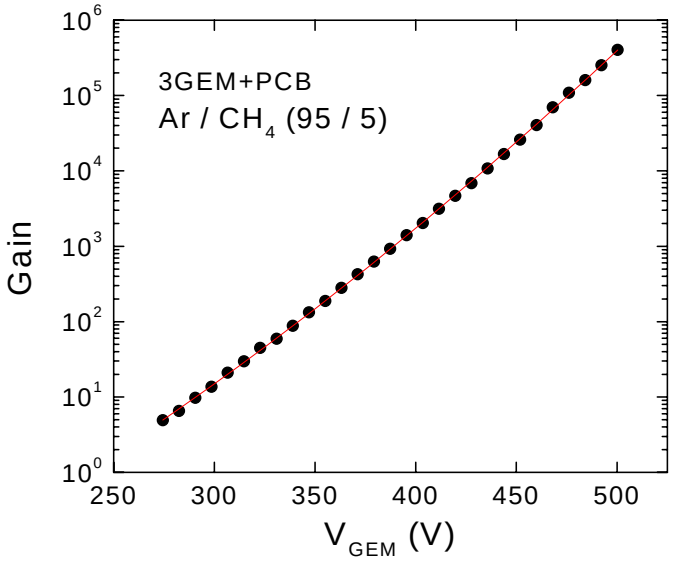

Fig, 4.6: Absolute gain of a gas photomultiplier consisting of a CsI photocathode coupled to a cascade of 3 GEM elements and a readout using a printed circuit board (see fig. 4.5), as the voltage across a single Gem.

5. Discussion

The results of this research work were discussed in detail in chapters 2-4. Here we will present a concise discussion of the main processes and results.

This work aimed at the development of photocathodes to be employed in gaseous photomultipliers in the UV-to-visible spectral range. Most important are photocathodes for the imaging of visible light, which is the major subject of this research work. For this purpose we coated alkali-antimonide photocathodes with thin dielectric protection films. The coated photocathodes were investigated in terms of three related aspects:

- Surface and in-depth chemical composition.
- Quantum efficiency and stability in gaseous environment and under conditions similar to those of a gaseous detector.
- Electron transport properties, including photoelectron energy distributions and QE attenuation length.

Although we experimented with a wide variety of coating materials, including oxides (SiO), organic molecules (n-$C_{36}H_{74}$: HTC, ($[CH_3(CH_2)_{16}COO]_2Ca$: CaSt) and alkali-halides (NaI, CsI, CsBr, NaF, CsF), we focussed here on CsI and CsBr. These two films showed the best results in terms of QE and stability of coated Cs-Sb and K-Cs-Sb photocathodes in gas environment.

5.1 Visible photocathodes in gaseous detectors

The choice of the coating film thickness is a compromise between the need for an efficient electron transmission (high QE), and the need for high stability when exposing the photocathode to impurities in the counting gas. We showed that by varying the coating film thickness, one could tailor the protection capability over a broad range of impurity levels (fig. 2.38). This was verified by XPS measurements. Fig. 2.18 showed the diffusion of oxygen into the photocathode when coated with thin (50Å) protection films compared to thicker coatings (250Å) where oxygen did not reach the photocathode.

The thickness of the film needed for protection of the photocathode depends on the nature of the film and on the state of the protected photocathode. The nature of the film includes its electron transmission efficiency and its ability to stop oxygen and water molecules. The protected Cs-Sb and K-Cs-Sb photocathodes consist of a mosaic of crystallites [57]. Since the surface of such photocathodes is not smooth, the thickness of the coating film needed for effective protection should exceed some threshold value. This value depends most likely, on the crystallite size and on the smoothness of the photocathode surface.

The protection is reached at the expense of a reduction in quantum efficiency. However, for CsI-coated K-Cs-Sb photocathodes, very reasonable values of 5% to 10% at a wavelength of 312nm were reached with respective protection capabilities to 150Torr and 0.1Torr of oxygen (figs. 2.35 ,2.36, 2.38). This should be compared to earlier works by Peskov et al. [6,7], coating Cs-Sb photocathodes with CsI films, resulting in a very low absolute QE of 0.15% at a wavelength 350nm, and by R. Enomoto. et al [129] who concluded that one cannot protect a Cs-Sb photocathode by using a thin CsI film.

The coated photocathodes, though about 3-6 times less efficient than bare photocathodes, when protected against high impurity levels, already have practical applications. Protection against impurities at the ppm or sub-ppm level, typical to counting gases, may require thinner protection films, hence higher QE values may be reached. Indeed we observed in fig. 2.15, as

was done previously by others [6,37,130,131], that filling the chamber with clean methane and pumping it back to vacuum does not reduce the photocathode's QE. However, it is important to ensure that the detector and the filling system are clean and that the gas is of high purity.

Alkali-halide films failed to protect the alkali-antimonide photocathodes against moisture at pressures greater than 10^{-5}Torr (fig. 2.39). Such protection may be achieved by coating the photocathodes with other films, possibly water-repelling polymers [81,86,108], or with double-film layers: the first protecting the photocathode from oxygen and the other from humidity. The presence of moisture in ambient air limits the stability of air-exposed coated photocathodes to 1Torr levels (fig. 2.40). The present levels of stability of coated photocathodes in oxygen and moisture permit photocathode handling in nitrogen-flushed glove box. This by itself is an important achievement, allowing for simple handling and detector assembly.

Coupling a photocathode to a gaseous electron multiplier defines a set of requirements concerning both the photocathode and the electron multiplier. While the photocathode should be resistant to aging by high photon and avalanche-induced ion flux, the electron multiplier geometry and operation mechanism are expected to have most avalanche ions collected away from the photocathode, and a reduced photon-feedback to it.

The coated photocathodes undergo moderate aging (fig. 2.42) and charging up (fig. 2.41) under intense illumination. In our estimation, this should not limit their use even at extreme photon imaging conditions. Preliminary measurements of aging of coated photocathodes by avalanche ions showed that it is comparable to that of CsI. This could be a crucial point, as Edmends et al. reported severe damage to bare Cs-Sb photocathodes by back-drifting ions [38]. Peskov et al. reported that coated Cs-Sb photocathodes are more stable than bare ones, under gas avalanche conditions [7]. It should be remarked that the ion-aging experiments were carried out at the worst possible conditions, namely under parallel-plate multiplication at low gas pressure. The aging data provide therefore an upper value. Much lower aging is expected in adequate multiplication geometry.

Minimizing the flux of back-drifting avalanche ions, in order to decrease possible damage by ion sputtering, is an important aspect in choosing the electron multiplication geometry. Micro-pattern gas electron multipliers such as micro-strip, micro-gap and micro-dot are good candidates. In such multipliers a large fraction of the avalanche ions is collected on the micro-pattern electrode, limiting the photocathode damage. Inserting the newly developed GEM between the photocathode and the electron multiplier would also decrease the ion impact as well as the photon feedback. It was recently shown that it is possible to reach a detection efficiency of 100% for single photoelectrons in such geometry [127]. Studies of coated photocathodes coupled to a GEM and a micro-pattern electron multiplier are in course. A very promising possibility is multi-GEM configuration (fig 4.5, 4.6), in which high gains, fast anode pulses and reduced ion- and photon-feedback were observed.

A work of special importance for the prospects of coupling a visible photocathode to a GEM was recently presented by Buzuluztkov et al. [41]. The GEM was operated in noble gases such as argon and neon and in gas mixtures of argon with xenon, neon, methane or nitrogen. Very high gains, reaching 10^6 at atmospheric pressure, were observed when cascading 3-4 GEM elements; pulses of 10ns width were recorded on the anodes. The possibility of multiplication in a noble gas is the result of the strong electric field confined to the small GEM holes, which effectively hinders photon-mediated secondary avalanches

[132]. The inert noble gases could prevent the chemical aging of the photocathodes, thus possibly allowing for their operation with no protection. However, there are still a few problems that require clarification, such as ion-feedback and charging up of the GEM electrodes. Moreover, the GEM is based on a kapton foil that outgases and therefore it may be incompatible with bare visible photocathodes. A possible solution would be glass-made GEM electrodes. Peskov et al recently proposed the use of a GEM-like micro channel plate (MCP) structure for this purpose [133]. However, special low-resistivity glass has to be used as to avoid charging up problems, particularly at high counting rates.

5.2 Electron transport properties.

Low-energy electron transport through thin alkali-halide films, used as protective coatings, was studied, to provide better understanding of the operation of coated photocathodes. For this purpose we considered the alkali-antimonide photocathodes as the source of electrons, injected into the coating film. This was possible because of the transparency of the coating film to the photons having energy smaller than the coating-film gap energy. The method of photo-injecting electrons differs from standard photoemission studies as it involves injection of electrons at a known depth and enables the study of electron scattering in the coating film material, disregarding photon absorption coefficients. However, the injected electrons are not mono-energetic. In this work, their energies were in the 0-4eV and 0-1.8eV ranges for 4.9eV and 2.85eV photons respectively. This method was used successfully by others such as DiStefano et al. [71] who studied hot-electron scattering in CsI, by photo-injecting electrons from copper and gold photocathodes. Buzulutskov et al. [68] coated CsI and CuI photocathodes with numerous alkali-halides, alkali-earth halides, oxides and organic films in order to study very low energy (~1eV) electron transport properties.

Coating a photocathode with a thin film results in the creation of a potential barrier between them. This was demonstrated by the attenuation of the photoyield caused by the first few tens of Angstroms of coating (fig. 2.21), which was also observed for other interfaces [68]. It could be speculated that this strong initial attenuation in photoyield represents the fraction of coated surface before full surface coverage is achieved. Indeed XPS measurements showed that up to a 50Å thick coating, there is no full coverage of the underlying photocathode. However, the observed attenuation is more drastic than expected from the geometrical factor of surface coverage. Moreover, the dependence of the attenuation over the first 10-50Å thick layer on the photon energy shows that it represents the creation of a potential barrier.

A model developed in our group [76,48], describing low-energy electron transport in alkali-halides, was modified in the framework of this thesis to include the role of the photocathode-coating film interface. The interface was roughly approximated by a step function, neglecting possible diffusion of elements between the photocathode and the coating film. The model treats the coating film as an ideal monocrystal, disregarding impurities and its polycrystalline structure, which could have an effect on low-energy electron transport. Monte-Carlo simulations, based on this model were carried out, calculating QE attenuation length and photoelectron energy distributions.

It was found that in order to obtain good agreement between measured and calculated results, the model had to include the possibility of electrons traversing the photocathode-coating film interface several times. Each step of interface-crossing back and forth involves a fixed energy loss, used as a free parameter of the model. The best value for the energy-loss

parameter was found to be 0.2eV, by minimizing the difference between calculated and experimental QE attenuation length.

It is known [64] that a few hundred Angstroms thick alkali-halide films exhibit a morphology of crystellites having a diameter of a few hundred angstroms. In the low energy range of a few eV, the de Broglie wavelength of the transported electrons is of the order of magnitude of a few tens of Angstroms and is thus only one order of magnitude smaller than the typical size of evaporated crystallites. The single-crystal approach for the electron transport, adopted in our model and shown previously to be successful [48,77], is therefore only partially justified in this case. Indeed, the calculated QE attenuation length values are larger than the measured ones. This was explained in section 2.3.2.3 by the trapping of photoelectrons at the interfaces between the crystellites that was not taken into account in our model. This trapping would affect more strongly the very low-energy electrons and would result in shorter QE attenuation length for low energy photons, (2.84, 3.05eV) for which the photoelectron energies vary in the 0-2eV range.

We also measured the photoelectron energy distributions for CsI and CsBr coatings of K-Cs-Sb varying both the photon energy and the coating-film thickness. To the best of our knowledge this was never done before. The model was verified by comparing experimental and calculated photoelectron energy distributions, varying the coating material (CsI, CsBr), photon energy (2.85eV, 3.05eV, 3.38eV, 3.96eV and 4.9eV) and film thickness (50Å, 250Å, 350Å and 500Å). Since there is only one free parameter in the model, the good agreement found between measurements and calculations is a good indication of the model validity.

The small discrepancy between experimental and calculated photoelectron energy distributions, presented in figs. 2.31-2.34, may be the result of an inaccurate photoelectron-input distribution. This was explained in detail in section 2.3.2.4. The measured photoelectron energy distribution for 50Å thick coating, which is the simulation-input distribution, suffers from strong influence of surface states and roughness. These affect the 50Å thick coating much more than the thicker films, due to the greater order and full surface coverage in the thicker films. As a result, the input distributions are distorted and the calculated photoelectron energy distributions are distorted in the same way.

The photoelectron energy distributions measured for thicker coatings are narrower and the peak positions are at lower energies than that of thinner coatings (fig. 2.29). Both effects are more pronounced for the more energetic photons, suggesting that the CsBr and CsI films have larger attenuation for more energetic electrons. The mean-free-path between phonon-electron scattering has a maximum at approximately 0.5eV and for higher energies it is dominant by the mean-free-path for acoustical phonon-electron interactions. As a result, the more energetic electrons have more frequent interactions, mostly with acoustic phonons that involve isotropic electron angular deflection. The shorter mean-free-path and the isotropic angular deflection result in the observed larger attenuation for more energetic electrons.

The threshold energy for photoemission from the coated photocathode was extracted from the photoelectron energy distributions. The values are 2.0±0.15eV 350Å for a thick CsBr coating and 2.25±0.1eV and 2.5±0.2eV for 250Å and 500Å thick CsI coating films. In the case of CsI, the thinner, 50Å thick coating film, has lower threshold energy value of 2.07±0.06eV; it is probably due to the fact that we did not observe full coverage of the underlying photocathode. For the CsBr coating, in which better coverage of the K-Cs-Sb photocathode was observed for 50Å thick films, the photoemission threshold energy is 1.97±0.08eV.

One important conclusion of this work is that the electron transport and therefore, the QE attenuation length and the photoelectron energy distributions, **depend both on the photocathode and on the coating film**. This is due to the influence of the photocathode-coating film interface and to the fact that the structure and surface of the underlying layer affect the structure of very thin coating films. The dependence on the photocathode is expected to be smaller for thicker coating films.

Taft et al. [51,72] observed the onset of a two-electron cascade between 4 and 4.9eV in K-Cs-Sb and in Cs-Sb. This results in more electrons of low energy, photo-injected into the coating film when illuminating the photocathode by 4.9eV photons compared to lower energies. The maximum observed for the QE attenuation length at a photon energy of 4eV (fig. 2.24) corresponds to the most energetic photoelectrons emitted from the photocathode. The two-electron cascade also influences the photoelectron distribution shape shown in fig. 2.29. The peak position of photoelectrons induced by 4.9eV photons is not at a larger energy than that induced by 3.96eV. It is also clear that the shape of the photoelectron distribution induced by 4.9eV photons is different from the shape induced by lower energy photons.

5.3 UV photocathodes

In the UV spectral range, the properties of DLC and CVD diamond films and that of CsBr were examined in detail. DLC films have both sp^2 and sp^3 carbon bonds, while CVD diamond films have only sp^3 bonds. It was found that carbon sp^2 configuration (graphite) strongly attenuates the absolute QE values. This is due to the electronic band structure of the graphite, considered as a semimetal. Semimetals are defined as metals having carrier concentration of several orders of magnitude lower than typical metals [134]. As a result, the photoelectrons energy is sufficient to excite secondary electrons in the graphite, each having a lower energy than the original photoelectron. There is a large probability that the low-energy secondary electrons will not have sufficient energy to escape into the vacuum. DLC films, even with high sp3 concentration were found to have QE values that are too low for any practical application, probably due to the graphite-rich surface layer.

On the other hand, CVD diamond films have reasonable QE and they are chemically stable. Surface treatment of these films by hydrogen plasma, discussed in section 3.1.3, increased their QE by two-fold, to values above 12%. Oxygen termination, on the contrary, was found to cause a strong QE decrease. Indeed the QE of a hydrogenated CVD film, stored in ambient air, decreased due to oxygen adsorption on the surface. To the best of our knowledge, it is the first time that photoemission from CVD diamond films was found to have long-term instability in air.

CVD diamond films could be attractive photocathodes for applications requiring moderate efficiency, radiation hardness and robustness, also at high temperatures. Indeed vacuum photomultipliers, consisting of CVD diamond photocathodes recently became commercially available.

CsBr solar blind photocathodes have a photoemission cutoff at approximately 174nm. The absolute QE values measured in reflective mode at 150nm were 15% and 21% for 300Å and 5000Å thick photocathodes, respectively. The increase in QE for thicker films is attributed to an increased photon absorption at thicker films. Post-evaporation heating of the photocathodes to 70^0C for a few hours resulted in a decrease in the photoemission cutoff by 0.7eV and a substantial enhancement of the QE value for all photon energies (35% at 150nm). Possible explanations for the heat enhancement are the removal of water or bromine

desorption from the surface, the latter resulting in a Cs-rich surface. Cs-rich surfaces are known to enhance the QE due to the creation of strong band bending at the surface. The latter explanation is supported by XPS measurements characterizing the surface of the photocathode in which the Cs-to-Br ratio was found to be 1.3. It is also well known that the vapor pressure of Br is much higher than that of Cs [102].

Photoemission from impurity levels is an important process in CsBr photocathodes. This was clearly observed in the photoelectron energy distributions of heat-treated photocathodes induced by 4.9eV photons. The energy gap of CsBr is approximately 7eV [76], therefore, these electrons were emitted from impurity levels. It is possible that heating the photocathode creates impurity states that give rise to an increase in the total photoemission and a shift in the red boundary cutoff.

After a short illumination of the photocathode by 1.5KeV photons, the photoyield increased by a factor of 15! This increase in the photoyield slowly decayed until it reached the original intensity. We hypothesized the creation of meta-stable impurity levels during the x-ray illumination. This effect, which was observed by other groups [135], should be investigated in detail.

Exposing CsBr photocathodes to air for 20 minutes did not degrade the photocathode QE. This is important for applications in which the photocathode preparation and the detector assembly take place at different locations. Longer exposures for a few hours, resulted in up to 50% decrease in QE. It is known that such long exposures induce a morphological transformation in the photocathode, resulting in a reduction in the surface-coverage [64]. The photocathode stability under high photon and ion flux was measured. The results are comparable to those of CsI photocathodes [2], therefore, we do not anticipate that this would limit their use.

To conclude, CsBr may be an efficient solar blind photocathode and can operate in both vacuum and gas avalanche photomultipliers.

5.4 Applications and future investigations

We showed that the coating of alkali-antimonide photocathodes, by thin alkali-halide films might permit, for the first time, the operation of a visible photocathode in a gaseous environment. This is an important step towards large-area fast detectors for imaging visible light.

Such fast, large area gas avalanche imaging detectors, sensitive in the UV-to-visible spectral range, capable of operation at repetition rates superior to a MHz/mm^2 and under high magnetic fields can be used in scintillation calorimetry, scintillating fiber trackers and large medical imaging detectors.

The development of a new gaseous photon detector for two-dimensional digital x-ray imaging for mammography is in course. The research work is done in the framework of a European Community collaboration involving: Agfa Gevaert-Antwerpen, Electron Tubes-London, INFN-Pisa, IMEC-Louvain, Vrije University-Brussels and our group [136]. A scheme of the proposed x-ray imaging detector and a picture of the photon detector are shown in figures 5.1 and 5.2. X-ray photons transmitted through tissue are absorbed in an erasable phosphor film creating meta-stable states. Illuminating the phosphor with a red light laser results in the decay of these states and the emission of photons in the blue spectral range. These photons are detected by an alkali-antimonide photocathode coupled to a micro-strip gaseous electron multiplier (see section 4.1) operated at 1 atm. of methane. This x-ray

imaging detector is expected to be faster and have an improved contrast compared to present mammography techniques.

Our group contributed in the development of the gas-stable visible photocathodes and their sealing technique to a package containing the electron multiplier. Figure 5.2 is a picture of a photocathode sealed to such a detector package. The sealing is done by means of hot indium deposited on the circumference of the photocathode and the package.

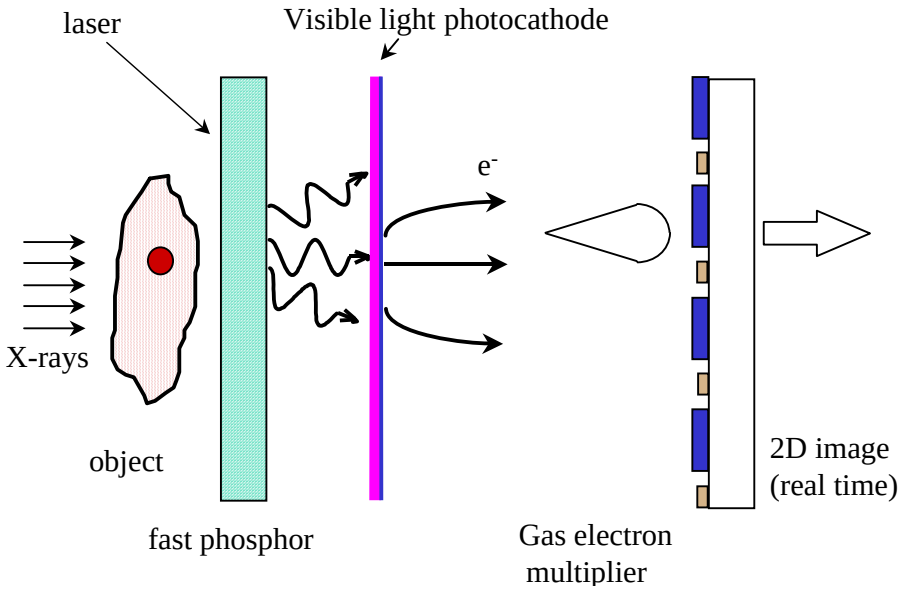

Fig. 5.1: *A scheme of a 2D digital x-ray mammography imaging detector. X-ray photons, traversing the object produce a latent image on an erasable phosphor. Laser illumination of the phosphor induces the emission of visible light, which is transformed into photoelectrons in a visible photocathode. The photocathode is located within a gas avalanche electron multiplier (here a micro-strip detector), providing after multiplication fast 2D images of the irradiated object.*

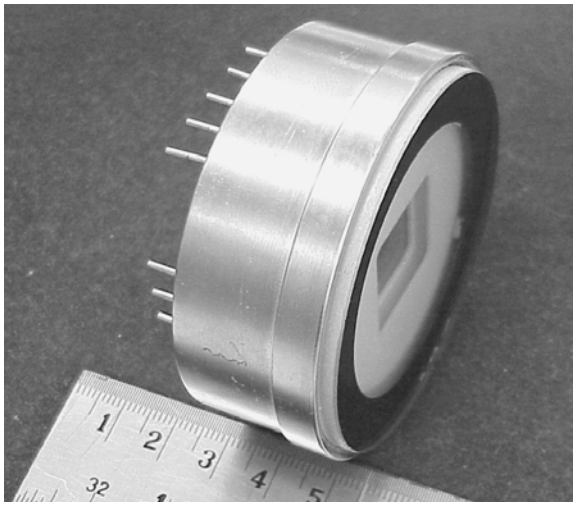

Fig. 5.2: *A picture of the sealed position-sensitive gas avalanche photomultiplier developed within this work. The window is gold-evaporated on the circumference, and the photocathode is evaporated on its central part. This particular detector contains a 3-GEM multiplier coupled to a CsI photomultiplier.*

Another possible application could be in RICH (Ring Imaging Cherenkov) detectors. The CsI- and CsBr-coated K-Cs-Sb photocathodes offer a spectral sensitivity over a wider energy range (cutoff at 2.8eV) compared to TMAE or to CsI UV-photocathodes. This could be useful when applying them to RICH devices used for particle identification in particle and astroparticle physics, provided higher QE values could be reached. The RICH detector response parameter, N_0, is defined as:

$$N_0 = \frac{\alpha}{\hbar c}\int (QE \cdot T \cdot R)dE \tag{5.1}$$

where α is the electromagnetic fine structure, T is the detectors window transmission and R is the detectors reflectivity (mirror and radiator) [137]. For a radiator reflectivity coefficient of 1, a quartz window with transmission coefficient of 0.9 and a mirror reflectivity coefficient of 0.9 (all coefficients are energy averaged), N_o calculated for a K-Cs-Sb photocathode coated with 280Å and 225Å thick CsI films is 50 and 70 cm^{-1} respectively. This is a low value compared to N_0=137cm^{-1} calculated for TMAE-based detectors, but of the same order as N_0= 80cm^{-1}, calculated for CsI-based detectors (these calculations were done with data from reference [138]). Thinner coating films resulting in larger N_0 values may have sufficient protection capability for practical applications.

Our results of coated photocathodes have triggered another application in the field of laser-triggered intense electron sources used in RF cavities [8,139]. Cs_2Te photocathodes, often employed in such sources, are required to withstand relatively poor vacuum conditions for long periods of time. Such photocathodes were recently coated with CsBr films and showed no degradation over long periods of operation [8].

6. Summary

This thesis work laid the foundations for extending the sensitivity of gaseous photon detectors, currently successfully employed in the VUV range (140-220nm), towards the UV-to-visible spectral range (300-450nm). The detection of light in this class of photon detectors is based on the conversion of photons to electrons in a thin solid photocathode, followed by the multiplication of the photoelectrons in a gaseous electron multiplier. These large-area, flat detectors are sensitive down to a single photon level, with very good time and spatial resolutions. The use of photocathodes eliminates time-jitter and parallax errors in localization. The gaseous photomultiplier has very small sensitivity to magnetic fields compared to vacuum-operated photon detectors. Due to the high chemical reactivity of alkali-antimonide photocathodes, sensitive in this spectral range, no such detectors could be constructed so far.

We presented the main results of our search for new photocathodes to be used in gaseous photomultipliers in the UV-to-visible spectral range. We investigated in detail the idea of coating alkali-antimonide photocathodes by thin dielectric films, in order to protect them from contamination by impurities present in counting gases. We systematically characterized the photoemission properties of coated photocathodes by measuring their absolute quantum efficiency (QE) spectra and photoelectron energy distributions. An important part of this work was dedicated to the study of low-energy photoelectron transport properties in the photocathode, the coating layers and through the interface between the two materials. XPS was used to determine the chemical composition of the coated photocathodes and their stability under exposure to counting gases, to high photon flux and under gas multiplication conditions was examined.

We experimented, in two complex dedicated setups built within this thesis work, with a wide variety of coating materials, including oxides, organic molecules and alkali-halides. The best results, in terms of high QE values and good stability in gaseous environment, were achieved with CsBr- and CsI-coated K-Cs-Sb photocathodes. We showed that by increasing the coating film thickness we increase the stability of the photocathode in a gaseous environment at the cost of reducing its QE. For CsI-coated K-Cs-Sb photocathodes, very reasonable QE values of 5% to 10% at a wavelength of 312nm were reached with respective protection capabilities to 150Torr and 0.1Torr of oxygen. Moderates aging and charging up observed under intense illumination of the coated photocathodes are not expected to limit their use.

We studied low-energy electron transport through alkali-halide coating films by measuring the QE attenuation length and the photoelectron energy distributions. We observed that the electron transport properties of the coated photocathode depend both on the photocathode and on the coating film due to the different interface created between them for different materials. The interface between the photocathode and the coating film, giving rise to a potential barrier, is of prime importance for the low-energy electron transport and a large fraction of the photoelectrons excited in the photocathode, are reflected or absorbed in the interface. For coating films thicker than 50Å the electron transport is dominated by the properties of the coating film: a large energy gap and low impurities density would result in good electron transport, while a small or negative electron affinity would increase the escape probability into the vacuum.

A model developed in our group, describing the electron transport process as a sequence of electron-phonon interactions, was modified to include the photocathode-coating film

interface, approximated as a step function. The model includes the possibility of electrons traversing the photocathode-coating film interface several times. This model was used to calculate the QE attenuation length and the photoelectron energy distributions. The good agreement between the experimental and calculated results validates this approach.

Some attention was given to CVD diamond and CsBr films, investigated as UV-photocathodes. Their QE is inferior to presently used CsI UV-photocathodes. However, CVD diamonds are relatively air-stable and radiation-hard and CsBr may be used as solar blind photocathode.

Novel gas avalanche electron multipliers were investigated in operation modes suitable for the application to gaseous photomultipliers. The most promising is the GEM, (Gas Electron Multiplier). Excellent results showing high gain for single photoelectrons, reduced ion- and photon-feedback and electron transmission efficiency of 100% were obtained. Cascading a few GEM elements decreases even further the ion- and photon-feedback, which permits stable operation in pure noble gases. This makes the multi-GEM a multiplier of choice for gas avalanche photomultipliers.

This work is the first to show the plausibility of protecting photocathodes while maintaining reasonable quantum efficiency values. This is a major step in the development of gaseous photomultipliers for UV-to-visible light. The level of protection and quantum efficiency values achieved in this work is of interest for applications in medical imaging and particle physics.

Although this work greatly contributes to the development of gaseous photon detectors for visible light, some issues remain to be investigated. The protection of photocathodes against moisture may be achieved by using water-repelling polymers, possibly as a second protection layer on top of oxygen-protected photocathode. A search for new protecting materials, providing stability in both oxygen and moisture, and having large energy gap, small electron affinity and full geometrical coverage of the photocathode surface is a challenge in the field. The chemical composition of protected photocathodes, as well as the mechanism responsible for successful protection should be investigated, to assist the search for new protecting materials. The low-energy electron transport modeling may be extended to include impurities, polycrystalline structures and other types of materials. The long-term operation of photocathodes in an appropriate gaseous electron multiplier has to be studied systematically.

Literature

[1] A. Breskin, T. Boutboul, A. Buzulutskov, R. Chechik, G. Garty, E. Shefer and B.K. Singh, “Advances in gas avalanche photomultipliers”, Nucl. Instr. and Meth. A **442** (2000) 58 and references therein.

[2] A. Breskin, “CsI UV photocathodes: history and mystery”, Nucl. Instr. and Meth. A **371** (1996) 116 and references therein.

[3] A. Piuz, “CsI-photocathode and RICH detector”, Nucl. Instr. and Meth. A **371** (1996) 96 and references therein.

[4] F. Piuz, A. Braem, M. Davenport, D. Di Bari, A. Di Mauro, D. Elia, B. Goret, P. Martinengo, E. Nappi, G. Paic, J.C. Santiard, S. Stucchi, G. Tomasicchio and T.D. Williams, “Final tests of the CsI-based ring imaging detector for ALICE experiment”, Nucl. Instr. and Meth. A **433** (1999) 178.

[5] H. Timan, “A survey of recent advances in the theory and practice of vacuum photoemitters”, Adv. Electronics and Electron Phys. **63** (1985) 73.

[6] A. Borovik-Romanov and V. Peskov, “Cs-based photocathodes for gaseous detectors”, Nucl. Instr. and Meth. A **348** (1994) 269.

[7] V. Peskov, A Borovik-Romanov, T. Sokolova and E. Silin, “Gaseous detectors of ultraviolet and visible photons”, Nucl. Instr. and Meth. A **353** (1994) 184.

[8] D.C. Nguyen, R.L. Sheffield, C.M. Fortgang, J.C. Goldstein, J.M. Kinross-Wright and N.E. Ebrahim.” First lasing of the regenerative amplifier FEL”, Nucl. Instr. and Meth. A **429** (1999) 125.

[9] J. P. Pansart, “Avalanche photodiodes for particle detection”, Nucl. Instr. and Meth. A **387** (1997) 186.

[10] R. Farrell, K. Shah, K. Vanderpuye, R. Grazioso, R. Myers and G. Entine, “APD arrays and large-area APDs via a new planar process”, Nucl. Instr. and Meth A **442** (2000) 171.

[11] V. Saveliev and V. Golovin, “Silicon avalanche photodiodes on the base of metal-resistor-semiconductor (MRS) structures”, Nucl. Instr. and Meth A **442** (2000) 223.

[12] N. Bachetta, D. Bisello, F. Broz, M. Catuozzo, Y. Gorta, E. Guschin, A. Lacaita, N. Malakhov, Y. Musienko, P. Nicolosi, A. Paccagnella, E. Pace, D. Pantano, Z. Sadygov, P. Villoresi and F. Zappa, “MRS detectors with high gain for registration of weak visible and UV light fluxes” Nucl. Instr. and Meth A **387** (1997) 225

[13] A.V. Akindinov, A.N. Martemianov, P.A. Polozov, V.M. Golovin and E.A. Grigoriev, “New results on MRS APDs”, Nucl. Instr. and Meth A **387** (1997) 231.

[14] G. Bondarenko, P. Buzhan, B. Dolgoshein, V. Golovin, E. Guschin, A Ilyin, V. Kaplin, A. Karakash, R. Klanner, V. Pokachalov, E. Popova and K. Smirnov, “Limited Geiger-mode microcell silicon photodiode: new results”, Nucl. Instr. and Meth A **442** (2000) 187.

[15] M.D. Petroff and M. Atac, “High energy particle tracking using scintillating fibers and solid state photomultipliers”, IEEE Trans. Nucl. Sci. **NS-36** (1989) 163.

[16] M.D. Petroff and M.G. Stapelbroek, “Photon-counting solid-state photomultiplier”, IEEE Trans. Nucl. Sci. **NS-36** (1989) 158.

[17] M.R. Wayne, “Visible light photon counters and the Dϕ scintillating fiber tracker”, Nucl. Instr. and Meth A **387** (1997) 278.

[18] M.D. Petroff., M.G. Stapelbroek and W.A. Kleinhans, “Detection of individual 0.4-28 (m wavelength photons via impurity-impact”, Appl. Phys. Lett. **51** (1987) 406.

[19] F. Galluzzi, M. Marinelli, L. Masotti, E. Milani, E. Pace, M.C. rossi, S. Salvatori, M. Santoro, S. Sciortino and G. Verona Rinati, “ CVD diamond films as photon detectors” Nucl. Instr. and Meth A **409** (1998) 423.

[20] H.J. Looi, N.D. Whitfield and R.B. Jackman, “Metal-semiconductor-metal photodiode fabricated from thin-film diamond”, Appl. Phys. Lett. **74** (1999) 3332.

[21] S Salvatori,F. Scotti, G. Conti and M.C. Rossi,”Diamond-based UV photodetectors for high temperature applications”, Electron. Lett. **35** (1999) 1768.

[22] P. Mandracci, F. Giorgis, C.F. Pirri and M.L. Rastello, “Large area and high sensitivity *a*-Si:H/*a*:SiC:H based detectors for visible and ultraviolet light”, Rev. Sci. Intrum. 70 (1999) 2235.

[23] E. Monroy, F. Calle, C. Angulo, P. Vila, A. Sanz, J.A. Garrido, E. Calleja, S. Haffouz, B. Beaumont, F. Omnes and P. Gibart, “GaN-based solar –ultraviolet detection instrument”, appl. Optics. **37** (1998) 5058.

[24] E. Monroy, F. Calle, E. Munoz, B. beaumont, F. Omnes and P. Gibart, “Schottky barrier ultraviolet photodetector on epitaxial lateral overgrown GAN”, Phys Stat. Sol. (a) **176** (1999) 141.

[25] G. Yu, K. Pakbaz and A.J. Heeger, “Semiconducting polymer diode: large size, low cost photodetector with excellent visible-ultraviolet sensitivity”, Appl. Phys. Lett. **64** (1994) 3422.

[26] Y.Yoshizawa, J.Takeuchi, “The latest vacuum photodetector”, Nucl. Instr. and Meth A **387** (1997) 33.

[27] R. De Salvo, W. Hao, K. You, Y. Wang and C. Xu, “First results on the hybrid photodiode tube”, Nucl. Instr. and Meth A **315** (1992) 375.

[28] A. Braem, E. Chesi, W. Dulinski, F. Filthaut, A. Go, C. Joram, J. Seguinot, P. Weilhammer, H. Wenzel, P. Wicht and T. Ypsilantis, “Highly segmented large-area hybrid photodiodes with bialkali photocathodes and enclosed VLSI readout electronics”, Nucl. Instr. and Meth A **442** (2000) 128.

[29] C. Damiani, A. Del Guerra, R. De Salvo, G. Vitale, G. Di Domenico, G. Zavattini, P. Benetti, D. Grassi, M. Merchesotti and M. Rossella, “Magnetic field effects on Hybrid PhotoDiode single electron response” Nucl. Instr. and Meth A **442** (2000) 136.

[30] N. Kanaya, Y. Fujii, K. Hara, T. Ishizaki, F. Kajino, K. Kawagoe, A. Nakagawa, M. Nozaki, T. Ota, T. Suzuki, H. Takeda, T. Takeshita, T. Toeda, Y. Yamada and C. Yokoyama, “Test results on hybrid photodiodes “, Nucl. Instr. and Meth A **421** (1999) 512.

[31] A. Go, “RICH detectors for the LHCb experiment”, Nucl. Instr. and Meth A **446** (2000) 305.

[32] R. Mirzoyan, D. Ferenc and E Lorenz, “An evaluation of the new compact hybrid photodiode R7110U-07/40 from Hamamatsu in high-speed light detection” Nucl. Instr. and Meth A **442** (2000) 140.

[33] K. Arisaka, “New trends in vacuum-based photon detectors”, Nucl. Instr. and Meth A **442** (2000) 80.

[34] J. Va'vra, "Photon detectors", Nucl. Instr. and Meth A **371** (1996) 33.

[35] J. Seguinot and T. Ypsilantis, “A historical survey of ring imaging Cherenkov counters”, Nucl. Instr. and Meth A **343** (1994) 1, and references therein.

[36] R. A. Holroyd, J. M. Preses, C. L. Woody and R. A. Johnson, “Measurement of the absorption length and absolute quantum efficiency of TMAE and TEA from threshold to 120 nm “, Nucl. Instr. and Meth A **261** (1987) 440.

[37] V. Dangendorf, A. Breskin, R. Chechik and H. Schmidt-Bocking, “Progress in ultrafast CsI-photocathode gaseous imaging photomultipliers “, Nucl. Instr. and Meth A **308** (1991) 519.

[38] G. Charpak, W. Domink, F. sauli and S. Majewski, “The gas photodiode as a possible large-area photon detector”, IEEE Trans. Nucl. Sci. **NS-30** (1983) 134.

[39] J. S. Edmends, D. J. Miller and F. Barlow, “Investigation of prototype gas-filled photomultipliers”, Nucl. Instrum. and Meth. A **273** (1988) 145.

[40] A. Breskin, E. Shefer, R. Chechik and A. Pansky, ”On the two-stage operation mechanism of low-pressure microstrip gas chambers” Nucl. Instr. and Meth A **345** (1994) 205.

[41] A. Buzulutskov, A. Breskin, R. Chechik, G. Garty, F. Sauli and L. Shekhtman, “The GEM photomultiplier operated with noble gas mixtures”, Nucl. Instr. and Meth. A **443** (2000) 164.

[42] L. Malter, “Thin film field emission”, Phys. Rev. **50** (1936) 48.

[43] A.Di Mauro, E. Nappi, F. Posa, A. Breskin, A. Buzulutskov, R. Chechik, S.F. Biagi, G. Paic and F. Piuz, “Photoelectron backscattering effects on photoemission from CsI into gas media”, Nucl. Instr. and Meth A **371** (1996) 137.

[44] F. Sauli and A. Sharma, “Micro pattern gaseous detectors”, CERN-EP/99-69, Ann. Rev. Nucl. and Particle Phys., in press.

[45] R. Bouclier, M. Capeans, W. Dominik, M. Hoch, J-C. Labbe, G. Million, L. Ropelewski, F. Sauli and A. Sharma, “The Gas Electron Multiplier (GEM)”, IEEE Trans. Nucl. Sci. **44** (1997) 646.

[46] W.E. Spicer, “Photoemissive, photoconductive and optical absorption studies of alkali-antimony compound”, Phys. Rev. **112** (1958) 114.

[47] C.N. Berglund and W. E. Spicer, “Photoemission studies of copper and silver: theory”, Phys. Rev. **136** (1964) 1030A and 1044A.

[48] T.Boutboul, A.Akkerman, A.Breskin and R.Chechik, “Escape length of UV-photoelectron in alkali iodide and CsBr evaporated films: measurements and modeling”, J. Appl. Phys. **84** (1998) 2890.

[49] W.E. Spicer, ”The influence of defect levels on photoemission”, RCA Rev. **19** (1958) 555.

[50] W.E. Spicer and A. Herrera-Gomez, “Modern theory and applications of photocathodes”, Proceedings of SPIE of the International symp. on optics imaging and instrumentation, San Diego, Ca, U.S.A., **2022** (1993) 18.

[51] E. A. Taft and H. R. Philipp, “Structure in the energy distribution of photoelectrons from K_3Sb and Cs-Sb”, Phys. Rev. **115** (1959) 1583.

[52] C. Kunze, “Untersuchungen an Cs-Sb-schichten”, Ann. Physik, **6** (1960) 89.

[53] B.R.C. Garfield and R.F. Thumwood, Brit. J. Appl. Phys **17** (1966) 1005.

[54] M. Hagino and T. Takashashi, “Thickness of Cs-Sb films relative to the original Sb films”, J. Appl. Phys. **37** (1966) 3741.

[55] W.H. McCarroll, “Crystal structure of photoelectric films of cesium-antimony”, J. Appl. Phys. **32** (1961) 2051.

[56] F.W. Dorn and W. Klemm, Z. Anrog. Allgem Chem. **309** (1961) 189.

[57] A.H. Sommer, "Photoemissive materials", Robert E. Krieger publishing comp., Huntington, New York, 1980.

[58] A.H. Sommer, “A new alkali antimonide photoemitter with high sensitivity to visible light”, Appl. Phys. Lett. **3** (1963) 62.

[59] W.H. McCarroll, “Chemical and structural characteristics of the potassium-cesium-antimony photocathode”, J. Phys. Chem. Solids, **26** (1965) 191.

[60] R.U. Martinelli and D.G. Fisher, “The application of semiconductors with negative electron affinity surfaces to electron emission devices”, Proc. of the IEEE, **62** (1974) 1339.

[61] E.A. Taft and L. Apker, “Photoemission from cesium and rubidium tellurides”, J. Opt. Soc. Am., **43** (1953) 81.

[62] B.K. Singh, E. Shefer, A. Breskin, R. Chechik and N. Avraham, “CsBr and CsI UV photocathodes: new results on QE and aging”, Nucl. Instr. and Meth. A **454** (2000) 364.

[63] E.A. Taft and H.R. Philipp, “Photoelectric emission form the valence band of some alkali halides”, J. Phys. Chem. Solids **3** (1957) 1.

[64] T. Boutboul, A. Breskin, R. Chechik, E. Klein, A. Braem, G. Lion and P. Mine, “On the surface morphology of thin alkali halide photocathode films”, Nucl. Instr. and Meth. A **438** (1999) 409.

[65] E. Shefer, A. Breskin, A. Buzulutskov, R. Chechik, M. Klin and M. Prager, “Laboratory production of efficient alkali-antimonide photocathodes”, Nucl. Instr. and Meth A **411** (1998) 383.

[66] E. Ritter, in “*Physics of Thin Films*”, edited by G. Hass (Academic, New York, 1963) Vol. 1, p. 123.

[67] U. Kaiser, N. Kaiser, P. Weisbrodt, U. Mademann, E. Hacker and H. Muller, “Structure of thin fluoride films deposited on amorphous substrates”, Thin solid Films **217**, (1992) 7.

[68] A. Buzulutskov, A. Breskin and R. Chechik, “Photoemission through thin dielectric coating films”, J. Appl. Phys. **81** (1997) 466.

[69] A. Kadyshevitch and R. Naaman, “Photoelectron transmission through organized thin films”, Phys Rev. Lett. **74** (1995) 3443.

[70] T. Miki, K. Inaoka, K. Sato and M. Okada, “Molecular orientation in the physical-vapor-deposited thin films of calcium stearate”, Jpn. J. Appl. Phys, **24** (1985) L672.

[71] T.H. DiStefano and W.E. Spicer, “Photoemission for CsI: Experiment”, Phys. Rev. B **7** (1973) 1554.

[72] L.Apker, E.Taft and J.Dickey, “Electron scattering and the photoemission from cesium antimonide”, J. Opt. Soc. Am. **43** (1953) 78.

[73] R. Natahn and C.H.B. Mee, “The energy distribution of photoelectrons form the K_2CsSb photocathode”, Phys. Stat. Sol. (a) **2** (1970) 67.

[74] R. Natahn and C.H.B. Mee, “Photoelectric and related properties of the Potassium-Antimony-Cesium photocathode”, Int. J. Electronics **23** (1967) 349.

[75] R.T. Poole, J.G. Jenkin, J. Liesegang and R.C.G.Leckey, “Electronic band structure of the alkali halides. I. Experimental parameters”, Phys. Rev. B **11** (1975) 5179.

[76] A.Akkerman, T.Boutboul, A.Breskin, R.Chechik, and A.Gibrekhterman, “Low-energy electron transport in alkali halides”, J. Appl. Phys. **76** (1994) 4656.

[77] T. Boutboul, “Study of photoinduced secondary electron emission from alkali halides”, Thesis for Ph. D. November 1998.

[78] F. James, “Monte Carlo theory and practice”, Rep. Prog. Phys**. 43** (1980) 1145.

[79] R. Shimizu and D. Ze-Jun, “Monte Carlo modeling of electron-solid interactions”, Rep. Prog. Phys. **55** (1992) 487.

[80] A.Breskin, A.Buzulutskov, R.Chechik, M.Prager and E.Shefer, “Evidence for thin-film protection of visible photocathodes” Appl. Phys. Lett. **69** (1996) 1008.

[81] A. Buzulutskov, A. Breskin, R. Chechik, M. Prager and E. Shefer, “Protection of cesium-antimony photocathodes”, Nucl. Instr. and Meth. A **387** (1997) 176.

[82] A Buzulutskov, E. Shefer, A. Breskin, R. Chechik and M. Prager, “the protection of K-Cs-Sb photocathodes with CsBr films”, Nucl. Instr. and Meth. A **400** (1997) 173.

[83] E. Shefer, A. Breskin, A. Buzulutskov, R. Chechik and M. Prager, “Towards gaseous imaging photomultipliers for visible light” Proc. Of the International Conference on High Energy Physics, Jerusalem, Israel, August 1997 Eds. Lellouch, Mikenberg and Rabinovici, p. 1081.

[84] E. Shefer, A. Breskin, A. Buzulutskov, R. Chechik and M. Prager, “composite photocathodes for visible photon imaging with gaseous photomultipliers”, Nucl. Instr. and Meth. A **419** (1998) 612.

[85] E. Shefer, A. Breskin, R. Chechik, A. Buzulutskov, B.K. Singh and M. Prager, “Coated photocathodes for visible photon imaging with gaseous photomultipliers”, Nucl. Instr. and Meth.A **433** (1999) 502.

[86] A. Buzulutskov, A. Breskin, E. Shefer, R. Chechik and M. Prager, “Removable organic protective coating for alkali-antimonide photocathodes”, Nucl. Instr. and Meth. A **413** (1998) 275.

[87] M. Grunder and H. Jacob, “Investigation on hydrophilic and hydrophobic Silicon (100) wafer surfaces by x-ray photoelectron and high-resolution electron energy loss spectroscopy”, Appl. Phys. A **39** (1986) 73.

[88] H. Yao, J.A. Woollam and S.A. Alterovitz, “Spectroscopic ellipsometry studies of HF treated Si (100) surfaces”, Appl. Phys. Lett. **62** (1993) 3324.

[89] P. Pfluger, H.R. Zeller and J. Bernasconi, “Hot electron transport in polymeric dielectrics”, Phys Rev. Lett. **53** (1984) 94.

[90] M. Rei Vilar, G. Blatter, P. Pfluger, M. Heynman, M. Schott, “Monoenergetic and directed electron emission from a large-bandgap organic insulator with negative electron affinity”, Europhys. Lett. **5** (1988) 375.

[91] B.L.Henke, J. Liesegang and S.D. Smith, “Soft X-ray-induced secondary-electron emission from semiconductors and insulators: Models and measurements”, Phys. Rev. B **19** (1979) 3004.

[92] G.W. Fraser, “The characteristics of soft X-ray photocathodes in the wavelength band 1-300Å II. Cesium iodide and other insulators of high photoelectric yield”, Nucl. Instrum. and Meth. **206** (1983) 265.

[93] M.P. Kowalski, G.G. Fritz, R.G. Cruddace, A.E. Unzicker and M. Swanson, “Quantum efficiency of cesium iodide photocathodes at soft X-ray and extreme ultraviolet wavelengths”, Appl. Opt. **25** (1986) 2440.

[94] T.G. Fiske and L.B. Coleman, “Longitudinal-optical phonons in thin films of rubidium iodide, potassium iodide, rubidium bromide, cesium iodide and cesium bromide”, Phys. Rev. B 45 (1992) 1414.

[95] D.F. Anderson, S. Kwan and V.Peskov, “Properties of CsI and CsI-TMAE photocathodes”, Nucl. Intrum. and Meth. A **323** (1992) 626.

[96] J. Lacer and E.L. Garwin, “Electron-phonon interaction in alkali halides. I. The transport of secondary electrons with energies between 0.25 and 7.5eV”, J. Appl. Phys. **40** (1969) 2766.

[97] I.R. McDonald, A.M. Lamki and C.F.G. Delaney,” Electron emission from alkali halides under soft X-ray bombardment”, J. Phys. D **6** (1973) 87.

[98] A .Akkerman, A. Gibrerkhterman, A. Breskin and R. Chechik, “Monte Carlo simulations of secondary electron emission from CsI, induced by 1-10keV X-rays and electrons”, J. Appl. Phys. **72** (1992) 5429.

[99] A. Akkerman, A. Breskin, R. Chechik and A. Gibrerkhterman, “Secondary electron emission from alkali halides induced by X-rays and electrons”, in *Ionization of Solids by Heavy Particles* (Plenum, New York, 1993), p.359.

[100] A. Gibrerkhterman, A. Akkerman, A. Breskin and R. Chechik, “The spatial characteristics of electron- and photon-induced secondary electron cascades in CsI”, J. Appl. Phys. **76** (1994) 1676.

[101] A di Bona, F. Sabary, S. Joly, P. Michelato, D. Sertore, C. Pagani and S. Valeri, “Development, operation and analysis of bi-alkali antimonide photocathodes for high-brightness photo-injectors “,Nucl. Instr. and Meth. A **385** (1997) 385.

[102] Handbook of the physichemical properties of the elements, Ed. G.V. Samsanov, Plenum Pub. New-York, 1968, pp. 254-255.

[103] J. Cazaux, “Some physical descriptions of the charging effects in insulators under irradiation”, in *Ionization of Solids by Heavy Particles* Plenum, New York, 1993, p. 325.

[104] J. Cazaux, “The electric image effects at dielectric surfaces”, IEEE Trans on Dielec. And Elec. Insul. **3** (1996) 75.

[105] J. Va’vra, A. Breskin, A. Buzulutskov, R. Chechik and E. Shefer, “Study of CsI photocathodes: volume resistively and aging”, Nucl. Instr. and Meth. A **387** (1997) 154.

[106] A.H. Sommer, US Patent 3,712,700 (1973).

[107] D.S. campbell, in: L.I. Maissel and R. Glang (Eds.), “Handbook of Thin film Technology”, McGraw-Hill, New-York, 1983 pp. 12-21 – 12-40.

[108] A. Buzulutskov, A. Breskin, E. Shefer, R. Chechik and M. Prager, “Organic protective coatings for alkali-antimonide photocathodes”, In ``New Detectors'' (ed. C.Williams and T. Ypsilantis) World Scientific Publishing (1999), p.195.

[109] L.S. Pan and D.R. Kania (eds.), “Diamond: electronic properties and application”, Kluwer academic publisher, 1995, pp.73-80.

[110] Y. Lifshitz, “Hydrogen-free amorphous carbon films: Correlation between growth conditions and properties”, Diam. Relat. Mater. **3-5** (1996) 388.

[111] Y. Lifshitz, G.D. Lempert, E. Frossman, H.J. Scheibe, S. Voellmar, B. Schultrich, A. Breskin, R. Chechik, E. Shefer, D. Bacon, R. Kalish and A. Hoffman, “Optical and photoemission studies of DLC films prepared with a systematic variation of the sp^3:sp^2 composition”, Diamonds and related materials, **6** (1997) 687.

[112] A. Breskin, R. Chechik, E. Shefer, D. Bacon, Y. Avigal, R. Kalish and Y. Lifshitz, “Absolute photoyield from chemical vapor-deposited diamond and diamond-like carbon films in the UV”, Appl. Phys. Lett.**70** (1997) 3446.

[113] A. Laikhtman, A. Hoffman, R. Kalish, Y. Avigal, A. Breskin, R. Chechik, E. Shefer, and Y. Lifshitz, “Absolute quantum photoyield of diamond thin films: Dependence on surface preparation and stability under ambient conditions”, Appl. Phys. Lett. **73** (1998) 1433.

[114] A. Laikhtman, Y. Avigal, R. Kalish, A. Breskin, R. Chechik, E. Shefer, Y. Lifshitz and A. Hoffman, “Surface quality and composition dependence of absolute quantum photoyield of CVD diamond films”, Diamonds and related materials, **8** (1999) 725.

[115] A. Laikhtman, “Electron emission properties of diamond surfaces”, Thesis for M.Sc. August 1999.

[116] A. Buzulutskov, A. Breskin and R. Chechik, “Heat enhancement of the photoyield from CsI, NaI and CuI photocathodes”, Nucl. Instr. and Meth. A **366** (1995) 410 and references therein.

[117] A. Breskin, “Progress in low-pressure gaseous detectors “, Nucl. Instr. and Meth. **196** (1982) 11.

[118] F. Fonte, V. Peskov and F. Sauli, “VUV emission and breakdown in parallel-plate chambers.” Technical report, European organization for nuclear research, 1991. Cern report-talk given at 2nd London Conference 1990.

[119] A. Oed, “Position-sensitive detector with microstrip anode for electron multiplication with gases”, Nucl. Instr. and Meth A **263** (1988) 355.

[120] S.F. Biagi, J. Bordas, D. Duxbury, E. Gabathuler, T.J. Jones and S. Kiourkos, “First experimental results from a microdot gas avalanche detector integrated onto a silicon wafer”, Nucl. Instr. and Meth. A **366** (1995) 76 and references therein.

[121] F. Angelini, R. Bellazzini. A. Brez, M.M. Massai, R. Raffo, G. Spandre and M.A. Spezziga, “The micro-gap chamber”, Nucl. Instr. and Meth A **335** (1993) 69.

[122] E. Shefer, A. Breskin, R. Chechik, G. Gefen and A. Pansky, “Low pressure operation of microstrip gas chambers”, Proc. of the International workshop on micro-strip gas chambers, Legnaro Italy, 13-14 October 1994, Ed. G.Della Mea and F.Sauli, p. 107.

[123] A. Breskin, R. Chechik, G. Garty, A. Pansky, E. Shefer and S.F. Biagi, “On the high gain operation of low-pressure microdot gas avalanche chambers”, Nucl. Instr. and Meth. A **394** (1997) 21.

[124] S. Bachmann, A. Bressan, L. Ropelewski, F. Sauli and D. Mörmann, “Recent progress in GEM manufacturing and operation “, Nucl. Instr. and Meth A **433** (1999) 464 and references therein.

[125] R. Chechik, A. Breskin, G. Garty, J. Mattout, F. Sauli and E. Shefer, “First results on the GEM operated at low gas pressures”, Nucl. Instr. and Meth. A **419** (1998) 423.

[126] G. Garty, A. Breskin, R. Chechik and E. Shefer, Nucl. Instr. and Meth. “Single photoelectron detection with a low-pressure GEM coupled to a CsI photocathode”, A **433** (1999) 476.

[127] C. Richter, A. Breskin, R. Chechik, D. Mörmann, G. Garty and A. Sharma, “On the efficient electron transfer through GEM”, submitted to Nucl. Instr. and Meth. A

[128] A. Breskin, A. Buzulutskov, R. Chechik, E. Shefer and B.K. Singh, “Sealed gas UV-photon detector with multi-GEM amplication”, submitted to Nucl. Instr. and Meth. A

[129] R. Enomoto, T. Sumiyoshi and Y. Fujita, “Test of various photocathodes”, Nucl. Instr. and Meth. A **343** (1994) 117.

[130] D.R. Winn, “Large photocathodes detectors for large calorimetry”, IEEE Trans. Nucl. Sci. NS-**36** (1989) 128.

[131] P.M. Beschastnov, S.G. Klimenko, E.A. Kravchenko, G.D. Minakov, A.P. Onuchin and V.I. Telnov, “Gated photon detector for the visible wavelength region”, Nucl. Instr. and Meth. A **387** (1997) 180.

[132] A. Buzulutskov, L. Shekhtman, A. Bressan, A. Di Mauro, L. Ropelewski, F. Sauli and S. Biagi, “GEM operation in pure noble gases and the avalanche confinment”, Nucl. Instr. and Meth. A **433** (1999) 471.

[133] V. Peskov, E. Silin, T. Sokolova and I. Radionov, “First attempts to combine capillary tubes with photocathodes”, Nucl. Instr. and Meth. A **433** (1999) 492.

[134] N.W Achcroft and N.D. Mermin, *Solid state physics* Saunders , Philadelphia, 1976 p. 304.

[135] C. Coluzza, private communication.

[136] The MICADO project, European Union Contract No. IN20589I.

[137] T. Ypsilantis and J. Seguinot, “Theory of ring imaging Cherenkov counters”, Nucl. Instr. and Meth. A **343** (1994) 30.

[138] A. Breskin, R. Chechik, D. Vartsky, G. Malamud and P. Mine, “A correction of the quantum efficiency of CsI and other photocathodes due to the recalibration of the reference photomultiplier”, Nucl. Instr. and Meth. A **343** (1994) 159.

[139] I. Boscolo and P. Michelato, “Photocathodes: the state of the art and some news”, Nucl. Instr. and Meth. A **445** (2000) 389.

עבודה זאת עוסקת בהרחבת תחום הרגישות של גלאי-אור גזיים, המופעלים היום בהצלחה בתחום האולטרא-סגול הרחוק (140-220 ננומטר), אל עבר תחום האולטרא-סגול הקרוב ועד האור הנראה (300-450 ננומטר). גילוי האור בסוג זה של גלאים מבוסס על המרת הפוטונים לאלקטרונים בתוך שכבת ממיר (פוטוקתודה) מוצקה ודקה, והכפלתם במכפל (multiplier) אלקטרונים גזי. לגלאים מסוג זה יתרונות רבים: הם דקים ובעלי שטח פעיל גדול, רגישים לאור עד כדי פוטון בודד והנם בעלי כושר הפרדת זמן ומקום מצוינות; השימוש בממיר מוצק מונע אי-דיוקים בזמן בשל time jitter ובמקום בשל פרלקסה; מכפלי אלקטרונים גזיים רגישים לשדה מגנטי הרבה פחות מאלו המבוססים על הכפלת אלקטרונים בואקום. אולם בגלל הרגישות הכימית הגבוהה של פוטוקתודות מסוג אלקלי-אנטימוניד, היעילות בתחום הספקטרום האולטרא-סגול עד האור הנראה, לא נבנו גלאים גזיים בתחום זה עד היום.

בעבודה זו מוצגות התוצאות העיקריות של מחקרנו בפיתוח פוטוקתודות חדשות המיועדות לגלאי-אור גזיים, בתחום הספקטרלי של האולטרא-סגול עד האור הנראה. חקרנו בפירוט את הרעיון לצפות פוטוקתודות מסוג אלקלי-אנטימוניד בשכבות דקות של חמר דיאלקטרי, כדי להגן עליהן ולמנוע ריאקציה כימית עם שיירי חמצן ומים השכיחים בגזים שמשמשים לספירת אלקטרונים. אפיינו באופן שיטתי את תכונות הפליטה (photoemission) של פוטוקתודות מצופות, באמצעות מדידה של ספקטרום היעילות הקוונטית האבסולוטית ושל התפלגות האנרגיה של הפוטו-אלקטרונים. חלק חשוב מעבודה זאת הוקדש ללימוד תכונות ההולכה (transport) של אלקטרונים בעלי אנרגיה נמוכה בפוטוקתודה, בשכבת הציפוי ובממשק בין שני החומרים. השתמשנו ב-XPS (ספקטרוסקופית פוטואלקטרונים מושרית על ידי קרני-X) כדי לקבוע את ההרכב הכימי של הפוטוקתודות המצופות ובחנו את יציבותן בחשיפה לגזים המשמשים לספירת אלקטרונים, לשטף פוטונים גבוה ותחת הכפלת אלקטרונים בגז.

המחקר התבצע בשתי מערכות ייעודיות שנבנו במהלך עבודה זאת, על מבחר רחב של חומרי ציפוי, כולל תחמוצות, מולקולות אורגניות וחומרים אלקלי-הלידיים. התוצאות הטובות ביותר, במונחים של יעילות קוונטית גבוהה ושל יציבות טובה בסביבה גזית, הושגו עם פוטוקתודות מסוג אשלגן-צזיום-אנטימוניד (K-Cs-Sb) שצופו בצזיום-ברומיד (CsBr) ובצזיום-יודיד (CsI). הראנו שעל-ידי הגדלת עובי הציפוי, גדלה יציבותה של הפוטוקתודה המצופה בסביבה גזית, זאת במחיר הקטנת היעילות הקוונטית. עבור פוטוקתודות מסוג K-Cs-Sb מצופות ב-CsI, ערכים סבירים של יעילות קוונטית - 5% עד 10% באורך גל של 312 ננומטר - הושגו עם יציבות בחמצן, בלחץ 150 0.11- ממ״ כספית , בהתאמה. יציבותן של פוטוקתודות מוגנות אלו בגז לאורך זמן ותחת הכפלת אלקטרונים נבדקו. נמצאו הזדקנות וטעינה חשמלית ברמה מתונה אשר אינן צפויות להגביל את השימוש בהן.

את ההולכה של אלקטרונים נמוכי אנרגיה דרך שכבות ציפוי מסוג אלקלי-הלידים חקרנו על-ידי מדידת אורך הדעיכה של היעילות הקוונטית (דהינו תלות היעילות הקוונטית בעובי הציפוי) ועל-ידי מדידת התפלגות האנרגיה של הפוטו-אלקטרונים. הבחנו שתכונות ההולכה של האלקטרונים תלויות גם בפוטוקתודה וגם בשכבת הציפוי, וזאת בגלל הממשק (interface) המיוחד הנוצר בין שני החומרים. הממשק בין שני חומרים אלה, אשר יוצר מחסום פוטנציאל, הוא בעל חשיבות גדולה עבור אלקטרונים נמוכי-אנרגיה ואמנם חלק גדול מהאלקטרונים המשתחררים בפוטוקתודה מוחזרים או נבלעים בממשק זה. במקרה של ציפויים עבים מ- 5 ננומטר, מעבר האלקטרונים ופליטתם אל הואקום נשלט ע״י תכונות הציפוי הדיאלקטרי: פער אנרגיה (energy gap) גדול בין פס הערכיות ופס ההולכה וריכוז נמוך של זיהומים יתרמו להולכת אלקטרונים טובה, בעוד שאפיניות אלקטרונית (electron affinity) נמוכה או שלילית תגדיל את הסתברות הבריחה אל הואקום.

מודל שפותח בקבוצתנו, המתאר את תהליך הולכת אלקטרונים נמוכי אנרגיה בחומר דיאלקטרי כרצף של אינטראקציות בין האלקטרונים לפונונים, הורחב כאן כדי לכלול גם את הממשק בין הפוטוקתודה

לציפוי. הממשק תואר כפונקצית מדרגה והמודל מאפשר לאלקטרונים לעבור אותו מספר פעמים. השתמשנו במודל זה כדי לחשב את אורך הדעיכה של היעילות הקוונטית ואת התפלגות האנרגיה של הפוטו-אלקטרונים. בהשוואת התוצאות המדודות ניסיונית לאלו המחושבות בעזרת המודל נתקבלה התאמה טובה, אשר נותנת תוקף לגישה זו.

חלק מן העבודה הנוכחית עסק בחקר הפליטה מיהלומים המיוצרים בשיטת CVD ומשכבות צזיום-ברומיד, שניהם נחקרו כפוטוקתודות לאור אולטרא-סגול רחוק. היעילות הקוונטית שלהם פחותה בהשוואה לזאת של פוטוקתודות מסוג צזיום-יודיד בהן משתמשים כיום לאור אולטרא-סגול רחוק. יחד עם זאת, יהלומי CVD יציבים למדי באוויר ותחת קרינה ושכבות צזיום-ברומיד יכולות לשמש כפוטוקתודות שאינן רגישות לאור השמש (solar blind).

חלק חשוב ביותר בפתוח גלאי-אור גזיים הוא בחירתו של מכפל האלקטרונים המתאים ביותר למטרה זו. במיוחד חשוב לבחור מכפל כזה שעל אף צימודו לממיר רגיש לאור לא יפגע תפקודו עקב משוב חיובי של פוטונים מחד, ומאידך שלא יפגע הממיר עקב משוב של יונים חיוביים. מבין מכפלי האלקטרונים הגזיים החדשים שנחקרו. ה-GEM (Gas Electron Multiplier) הוא המבטיח ביותר. הושגו תוצאות מצוינות המראות הכפלה גבוהה של פוטו-אלקטרונים בודדים, הפחתה של משוב היונים והפוטונים ויעילות העברת אלקטרונים של 100%. שרשור של מספר מכפלי GEM בטור מפחיתה עוד יותר את משוב היונים והפוטונים ומאפשרת הפעלה יציבה בגזים אצילים. כל אלה הופכים את הרב-GEM למכפל הנבחר לגלאי-אור גזיים עם ממיר מוצק, בתחום האולטרה סגול הקרוב עד אור נראה.

בעבודה זאת הראנו לראשונה שאפשר להגן על פוטוקתודות רגישות ובו בזמן לשמור על ערכי יעילות קוונטית סבירים. זהו צעד מרכזי וחשוב בפיתוח מכפלי-אור גזיים עבור אור אולטרא-סגול עד אור נראה. ממירי אור ברמת ההגנה וערכי היעילות הקוונטית שהושגו בעבודה זאת ניתן לנצל ליישומים בתחומי הדמיה רפואית ופיזיקה של חלקיקים.

למרות תרומתה הרבה של עבודה זו לפיתוחם של גלאי פוטונים גזיים לאור נראה, נותרו מספר נושאים הדורשים מחקר נוסף: ההגנה שהושגה בפני כמות שיורית של מים אינה מספקת. תוצאות טובות יותר ניתן להשיג אולי באמצעות שימוש בפולימרים דוחי-מים, כשכבת מגן שניה מעל פוטוקתודה מוגנת מחמצן. אפשר להרחיב את החיפוש אחר חומרי-מגן חדשים המספקים יציבות גם בחמצן וגם במים, ובעלי הולכת אלקטרונים טובה, אפיניות אלקטרונית נמוכה וכיסוי גיאומטרי מלא של שטח הפנים של הפוטוקתודה. חומרים כאלו ימצאו אולי בתחום המוליכים למחצה. דרוש מחקר של ההרכב הכימי של הפוטוקתודות המוגנות ושל המנגנון האחראי להגנה כדי לסייע בחיפוש אחר חומרי-מגן חדשים. אפשר להרחיב את המודל המתאר מעבר של אלקטרונים נמוכי-אנרגיה כך שיכלול זיהומים, מבנה מרובה גבישים (polycrystalline) ומבנה אמורפי ויותאם לסוגים של חומרים אחרים. כמו כן נדרש לימוד של אופן הפעלת הפוטוקתודות לתקופות ממושכות במכפל אלקטרונים גזי מתאים.